# OPTIMIZATION OF AIRCRAFT TOW STEERED COMPOSITE WING STRUCTURES

by

MICHAEL CHAMBERLAIN HENSON

Presented to the Faculty of the Graduate School of

The University of Texas at Arlington in Partial Fulfillment

Of the Requirements

For the Degree of

DOCTOR OF PHILOSOPHY

THE UNIVERSITY OF TEXAS AT ARLINGTON

December 2017

**Acknowledgements**

The list of people who supported me in this journey towards a PhD is long and I will not be able to list them all here. However, I would like to acknowledge the UTA MAE faculty, my colleagues at Lockheed Martin Aeronautics, my friends and most importantly my family.

This work would not have been accomplished without the support and guidance of my advisor and committee chairman, Dr. Bo Ping Wang. His expertise, patience and encouragement had a profound influence on my research. I would like to acknowledge my Graduate Advisor, Dr. Seiichi Nomura who allowed me to complete this work over an extended time period. I wish to thank my committee; Dr. Ashfaq Adnan, Dr. Brian Dennis, Dr. Kent Lawrence and Dr. Robert Taylor for their support and guidance. Thanks to Dr. Rob McDonald of Cal Poly and Dave Kinney of NASA Ames for their guidance in the use of OpenVSP and VSPAero. Thanks to Mark Lovrich and Larry Collins of TMP for complimentary use of their CAE software. I would also like to acknowledge Lockheed Martin for the employee tuition reimbursement they provided. I would like to thank the many friends and colleagues who encouraged me over the years.

Finally, I would like to say that this work could not have been finished without the support and love my wife Janie, my daughter Mary and my son Matt. They are everything to me. I would also like to thank my parents Lyman Henson and Kay Henson for their love and the value they instilled in me for a higher education. I know my father would have very much liked to see this work completed, if it were not for his passing.

December 15, 2017

**Abstract**

OPTIMIZATION OF AIRCRAFT TOW STEERED COMPOSITE WING STRUCTURES,

Michael Chamberlain Henson, PhD

The University of Texas at Arlington, 2017

Supervising Professor: Dr. Bo Ping Wang

An efficient methodology for design of aircraft composite wing structures is presented. The developed approach provides a flexible and integrated strategy to leverage advantages of composite material tow steering to achieve more effective wing designs. This is accomplished by including the coupling between OML geometry, aerodynamics and structural response. Structural and aerodynamic analyses are derived from parametric aircraft geometry and assembled into a framework for aero-structural wing sizing. A Ritz equivalent plate solution is extended to model composite materials with variable fiber path geometry. The structural modeling approach is implemented to automate creation of both Ritz and finite element analyses. The Ritz structural model is coupled to a vortex lattice flow solver and implemented into an optimization framework. By using this approach we are more rapidly able to gain an understanding of optimal wing skin laminates that satisfy a variety of constrains and objective functions. The framework is suitable for conceptual and preliminary design of aircraft wing skins and it has been applied to accomplish a tow-steered wing skin design.

Table of Contents

## List of Figures

## List of Tables

## Nomenclature

| | |
|---|---|
| *AFP* | Automated Fiber Placement |
| $\{B\}$ | Ritz basis vectors |
| $b$ | wing span |
| $c$ | chord length |
| *EPM* | Equivalent Plate Method |
| $\{F_{\bar{q}}\}$ | generalized force vector |
| *FEA* | Finite Element Analysis |
| *FEM* | Finite Element Method |
| FSDT | First-order Shear Deformation Theory |
| $g(x)$ | inequality constraint function |
| $g_{\varepsilon}, g_{strain}$ | strain constraint |
| $g_{\lambda_b}, g_{buckling}$ | buckling constraint |
| $g_{\lambda_f}, g_{flutter}$ | flutter constraint |
| $g_m, g_{mingage}$ | minimum gage thickness constraint |
| $g_{pp}, g_{plypercent}$ | allowable ply percentage constraint |
| $h(x)$ | equality constraint function |
| $[K_{\bar{q}}]$ | stiffness matrix |
| $M$ | Mach number |
| $[M_{\bar{q}}]$ | mass matrix |

| | |
|---|---|
| $N_i(\xi,\eta)$ | bi-linear lagrangian interpolation functions |
| $N_{layer}$ | number of orthotropic skin layers |
| $N_{ply}$ | number of plies in a laminate |
| $N_p$ | polynomial order of Legendre basis function |
| $N_{rib}$ | number wing ribs |
| $N_{spar}$ | number wing spars |
| $\{N_x, N_y, N_{xy}\}$ | in-plane panel force resultants |
| $N_z$ | Normal load factor |
| *OML* | Outer Mold Line |
| $P_i(x)$ | Legendre polynomials |
| $\{\bar{q}\}$ | generalized displacement vector |
| *s* | length of semi-span of wing |
| $t_U, t_L$ | total thickness of upper/lower wing skins |
| $t_{U_k}, t_{L_k}$ | k-th ply thickness of upper/lower wing skins |
| $t_{ij}$ | polynomial skin thickness coefficients |
| *u, v, w* | displacements in x, y, z directions |
| *UD* | unidirectional laminate |
| *UDrot* | rotated unidirectional laminate |
| *VAT* | variable angle tow laminate |
| $w_{sc}, w_{rc}$ | width of spar cap, width rib cap |
| $t_{sc}, t_{rc}$ | thickness of spar cap, thickness of rib cap |
| $h_{sw}, h_{rw}$ | height of spar web, height of rib web |

| | |
|---|---|
| $t_{sw}, t_{rw}$ | thickness of spar web, thickness of rib web |
| $\{x\}$ | design variable vector |
| $x_l, x_u$ | design variable upper and lower bounds |
| *(x, y, z)* | airframe cartesian coordinate directions |
| $\{\varepsilon\}$ | strain vector |
| $\{\bar{\varepsilon}\}$ | transformed strain vector |
| $\phi_x, \phi_y$ | rotations about x and y axes |
| $\theta_0, \theta_1$ | reference fiber path orientation coefficients |
| $\theta_U, \theta_L$ | reference fiber path orientation of upper, lower skin |
| $\theta_{U_0}, \theta_{U_1}$ | upper surface reference fiber path coefficients |
| $\theta_{L_0}, \theta_{L_0}$ | wing lower surface root and tip fiber constants |
| $\xi, \eta$ | transformed wing computational coordinates |

# Chapter 1

# Introduction

## 1.1 Trends in Aircraft Conceptual Design

Rapid exploration of aircraft conceptual design space has increased the need for efficient modeling and analysis techniques. Many configurations are evaluated in multidisciplinary design trades to determine the values of system-level variables such as gross weight and external geometry shape parameters which are used to measure overall vehicle performance. Airframe modeling and evaluation in the early stages of design is often avoided because structural layout and sizing activities cannot keep pace with the configuration development process. Further, utilization and advancement of composite materials for aircraft structures is being driven by ongoing requirements to reduce weight, increase air vehicle fuel efficiency, improve aero-structural performance and reduce airframe cost.

Important aircraft development trends are shown in Figure 1-1 and Figure 1-2. These include the need to address aircraft development costs early in the design cycle, shorten development time and to leverage the growing use of composite materials. The aerospace industry is keenly aware of these needs as it is estimated that 90% of the cost of a product is committed during the first 10% of the design cycle. Composite utilization for recently developed airframe ranges from 35% to 55% and continues to grow.

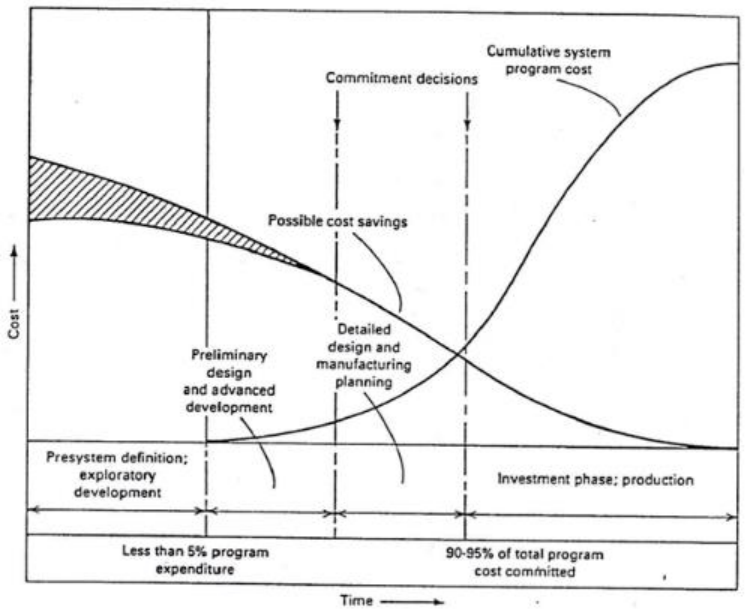


Figure 1-1. Aircraft development cost profile [1]

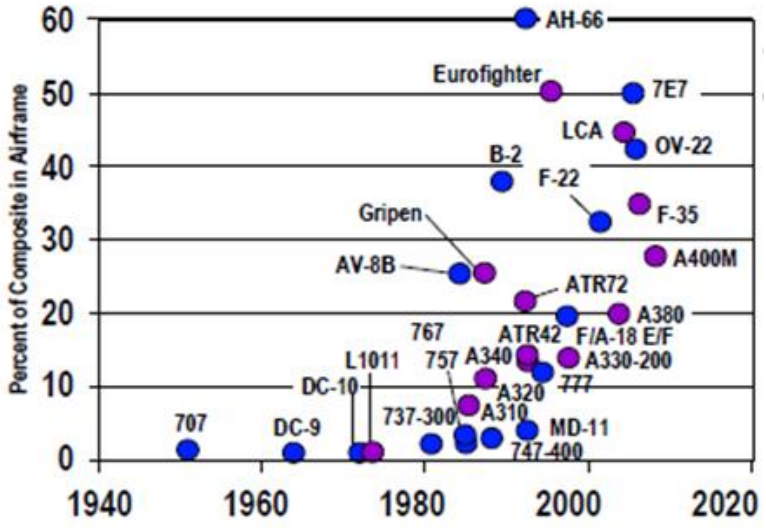


Figure 1-2. Trends of composite material utilization in aircraft [1].

## 1.2 Motivation for Integrated Design Optimization

Aircraft are complex systems whose design requires consideration of multiple disciplines including aerodynamics, structures, materials, flight controls and propulsion. Airframe design trades conducted during conceptual design can provide valuable insight to structural layout feasibility, performance and early risk assessment. A first-order estimate of material required for strength and aeroelastic constraints can serve three critical needs [2]. First, data is provided in terms of the weight required to meet the combined structural constraints for various planforms and assists in the elimination of infeasible aerodynamic surfaces. Second, a critical evaluation can be made of material efficiency in aeroelastic constrained designs, and last, a preliminary risk assessment of structural concepts and materials can be performed. Martins et.al [3] demonstrated this concept by defining an optimum lift distribution to maximize aircraft range for a simple aero-structural design problem as shown in Figure 1-3.

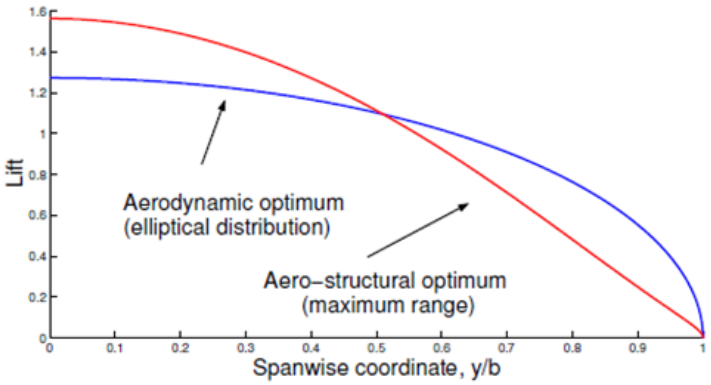


Figure 1-3. Optimum lift distribution for a simplified aero-structural problem [3].

## 1.3 Aerodynamic Analysis

A variety of aerodynamic analysis tools are used to perform aircraft design and can be generally categorized as: empirical, 2D/3D panel methods, computational fluid dynamics (CFD) and experimental (wind tunnel and flight tests). They are briefly described in increasing order of fidelity of flow representation and handling complex geometry. Empirical methods [4] are typically fast and based on previous aircraft data and include wind tunnel and flight tests. Panel methods provide detailed but simplified aerodynamics for complex configurations and are used routinely in industry. They are generally restricted to linear potential flow with small disturbances as illustrated in Figure 1-4(a) and applicable to slender bodies and thin wings at low angles of attack and sideslip. Panel methods are implemented by subdividing the configuration surface into quadrilateral 'panel' elements as shown in Figure 1-4(b) and are computationally efficient. One well know implementation is the vortex lattice method (VLM) described in [5]. Large disturbance flow over complex geometry is modeled using CFD and requires creation of detailed surface and volume meshes with high computational solution costs. Experimental wind tunnel and flight testing remain very important tools for aircraft development and are used to mature and certify a configuration. This effort will apply the VLM method for its computational efficiency, its ability to handle complex geometry and ease of coupling with a structural solution.

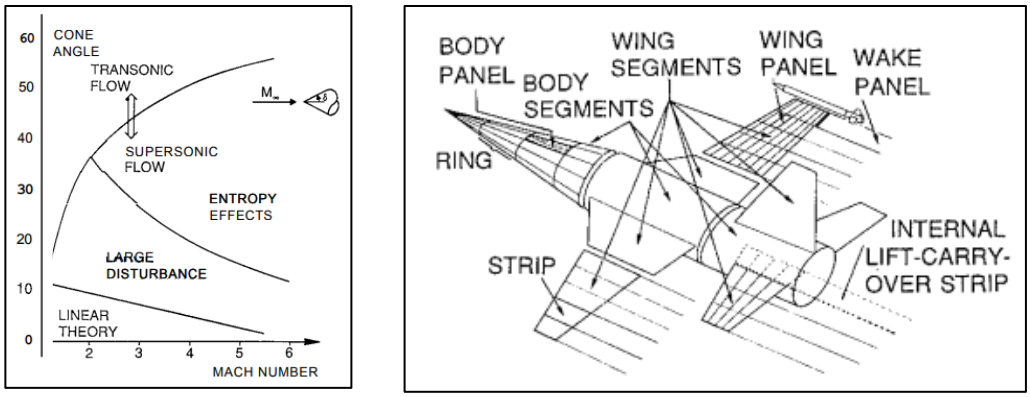


Figure 1-4. (a) Flow regimes on a circular cone [6] , (b) Example panel model [6].

## 1.4 Structural Analysis

The Finite Element Method (FEM) is widely used for aircraft structural analysis because of its versatility and reliability. However, setup and solution time using traditional FEM techniques are generally not well suited to support rapidly evolving configuration development. Alternatively, equivalent continuum models can be used to simulate the behavior of complex structural assemblies for the purpose of developing conceptual airframe design solutions. Continuum models are specified using continuous polynomials on only a few members and thus require only a small fraction of the input and time as a corresponding FEM where geometry and stiffness properties are specified discretely. The resulting reduction in model preparation time is important during early design phases when many candidate configurations must be assessed. Also, mass quantities and applied loads can be defined and easily relocated without disrupting other aspects of the model and must be facilitied during early design when design changes must occur rapidly. Moreover, the combined use of continuum models with FEM can be used

to rapidly calibrate and quantify uncertainties that may be present in lower order solutions. Giles [7] summarized the key features offered by these codes:

Key features of continuum methods:

- Adequate accuracy for early preliminary design
- Efficient computation
- Capability to trade accuracy for speed
- Minimal time for model preparation and modification
- Ease of coupling with other codes
- Capability to generate sensitivity derivatives

Several tools have been developed to study aircraft wing structures using continuum equivalent plate models [2], [7]-[15]. For example, the TSO (Aeroelastic Tailoring and Structural Optimization) code enjoyed widespread use but was limited to trapezoidal planforms [2], [8]. Giles developed ELAPS (Equivalent Laminated Plate Solution) while at NASA to analyze more complex planforms with internal structure [7], [9]-[11]. Tizzi developed a method similar to Giles and later provided support for modeling internal rib and spar structure [13]. Livne [14] formulated a wing equivalent plate model employing the use of First Order Shear Deformation Theory (FSDT). Kapania and Liu [15] presented the use of FSDT with well-behaved Legendre basis functions to model trapezoidal wing structures. Henson and Wang [16] applied this approach to model behavior of laminated quadrilateral plates with variable fiber path geometry and extended it to model static and modal behavior of built-up wings [17]. The Ritz equivalent plate method (EPM) will therefore be used in the present research and validated using FEM.

## 1.5 Laminated Composites Tailoring

The directional properties of laminated composite materials provide distinct advantages over metals in their ability to tailor aircraft structure for improved static and dynamic response at a reduced weight. Laminate tailoring is the process of establishing an optimal configuration of plies to meet one or more design objectives such as minimum weight. The traditional approach is to organize the laminate into constant thickness regions and then develop stacking sequences to locally optimize for criteria such as strength, buckling or to reinforce geometric features such as stiffeners, cutouts and fastener paths. A 0-degree reference fiber direction is established, commonly oriented in the principal load direction of the component and assumed to remain constant. A simple five zone composite wing skin example is shown in Figure 1-5.

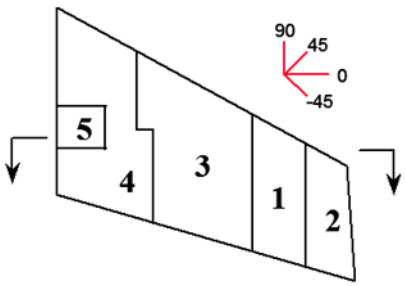


Section view - thickness exaggerated

| Zone | Thickness | Ply Percentages | | | |
|---|---|---|---|---|---|
| | | 0 | 45 | -45 | 90 |
| 1 | 0.176 | 37.5 | 25.0 | 25.0 | 12.5 |
| 2 | 0.198 | 33.3 | 22.2 | 22.2 | 22.2 |
| 3 | 0.209 | 36.8 | 26.3 | 26.3 | 10.5 |
| 4 | 0.242 | 31.8 | 27.3 | 27.3 | 13.6 |
| 5 | 0.286 | 34.6 | 26.9 | 26.9 | 11.5 |

| Zone | Total Plies | Orientation | | | |
|---|---|---|---|---|---|
| | | 0 | 45 | -45 | 90 |
| 1 | 32 | 12 | 8 | 8 | 4 |
| 2 | 36 | 12 | 8 | 8 | 8 |
| 3 | 38 | 14 | 10 | 10 | 4 |
| 4 | 44 | 14 | 12 | 12 | 6 |
| 5 | 52 | 18 | 14 | 14 | 6 |

Figure 1-5. Simple 5-zone composite wing skin [18].

The required laminate zone thickness and ply percentages are determined from a structural analysis and sizing process of the component to meet specified design criteria. For each region, plies with the same fiber orientation, most often combinations of [0/+45/-45/90] ply angles, are summed together to calculate the percentage of fibers in each direction. Total thickness and ply percentages are used to tailor in-plane laminate stiffness and strength whereas the ply stacking sequence is used to tailor laminate bending properties. Laminate thickness is tapered from thick to thin sections using ply terminations known as ply drop-offs. An example application of multi-zone laminate tailoring is shown in Figure 1-6 for a fighter wing skin.

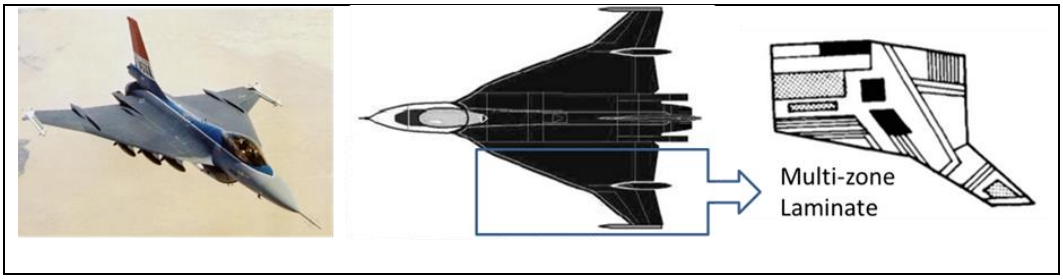


Figure 1-6. F16-XL fighter aircraft and multi-zone wing skin laminate [19], [20].

## 1.6 Automated Fiber Placement

Advancements in composite manufacturing technology have led to the development of automated fiber placement (AFP) introduced in the late 1980's [21]-[25]. The AFP machine shown in Figure 1-7 is a high precision robot with typically seven axes of motion, three translation, three rotation and a part-rotation axis to rotate the layup mandrel and position the fiber placement head to layup and compact material onto the part surface. Spools of slit unidirectional tape or pre-impregnated tows are supplied to the fiber placement head. Each tow is individually controlled with the ability to be

clamped, cut and restarted during layup. This makes it possible to deliver tows at different speeds and enables layup over complex surfaces. Tow materials come in typical widths of 1/8 in., 1/4 in. and 1/2 in. The head collects the tows to form a fiber band and delivers it to a segmented compaction roller where heat and force are applied to remove voids and de-bulk the material. A band of material deposited on the layup tool surface is designated as a course and a sequence of courses forms a ply.

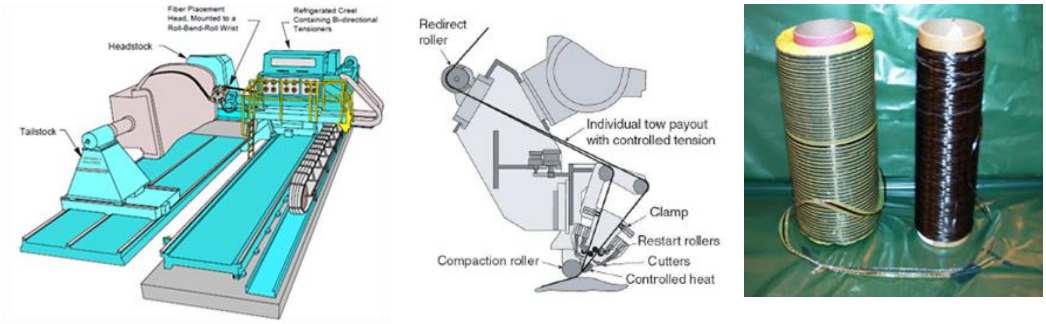


Figure 1-7. Automated Fiber Placement System Components and Materials [26].

AFP has gained recognition for its ability to fabricate complex aircraft structure with improved precision and reduced cost. Recent examples of large complex composite structure produced using this process are shown in Figure 1-8.


Figure 1-8. Aircraft structures produced using AFP (a) Raytheon business jet fuselage [27], (b) Airbus A380 aft fuselage [28], (c) Lockheed Martin JSF F-35 wing skin [29].

## 1.7 Tow Steering

The AFP process enables the steering of fibers in the plane of the layup surface as shown in Figure 1-9. It provides a unique capability to fabricate and tailor variable stiffness laminates using curvilinear fiber paths. It has led to development of a new class of composite materials called "tow steered" laminates. Tow steering attempts to tailor the stiffness of a composite laminate by placing fiber paths into curvilinear orientations within the plane of the ply.

The concept is motivated by the idea that it is possible to improve the structural performance of a laminate by using curvilinear fiber paths as opposed to straight fibers. The ability of a fiber placement machine to steer fibers in any direction presents the opportunity to design laminates with more efficient load paths and thus weight savings over traditional constant stiffness laminates. These composites are referred to in the literature as "fiber-steered", "tow-steered", and "variable angle tow" (VAT) laminates.

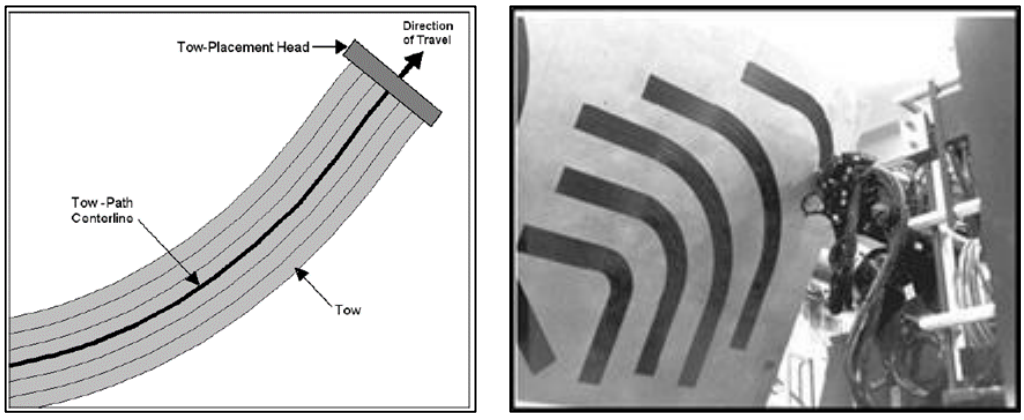


Figure 1-9. (a) Tow steering parameters, (b) Steered material courses [30]

Researchers have demonstrated that fiber steering expands the design space by offering increased tailoring flexibility with improved performance and weight savings. Early work performed by Hyer et al [31], [32] documented improvements that can be achieved in buckling performance with the use of curvilinear fiber orientations. Gurdal and Olmedo [33] studied the in-plane elastic response of variable stiffness panels. Gurdal et al. [34]-[36] investigated the design, analysis and manufacturing of VAT laminates for maximum buckling performance. Extensive research has also been devoted to modeling and analysis of curvilinear fiber paths [37]-[44]. Vibration studies have been conducted in [45]-[47] to demonstrate fundamental panel frequency performance improvements.

More recently, researchers have investigated the aeroelastic benefits of tow steering for wing structures. Beam and plate models [47]-[49] have been used to demonstrate trim and gust load reductions as well as increased flutter velocities over equivalent straight-fiber composites. Other recent investigations [50]-[52] have applied tow steering to optimize the NASA Common Research Model (CRM) using FEM based techniques. Stanford et al [50] showed up to 6% mass reductions for the CRM using maneuver load and flutter constraints. Brooks et al [51] demonstrated use of a coupled FEM/CFD methodology to perform a similar optimization study and reduce wing mass by 13%. Stodiek et al [52] optimized the CRM configuration and considered design constraints for gust loads, flutter stability and control effectiveness. Their results also indicated a reduction in mass over straight-fiber configurations. However, their framework is not appropriate for fast design assessments as one iteration could take up to 7 hours. Past research confirms the performance advantages for tow steered composites and a need for efficient design and analysis methodologies.

## 1.8 Scope of the Present Research

The objective of this work is to develop techniques that enable efficient design of aircraft wing skins constructed using automated fiber placement to steer fiber paths into optimal configurations. It is proposed that a primary fiber orientation exists for aircraft wings such that it minimizes weight and in general follows a non-linear path suitable for tow-steered laminate construction. This research is to be a proof-of-concept that demonstrates viability of a tow steered wing skin design framework. The approach will include consideration of geometry, aerodynamics, structures and manufacturing.

### *1.8.1 Proposed Optimization Problem*

The proposed optimization problem is to find a variable fiber orientation $\theta(x, y)$ and skin thickness distribution $t(x, y)$ that minimizes wing weight, subject to structural design criteria and manufacturing constrains. The problem is illustrated in Figure 1-10 which shows a continuously varying fiber path orientation ranging from $\theta_{root}$ at the wing root to $\theta_{tip}$ at the wing tip.

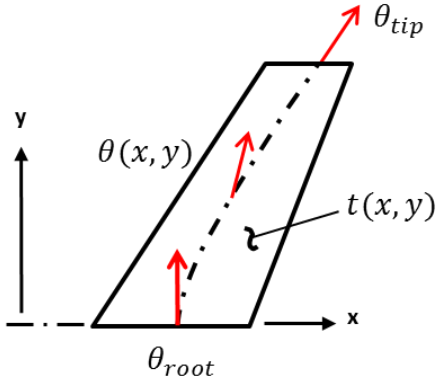


Figure 1-10. Wing skin design optimization problem.

### *1.8.2 Objective Function and Design Variables*

The design objective is to minimize the wing weight, given by

$$min\ f(x) \tag{1.1}$$

Wing skin laminate design variables $\{x\}$ are needed to describe ply orientations $\theta_k$ and ply thicknesses $t_k$ where *k=1,2,..,$N_{ply}$* and represents the index of the *k-th* ply. These variables are allowed to vary continuously with position $(x, y)$ on the wing plan form such that we may write

$$x = [\theta_k(x, y), t_k(x, y)] \tag{1.2}$$

### *1.8.3 Constraints*

Constraints are formulated to address design criteria which must be satisfied, including laminate strength, skin panel buckling stability and wing flutter. Manufacturing constraints are also needed to ensure optimized designs are producible. Constrains can be written as inequality functions $g(x)$, equality constraint functions $h(x)$, or side constraints $x_l$, $x_u$ and are given by equations (1.3), (1.4) and (1.5) . A detailed presentation of the constraint formulations is given in in Chapter 5.

$$g(x) \leq 0 \tag{1.3}$$

$$h(x) = 0 \tag{1.4}$$

$$x_l \leq x \leq x_u \tag{1.5}$$

## 1.9 Research Contributions

The main contributions of this research lie in development and application of methods to design and optimize tow steered laminates for aircraft wing skins. The developed methodology provides a flexible and integrated strategy to leverage advantages of tow steering to achieve more effective wing designs by including the coupling between OML geometry, aerodynamics and structural response.

A Ritz EPM is implemented to model orthotropic materials with variable fiber path geometry for a built-up wing construction using a parametric formulation. The approach also includes automated creation of finite element models to enable validation with higher fidelity analyses. The EPM structural model is coupled to a vortex lattice flow solver and implemented into an optimization framework. By using this approach we are more rapidly able to gain an understanding of optimal wing skin laminates that satisfy a variety of constrains and objective functions. The key features of this implementation are parameterization, flexibility and speed. The framework is suitable for conceptual and preliminary design of aircraft wing skins and has been applied to accomplish a tow-steered wing skin design.

# Chapter 2

## Geometric Modeling and Design Parameterization

This chapter provides the geometric modeling and parametrization used to describe the aircraft wing design problem. The 3D wing geometry is decomposed into a 2D planform representation that accommodates definition of tow steered laminated composite skins, a substructure layout and cross-sectional geometry.

### 2.1 Wing Geometry

Definition of three-dimensional wing geometry is enabled through the use of the OpenVSP [53] parametric aircraft geometry tool. OpenVSP allows creation of a 3D aircraft using common engineering parameters. It was originally developed at NASA by Gloudemans and others [54], [55]. A model can be generated interactively or automatically using its built-in scripting language and processed into formats suitable for engineering analysis. A particularly useful format is the degenerative geometry file developed by Belben [56] used to extract the geometry into three representations; a faceted 3D surface, a degenerative surface idealization, or a stick model as shown in Figure 2-1.

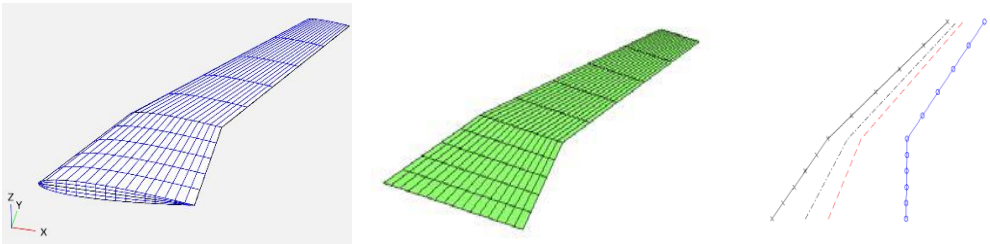

Figure 2-1. (a) 3D Geometry, (b) Degenerative Surface, (c) Stick Geometry.

The 3D model is used to extract wing geometry that is a function of the z-coordinate, such as OML surface points and section cuts at spar and rib centerlines. The mid-camber degenerative surface definition can be used to establish a planform reference plane for construction of wing segments and rib-spar centerlines. VSP also provides export of degenerated stick geometry for 1D idealizations. This study will rely on the 3D surface model and 2D degenerative surface geometry.

## 2.2 Wing Planform

The wing planform is modeled as an assembly of quadrilateral segments as shown in Figure 2-2. Each segment is defined by four grid points and transformed from the physical (x-y) domain to a local (ξ-η) computational domain as described in Appendix A. This makes it possible to select displacement basis functions with orthogonal properties and reduces the (ξ-η) computational domain to [−1< ξ,η <1]. It also facilitates mapping of fiber path orientations and simplifies application of boundary conditions.

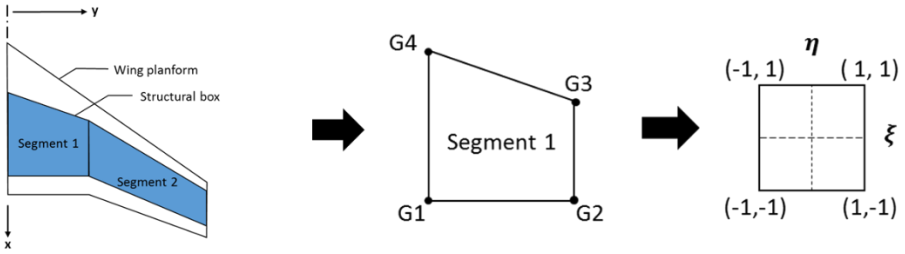


Figure 2-2. Wing Segment Geometry and Transformation to Computational Domain.

## 2.3 Wing Skin Laminate and Fiber Path Model

Wing skins are modeled as layers of orthotropic material positioned relative to the z = 0 reference plane. The 0-degree reference fiber direction is allowed to vary linearly from a value of $\theta_0$ at wing root to a value of $\theta_1$ at wing tip along the primary structural wing axis for a wing segment as shown in Figure 2-3(a).

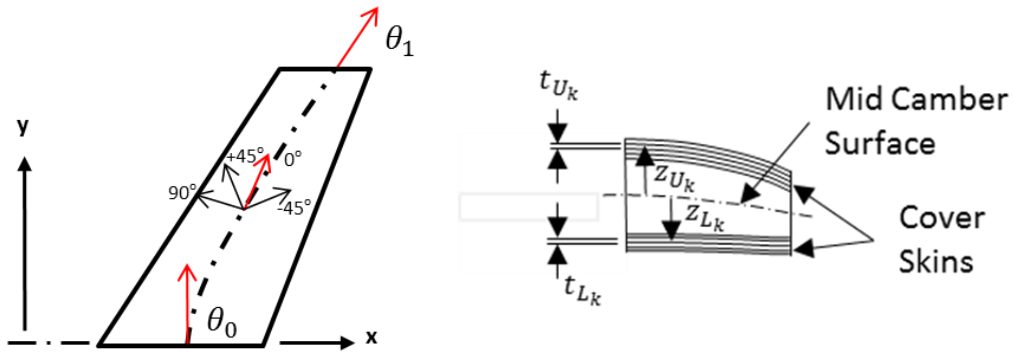


Figure 2-3. (a) Tow Steered Reference Fiber Path, (b) Wing skin laminate variables.

This is an extension of the linear variable curvilinear fiber path model introduced by Gurdal and Olmedo [33] and is defined by equation (2.1). This model has the advantages of offering a wide range of variable stiffness designs and provides closed form relations for the fiber path and steering radius of curvature.

$$\theta_k(x,y) = \emptyset_k + (\theta_1 - \theta_0)\frac{y}{s} + \theta_0 \tag{2.1}$$

Fiber orientations $\theta_k$ for each layer can vary independently or be positioned at fixed angles of $\emptyset_k$ = (0, +45, -45, 90) degrees relative to the 0-degree fiber. This provides the ability to steer laminate properties while preserving attractive manufacturing qualities. Skin layer thicknesses $t_{U_k}$, $t_{L_k}$ for the upper and lower skin, respectively, vary continuously across the wing planform surface and are modeled using orthogonal

Legendre polynomials given by the equation (2.2), where $t_{ij}$ are coefficients and $B_{ij}(\xi,\eta)$ are Legendre polynomials described in Appendix A. The functions are expressed in terms of a set of natural coordinates for a quadrilateral plate and can be transformed from its rectangular Cartesian system using equation (2.2)

$$t_{U_k}, t_{L_k}(\xi,\eta) = \sum_{i=0}^{I}\sum_{j=0}^{J} B_{ij}(\xi,\eta)t_{ij} \tag{2.2}$$

## 2.4 Rib-Spar Arrangement and Wing Skin Panels

Wing skins are supported by rib and spar substructure as illustrated in Figure 2-4. The default arrangement is based on an equal chord/span distribution and can be modified to user-defined configurations. Wing skins are subdivided into analysis panels based on this underlying rib-spar arrangement. The resulting skin panel geometries have arbitrary quadrilateral shape and are subject to a large number of in plane $\{N_x, N_y, N_{xy}\}$ and transverse pressure load conditions. The panel geometry is transformed to a (ξ-η) computational domain to facilitate panel buckling stability analyses described in [16].

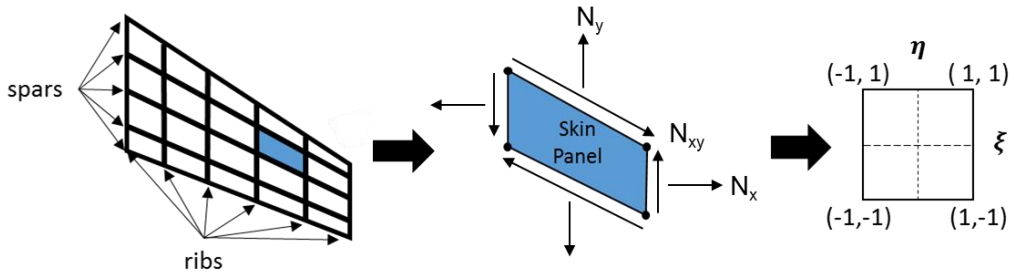


Figure 2-4. Wing substructure topology.

## 2.5 Wing Cross Section

Wing skins are supported by rib and spar structure as illustrated in Figure 2-5(a). The spars and ribs are modeled as assemblies of caps and webs as shown in Figure 2-5(b). Cross section variables are described by Table 2-1. All variables will be set to nominal values except for the rib and spar heights which are a function of position in the wing planform position and airfoil shape.

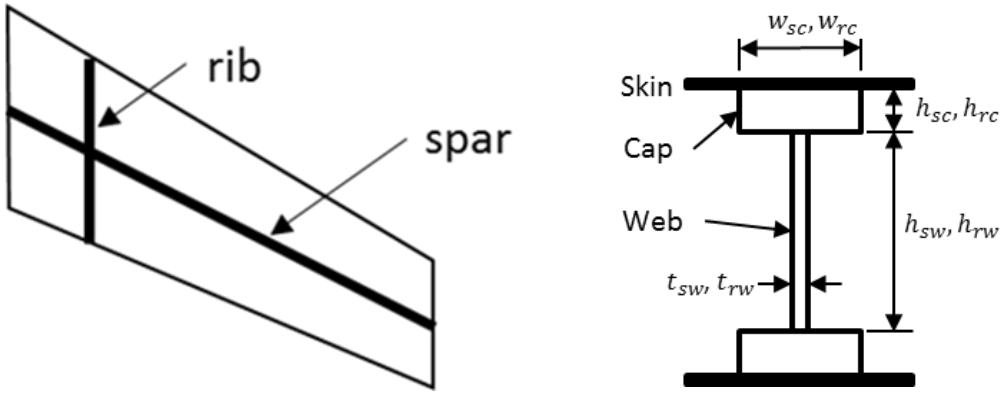


Figure 2-5. (a) Plan view of rib and spars, (b) Cross Section Variables for ribs and spars.

Table 2-1. Wing sub-structure cross-section variables.

| Section Variables | Description | Nominal Value |
|---|---|---|
| $w_{sc}, w_{rc}$ | Width of spar, rib cap | 2.0 in. |
| $t_{sc}, t_{rc}$ | Thickness of spar cap, rib cap | 0.20 in. |
| $h_{sw}, h_{rw}$ | Height of spar web, rib web | Varies with wing depth |
| $t_{sw}, t_{rw}$ | Thickness of spar web, rib web | 0.20 in. |

# Chapter 3

## Analysis Modeling and Development

This chapter describes the analysis models used in the design-analysis framework: the flow solver, structural solver, and an aero-structural coupling procedure.

### 3.1 Aerodynamics Model

The wing aerodynamics has been modeled using the VSPAero flow solver [57]. It provides flow solutions for two geometric representations of an aircraft configuration as shown in Figure 3-1. The first is shown in Figure 3-1b and based on a degenerative representation of the geometry, where fuselage surfaces are degenerated to a cruciform surface and lifting surfaces are modeled as camber surfaces. The final mesh is a mixture of quadrilaterals and triangles and is solved using the VLM. VSPAero also provides a panel method flow model by intersecting and trimming the faceted 3D VSP geometry for aircraft components (i.e. fuselage, wings, tails, etc.) to provide a mesh of quadrilaterals, triangles and general polygons Figure 3-1b. Control surfaces can be modeled explicitly as independent lifting surfaces or as sub-surfaces managed within a lifting surface component. Sub-surfaces can be rotated about a hinge line to interact with the flow.

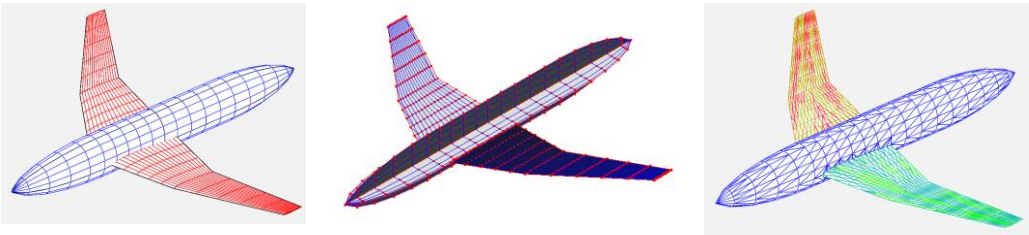

Figure 3-1. (a) VSP geometry, (b) degenerative VLM panel mesh, (c) 3D panel mesh.

VLM results are written to a .fem2d output file which describes the computational mesh and delta pressure data for each mesh element. Pressure loads are computed from these results and made available to the structural model.

## 3.2 Ritz Equivalent Plate Method

The Ritz EPM process is depicted in Figure 3-2 and has been implemented as a MATLAB numerical procedure. The 3D wing surface geometry is extracted as a degenerative geometry export file from OpenVSP and read directly by MATLAB. Analysis parameters are input to define the analysis problem type, polynomial degree, skin layer orientations and thickness, rib/spar geometry and rib/spar materials and section properties.

The wing mid-camber geometry is extracted from the OpenVSP file and mapped to the (ξ-η) domain as seen in Figure 3-2a-b. Gaussian quadrature integration points defined in the (ξ-η) space are used to compute a fiber path field representing the 0-degree tow-steered reference direction. Figure 3-2c-e shows the points are projected to the wing skin surfaces to obtain upper and lower offset heights $z_{U_k}, z_{L_k}$ for integration of skin strain energy equation terms. A similar technique is used to model the rib and spar elements to develop the static and eigenvalue analysis equations

$$\left[K_{\bar{q}}\right]\{\bar{q}\} = \left\{F_{\bar{q}}\right\} \tag{3.1}$$

$$\left[K_{\bar{q}} - \lambda M_{\bar{q}}\right]\{\bar{q}\} = 0 \tag{3.2}$$

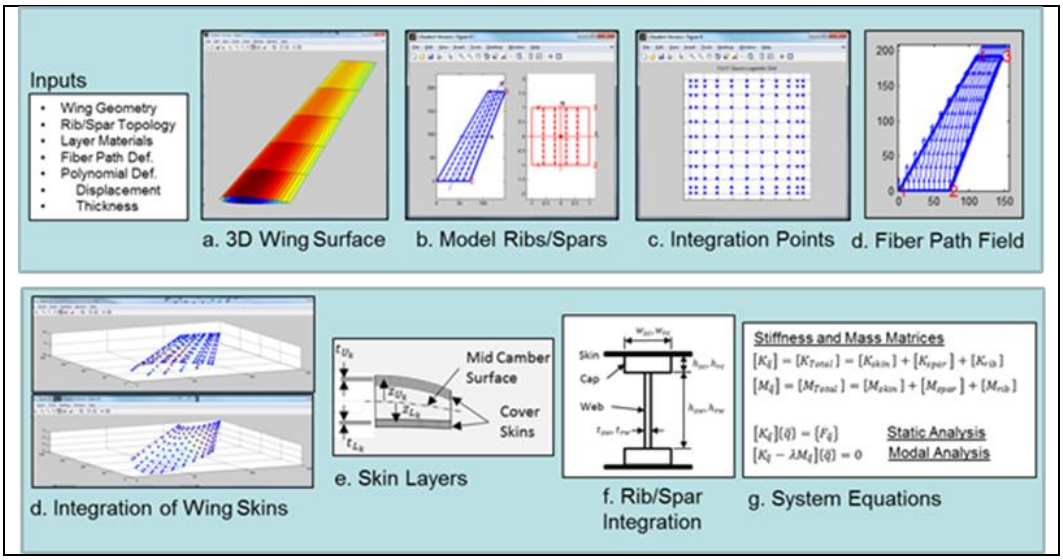


Figure 3-2. Ritz Equivalent Plate Modeling Process.

### 3.3 Finite Element Model

Wing finite element models were constructed using the workflow shown in Figure 3-3. The FEM is generated automatically from the same OpenVSP geometry as used in the Ritz EPM. It provides a rapid means to validate the Ritz solution and enables visualization of Ritz results mapped onto the FEM. The wing mid-camber geometry is extracted from the OpenVSP geometry and used to create a 2D planform mesh with element edge lengths sized to accommodate rib and spar structure. The 2D mesh is projected to the upper and lower wing surfaces to create a shell model of the wing. Beam elements are used to model spar and rib caps while webs are modeled using CQUAD4 elements. Composite skin layers were modeled using PCOMP property definitions with a SMEAR laminate stacking sequence definition to match the Ritz EPM. Local ply orientations are extracted at element centroids evaluated from the fiber path field. The FEM was solved using MSC.Nastran.

Inputs to the FEM process include the OpenVSP wing geometry file, a definition of the rib and spar topology, composite layer materials and a fiber path definition. The FEM mesh density is usually set to a value such that it agrees with the number of integration points used in the Ritz solution. It can also be refined to higher values for mesh refinement and resolution of structural responses.

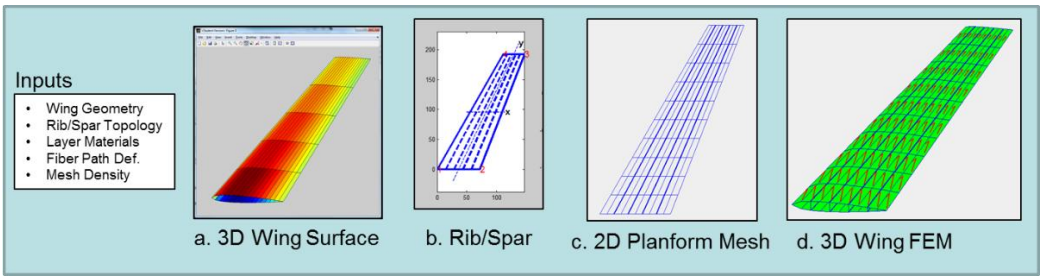


Figure 3-3. Wing finite element modeling process.

## 3.4 Aero-Structural Coupling

The aero-structural model and process flow described by Figure 3-4 was used to establish a coupling between the aerodynamic surface pressures and the structural deflections. The baseline outer mold line (OML) geometry is input to the aerodynamics solver to define surface pressure distributions. Aerodynamic surface pressures are coupled to the structural analysis model to compute deflections created by the flight condition. A comparison of the new displacement field is made with the previous iteration to determine if the structural displacements have converged. If not, the displaced OML geometry is updated with the new deflections and fed to the aerodynamics solver to start another iteration. This process continues until the structural deflections have converged to within an acceptable tolerance.

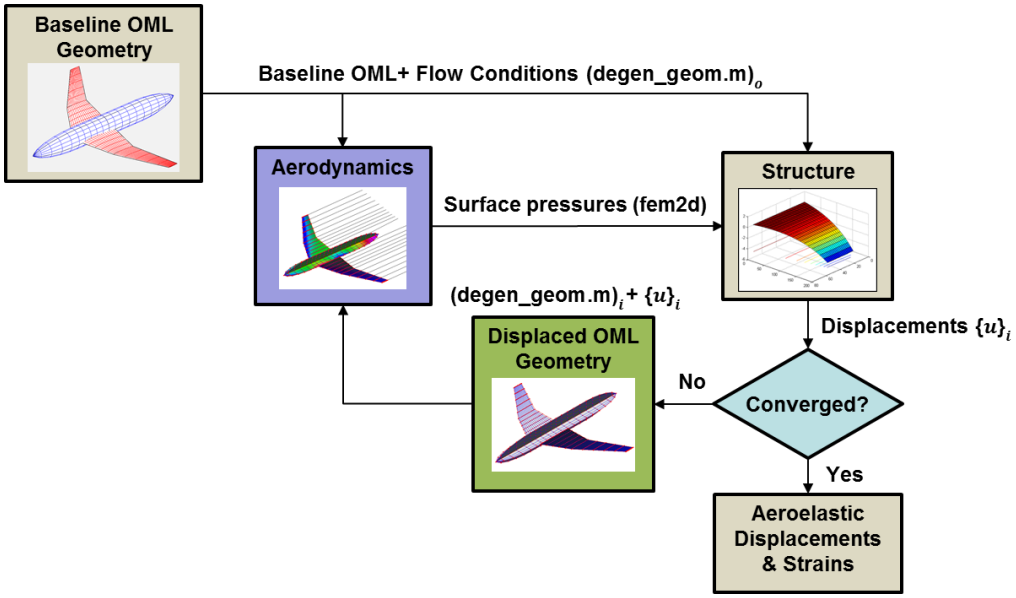


Figure 3-4. Aero-structural modeling process flow.

Coupling of the structural displacements to the OML aerodynamic surface is accomplished using the Ritz displacement field described in Appendix A. This is particularly convenient because the Ritz displacement equations are continuous and can be evaluated directly for any aerodynamic grid points.

### 3.5 Design Analysis Framework

The software components used in this research effort are shown schematically in Figure 3-5 and consist of open source, commercial and developed software. Open source components included the parametric aircraft design tool OpenVSP and its companion aerodynamic flow solver, VSPAero. Commercial applications include the MSC.Nastran general purpose finite element solver, the TMP/Slim/Vision finite element post-processing suite and the MATLAB numerics and visualization tool. The Ritz EPM wing application was written using the MATLAB programming language and integrated with the other components. Design optimization was also performed using MATLAB.

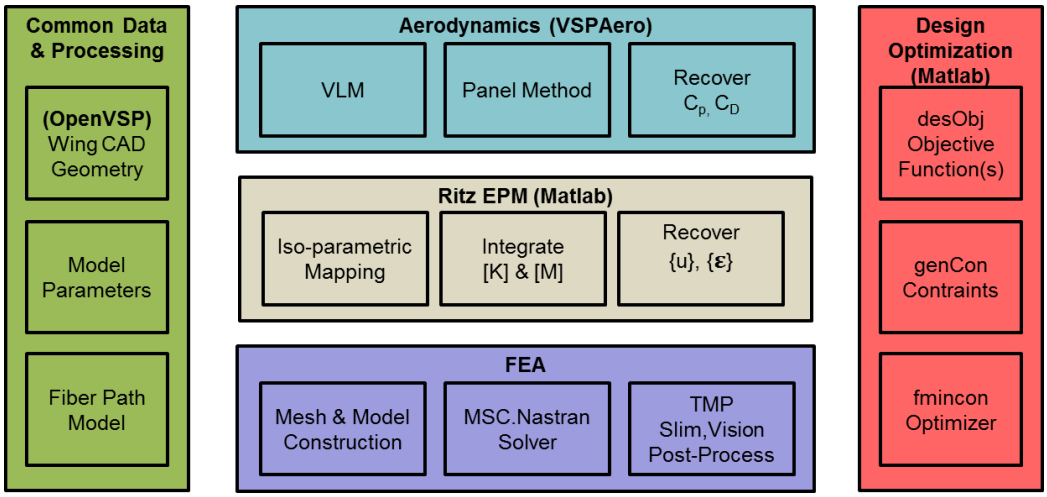


Figure 3-5. Software components used in this study.

# Chapter 4

## Analysis Validation

This chapter describes the work performed to validate the design analysis framework. Validation models were used to assess the accuracy of the modeling methods for various wing constructions clamped at the root. Results were generated for free vibration and static load conditions using Ritz EPM and the MSC.Nastran FEA solver. Appendix A describes the detailed results. Last, an aero-structural analysis coupling problem is evaluated.

### 4.1 Validation Models

Two planform geometries, uniform and swept, were chosen for the validation study as shown in Figure 4-1with parameters summarized in Table 4-1. Both have a span of 192 in., a root chord with of 72in. and a tip chord width of 35 in. The uniform wing has a rectangular air foil with a constant $t/c$ of 0.833. The swept wing uses a symmetrical NACA 0015 air foil with a $t/c$ of 0.15 at the root and 0.06 at the tip.

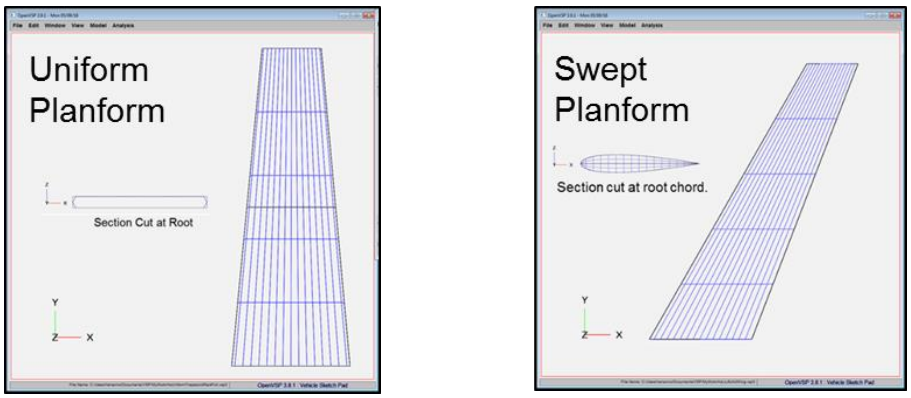


Figure 4-1. Validation Models (a) Uniform Planform, (b) Swept Planform.

Table 4-1. Wing planforms and sections.

| Parameter | Uniform Planform | Swept Planform |
|---|---|---|
| Half Span | 192 in. | 192 in. |
| Root Chord Width | 72 in. | 72 in. |
| Tip Chord Width | 36 in. | 36 in. |
| Sweep Angle | 5.5° | 30° |
| Air Foil | Rounded Rectangle | NACA 0015, NACA 0006 |
| t/c (root) | 0.0833 | 0.15 |
| t/c (tip) | 0.0833 | 0.06 |

Three different validation models of varying complexity were derived from the uniform and swept planforms as described in **Error! Reference source not found.**. Each model was analyzed to determine free vibration modes, wing bending due to pressure and twist due to torque. The trapezoidal plate represents a uniform trapezoid wing shaped surface constructed of isotropic material with a linearly varying thickness from root to tip. The core filled wing represents a uniform trapezoid with upper and lower unidirectional composite skins and full-depth honeycomb core. The tow steered wing represents a swept trapezoid wing with tow-steered composite skins and five supporting spars and ten ribs. Table 4-3 summarizes the materials and mechanical properties used in the analysis models.

Table 4-2. Validation model descriptions.

| Model | Planform | $N_{spar}$ | $N_{rib}$ | Skin Definition | Sub-structure |
|---|---|---|---|---|---|
| Trapezoidal Plate | Uniform | - | - | Linear Varying Thickness, $t_{root}$=0.180in., $t_{tip}$=0.090 | - |
| Core Filled Wing | Uniform | - | - | 4-Layer UD Laminate, [0/+45/-45/90] | Core |

| | | | | | |
|---|---|---|---|---|---|
| Tow Steered Wing | Swept | 5 | 10 | 4-Layer Tow Steered Laminate, [0/+45/-45/90] | Al |

Table 4-3. Materials and mechanical properties.

| Material | $E_1$ (Msi) | $E_2$ (Msi) | $G_{12}$ (Msi) | $\nu_{12}$ | $\rho$ (lb/in$^3$) |
|---|---|---|---|---|---|
| Aluminum (Al) | 10 | - | | 0.3 | 0.10 |
| Carbon/Epoxy (C/Ep) | 22.15 | 1.38 | 0.86 | 0.321 | 0.058 |
| Honeycomb (Core) | 0.68 | 0.68 | 0.26 | | .00231 |

## 4.2 Trapezoidal Plate

Analyses were performed using the Ritz EPM and FEA models shown in Figure 4-2, respectively. The EPM utilized a polynomial of degree 11 with 605 DOF and the FEM model employed 880 shell CQUAD4 elements, 160 beam elements representing the spar caps and 882 nodes with 5292 DOF. Comparisons are made in Figure 4-3 of free vibration results between the Ritz EPM and those obtained from FEA using MSC.Nastran. The EPM utilized a polynomial of degree 11 with 605 DOF and the FEM model employed 144 shell CQUAD4 elements and 169 nodes with 1014 DOF. The first 10 Ritz EPM modes lie within a range of -1.93% to +0.12% of the FEA results.

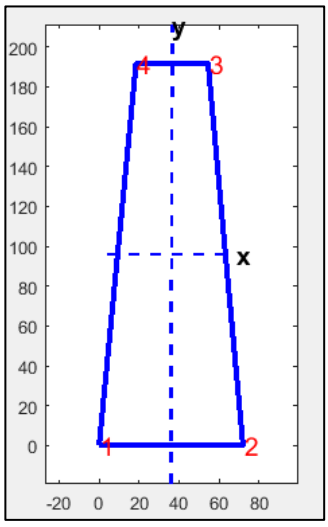


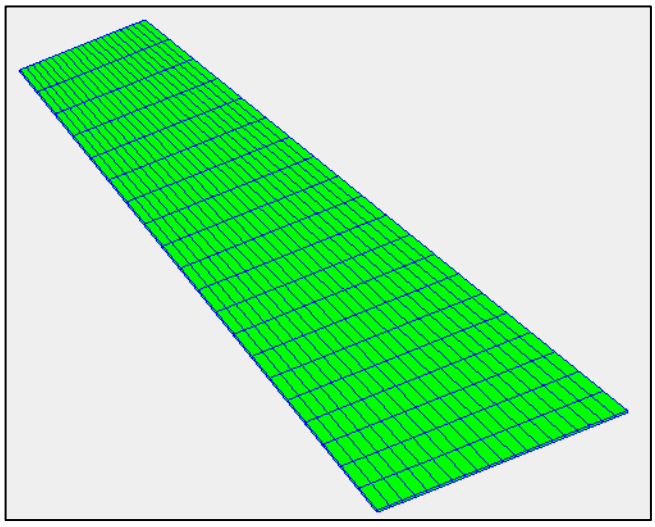

Figure 4-2. Analysis meshes for Ritz EPM and FEM of trapezoidal plate.

A comparison of the first four mode shapes is given in Figure 4-4 and Figure 4-5 where it is seen that the mode shapes are in good agreement.

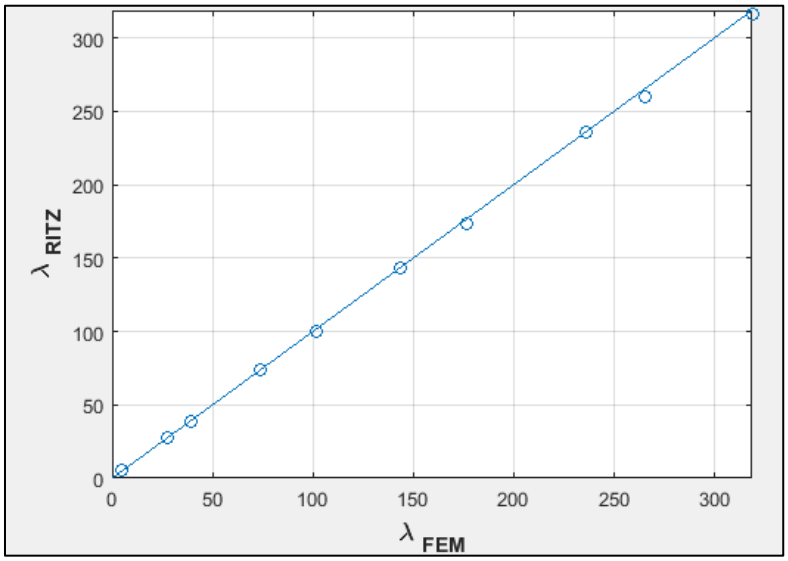


Figure 4-3. EPM and FEM free vibration eigenvalues for trapezoidal plate.

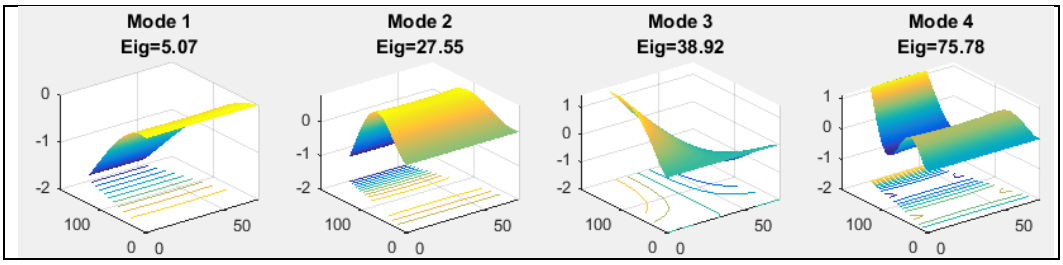


Figure 4-4. Ritz EPM free vibration mode shapes of trapezoidal plate.

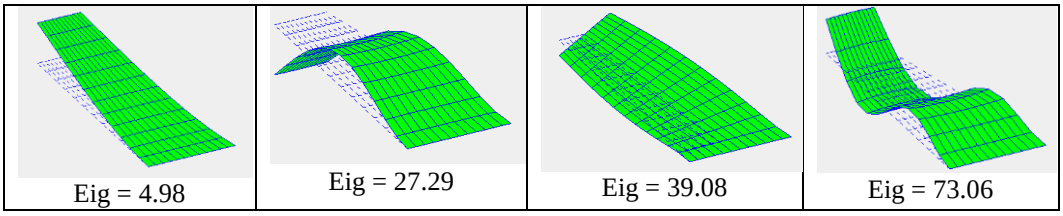


Figure 4-5. FEM free vibration mode shapes of trapezoidal plate.

Comparisons are made in Figure 4-6 and Figure 4-7 between Ritz EMP and FEA for deflections and principal strains due to bending under a uniform pressure of p = -0.05 psi. It can be seen that there is good agreement between the Ritz and FEA results.

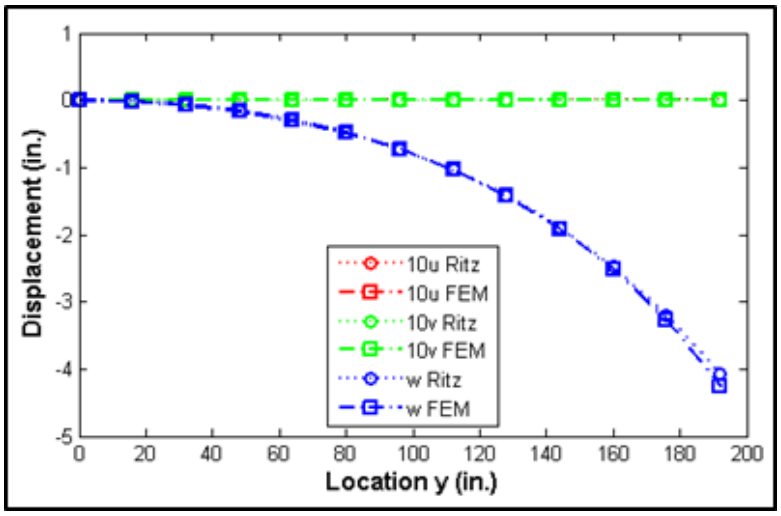


Figure 4-6. Comparison of trapezoidal plate displacements for bending case.

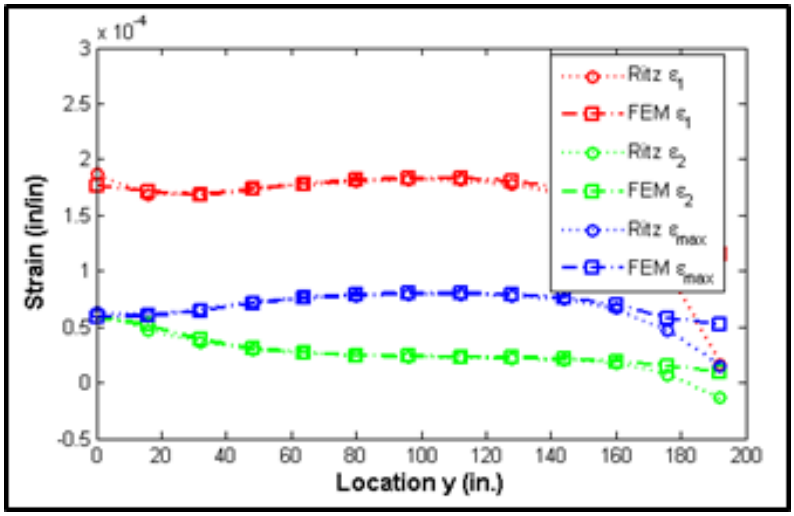


Figure 4-7. Comparison of trapezoidal plate principal strains for bending case.

Comparisons are made in Figure 4-8 and Figure 4-9 between Ritz EMP and FEA for deflections and principal strains resulting from a tip torque +/- 1 lb. applied to the leading and trailing edge tip. The results agree well between Ritz and FEA.

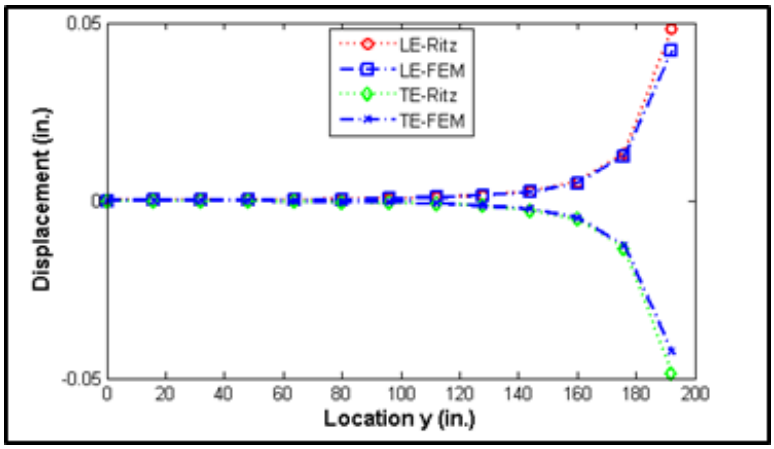


Figure 4-8. Comparison of LE and TE deflections for tip torque.

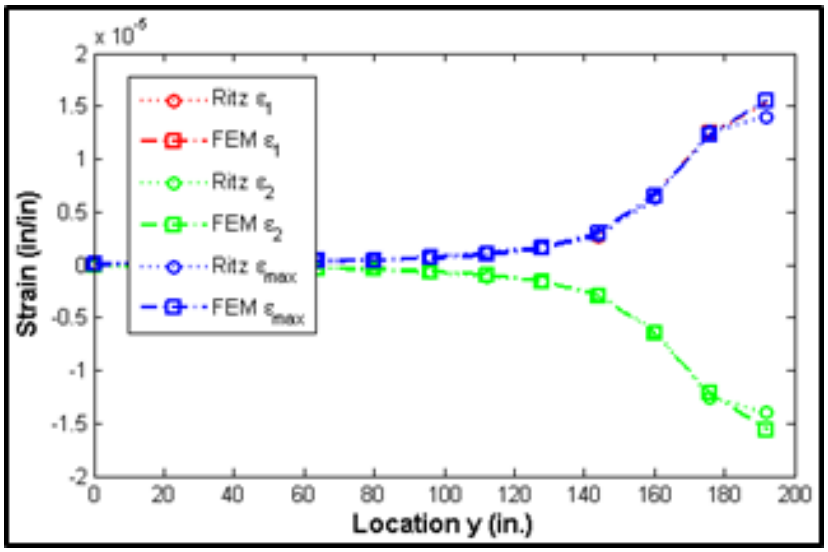


Figure 4-9. Comparison of LE and TE principal strains for tip torque.

### 4.3 Core Filled Wing

Analyses were performed using the Ritz EPM and FEA models shown in Figure 4-10. Comparisons are made in Figure 4-11 of free vibration results between the Ritz EPM and those obtained from FEA. The EPM utilized a polynomial of degree 11 with 605 DOF and the FEM model employed 288 shell CQUAD4 elements, 144 solid (CPENTA, CHEXA) elements and 338 nodes with 2028 DOF. It can be seen that modes 1, 2, 4 and 5 computed using EPM lie within -5.93% of the FEA results and the other modes lie between -20.58% and 25.22%.

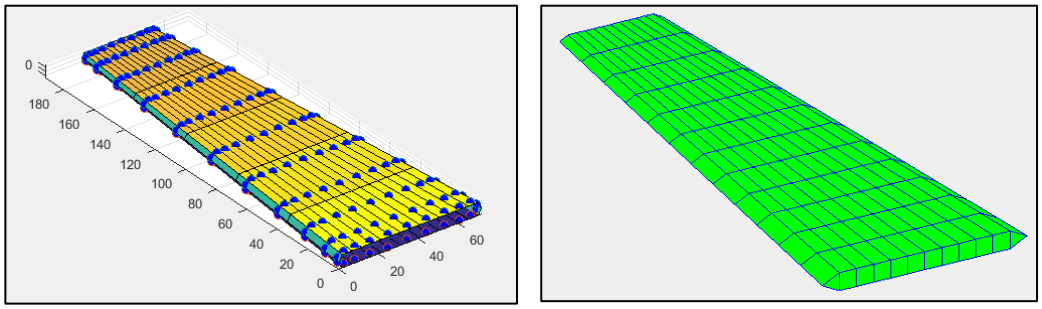


Figure 4-10. Analysis meshes for Ritz EPM and FEM of core filled wing.

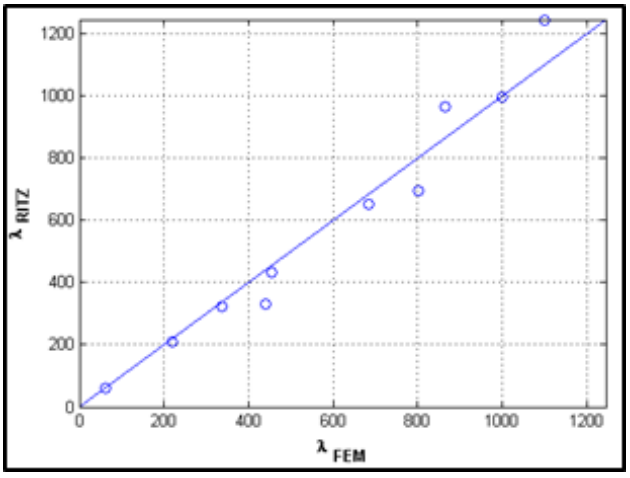


Figure 4-11. Comparison of free vibration eigenvalues for core filled wing.

Comparisons are made in Figure 4-12 between Ritz EMP and FEA for deflections and in Figure 4-13 for principal strains resulting from a uniform pressure loading of p=-0.5psi. The displacement results agree well between Ritz and FEA.

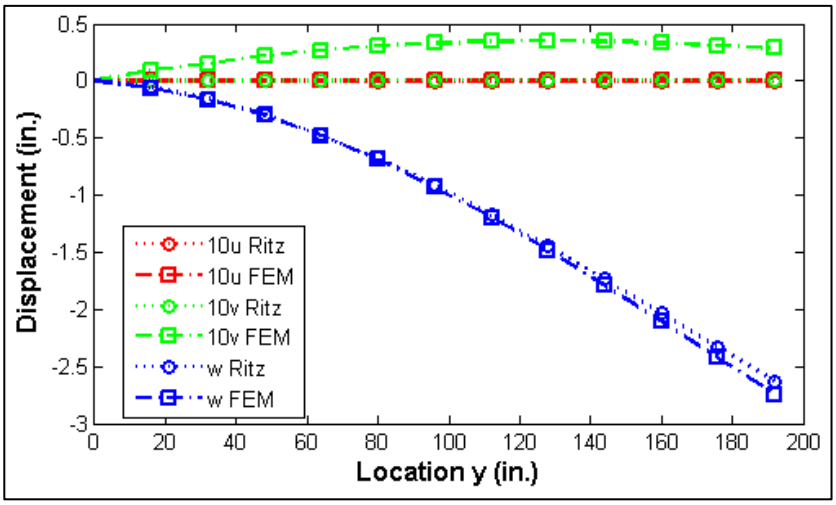


Figure 4-12. Ritz EMP and FEM displacements for bending of core filled wing.

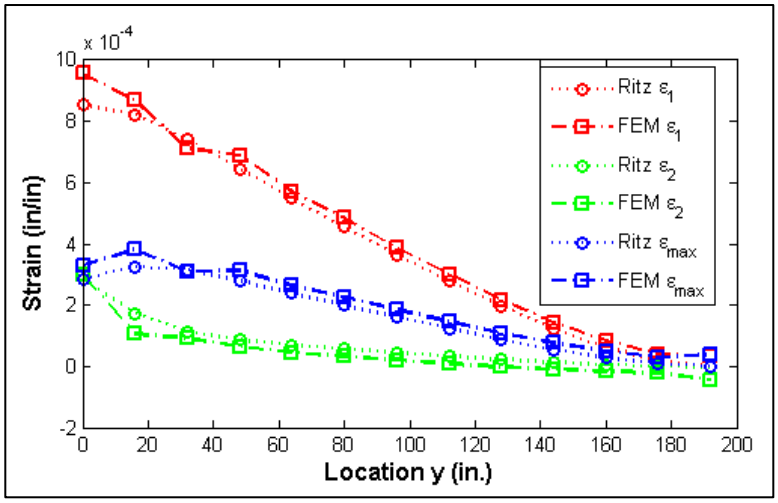


Figure 4-13. Comparison of EPM and FEM strains for bending of core filled wing.

Comparisons are made in Figure 4-14 and Figure 4-15 between Ritz EPM and FEA for deflections and principal strains resulting from a tip torque load condition. The torque loading was defined by a unit load acting on the leading edge tip in the +z direction and a unit loading acting on the trailing edge tip in the –z direction. The results trend agrees reasonably well between Ritz and FEA but shows growing departure in the span direction.

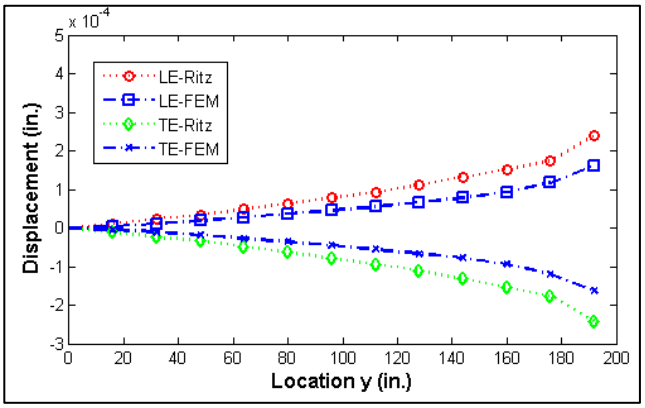


Figure 4-14. Comparison of LE and TE displacements for tip torque of solid wing.

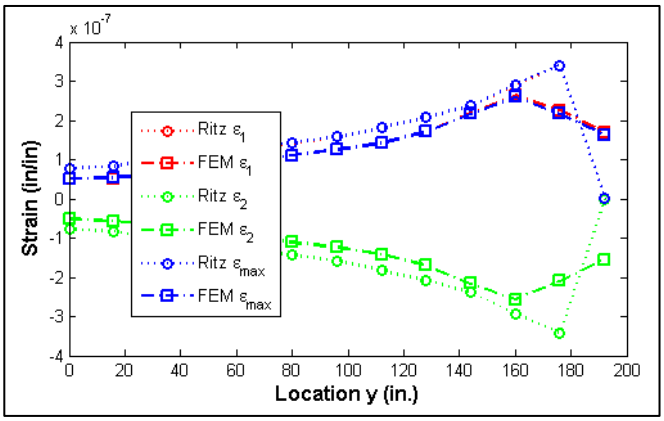


Figure 4-15. Comparison of LE and TE principal strains for tip torque of solid wing.

## 4.4 Tow Steered Wing

A built-up wing with tow steered skins was defined to evaluate structural response of variable fiber paths. Skins include four tow-steered layers as shown in the plot of Figure 4-16. The reference 0-degree path varies linearly from wing to tip as given by Eq. (3) and has an initial orientation of 0-degrees at the root and -30-degrees at the tip. The +45, -45 and 90 layers are linked to the 0-degree reference path and follow the same variation. The upper and lower skins use the same definition. The skins are supported by 5 evenly distributed spars and 10 ribs.

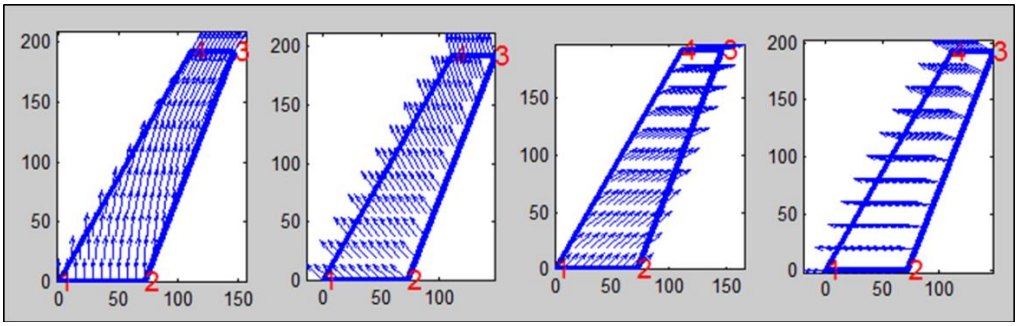

Figure 4-16. Fiber path fields for 0/+45/-45/90 layers of tow steered wing.

Analyses were performed using the Ritz EPM and FEA models shown in Figure 4-17, respectively. The EPM utilized a polynomial of degree 11 with 605 DOF and the FEM model employed 880 shell CQUAD4 elements, 160 beam elements representing the spar caps and 882 nodes with 5292 DOF.

Comparisons of free vibration eigenvalues are made in Figure 4-18. The modes computed using EPM lie within a range of -2.6% and +1.76% of the FEA results.

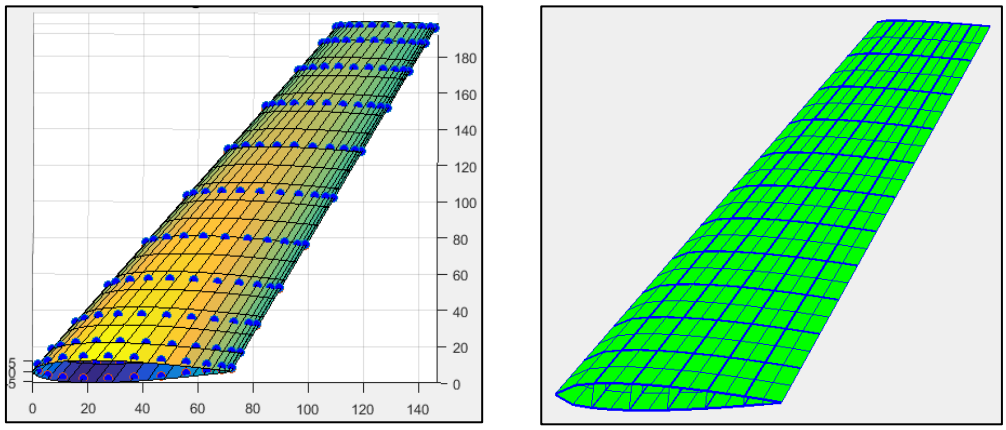


Figure 4-17. Analysis meshes for Ritz EPM and FEM of tow steered wing.

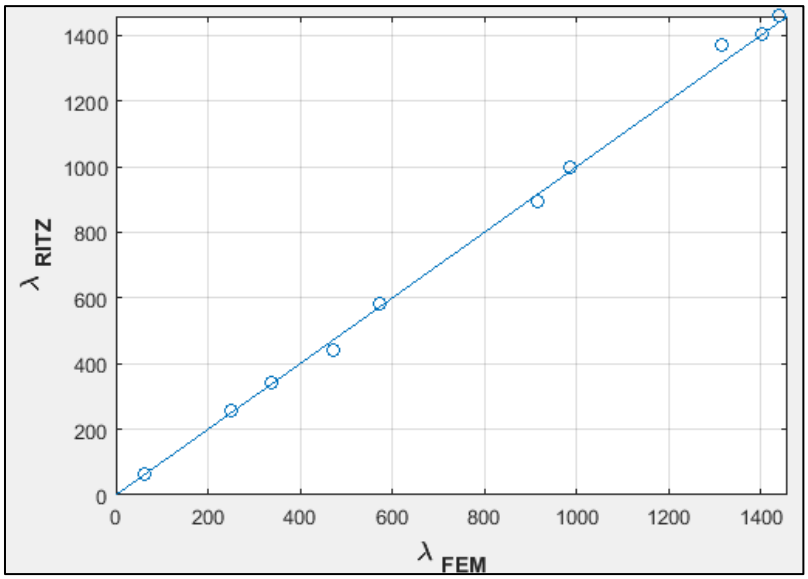


Figure 4-18. Ritz EPM and FEM free vibration eigenvalues for tow steered wing.

A comparison of the first four mode shapes is given in Figure 4-19 and Figure 4-20. It is seen that mode shapes 1, 2 and 4 are in good agreement. However, there is a difference between Ritz mode 3, shown as torsion, and FEM mode 3, shown as in-plane bending. There is no explanation offered for the difference at this time.

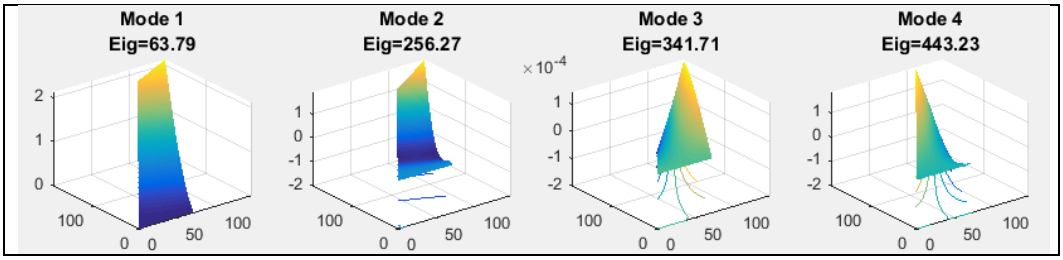


Figure 4-19. Ritz EPM free vibration mode shapes for tow steered wing.

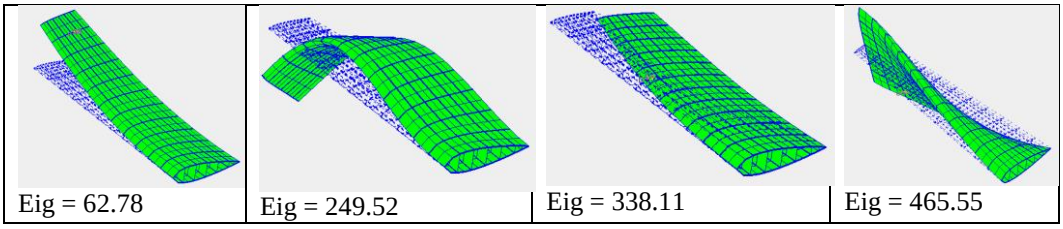


Figure 4-20. FEM free vibration mode shapes for tow steered wing.

Comparisons are made in Figure 4-21and Figure 4-22 between Ritz EPM and FEA for deflections and principal strains resulting from a uniform pressure loading. The displacement and strain results agree reasonably well and exhibit consistent trends between Ritz and FEA, but the principal strains show significant disagreement particularly for the prinicipal shear strain at the wing root.

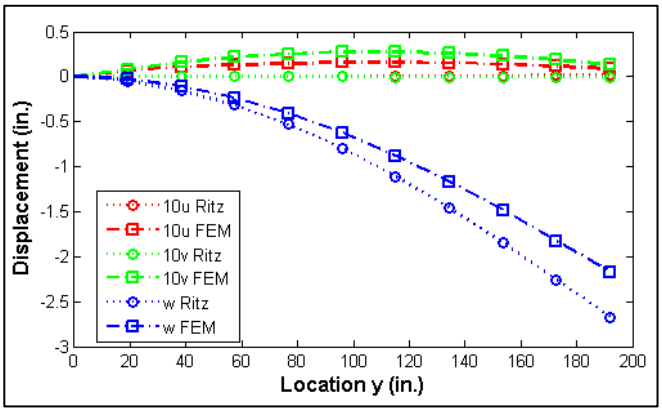


Figure 4-21. Ritz EPM and FEM displacements for bending of tow steered wing.

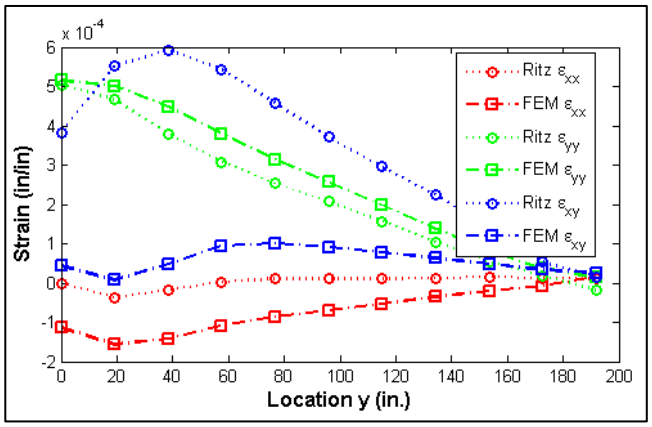


Figure 4-22. Ritz and FEM results for uniform pressure loading of tow steered wing

Comparisons are made in Figure 4-23 and Figure 4-24 between Ritz EPM and FEA for deflections and strains resulting from a unit tip torque load condition. The displacement results agree well between Ritz and FEA.

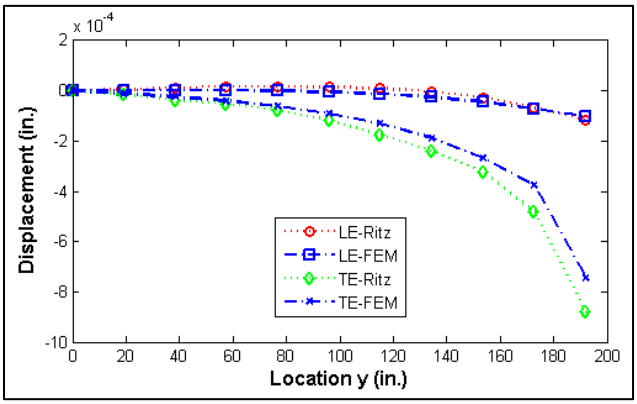


Figure 4-23. Comparison of LE and TE displacements for tip torque of tow steered wing.

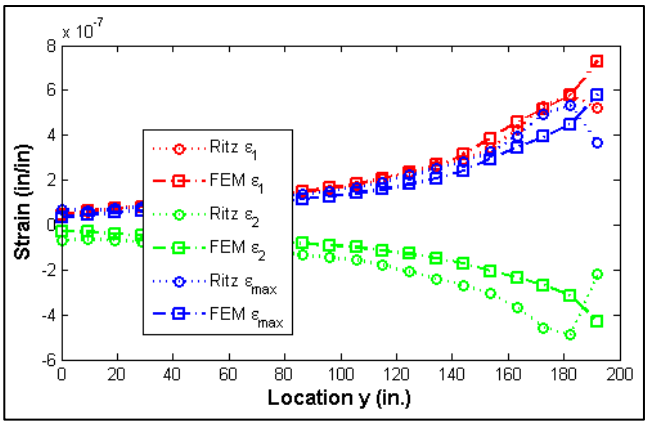


Figure 4-24. Ritz EPM and FEA results for tip torque loading of tow steered wing.

## 4.5 Efficiency Comparisons

A comparison of efficiency between the Ritz EPM and FEA has been made in Table 4-4. Details in terms of degrees of freedom (DOF) and run time for each of the wing analyses has been compared between EPM using polynomial orders ranging from $Np$= 4 to 14. Run times between EPM ($Np$=4, 6, 8) and FEA are generally comparable and typically less than 10 seconds for all wing constructions. However, substantial increases in run time result using EPM at $N_p \geq 10$ as shown in Figure 4-25.

Solution times between Ritz EPM and FEA are comparable at the lover polynomial orders ranging between $Np$=4, 6, 8. FEA solution times are seen to be generally insensitive to the DOF in this investigation and are significantly faster that Ritz EPM at higher polynomial orders of $N_p \geq 10$. It was concluded that $N_p \leq 8$ would be used for design studies.

This efficiency comparison should be considered somewhat qualitative since the EPM was coded in MATLAB m-file code and MSC/NASTRAN is coded in FORTRAN and highly optimized. Recoding EPM using a compiled language such as FORTRAN or C++ would provide a more direct comparison of computational effort.

Table 4-4. Efficiency comparison of Ritz EPM and FEA

| Trapezoidal Plate | | | | | Core Filled Wing | | | | | Tow Steered Wing | | | | |
|---|---|---|---|---|---|---|---|---|---|---|---|---|---|---|
| EPM | | | FEA | | EPM | | | FEA | | EPM | | | FEA | |
| Np | DOF | Time | DOF | Time | Np | DOF | Time | DOF | Time | Np | DOF | Time | DOF | Time |
| 4 | 80 | 0.17 | 1014 | 0.98 | 4 | 80 | 0.966 | 2028 | 1.31 | 4 | 80 | 3.05 | 4332 | 2.61 |
| 6 | 180 | 0.15 | 1014 | 1.01 | 6 | 180 | 1.59 | 2028 | 1.37 | 6 | 180 | 4.78 | 4332 | 2.51 |
| 8 | 320 | 1.44 | 1014 | 0.92 | 8 | 320 | 4.62 | 2028 | 1.34 | 8 | 320 | 10.32 | 4332 | 2.60 |
| 10 | 605 | 3.57 | 1014 | 0.97 | 10 | 605 | 16.1 | 2028 | 1.35 | 10 | 605 | 30.23 | 4332 | 2.50 |
| 12 | 720 | 10.19 | 1350 | 1.23 | 12 | 720 | 43.38 | 2700 | 1.59 | 12 | 720 | 64.79 | 4332 | 2.57 |
| 14 | 980 | 23.53 | 1734 | 1.17 | 14 | 980 | 102.61 | 3468 | 1.67 | 14 | 980 | 134.37 | 4332 | 2.56 |

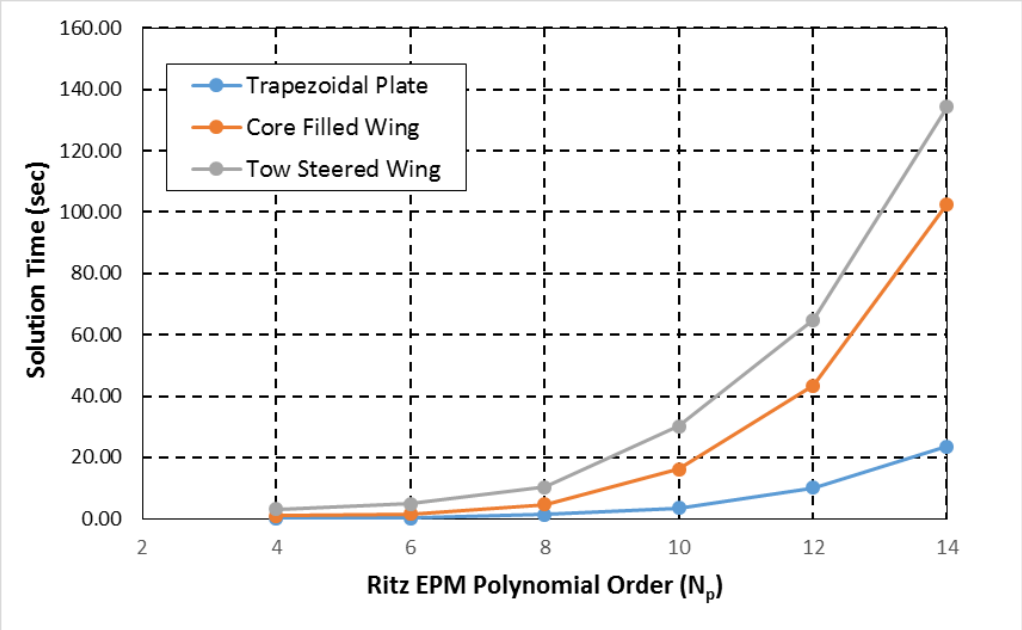


Figure 4-25 . Ritz EPM solution times for various wing constuctions.

### 4.6 Panel Buckling Stability

Panel buckling stability is a critical design criteria for sizing wing skin thickness and sub-structure layout. Internal skin load distributions are applied as panel boundary loads and buckling eigenvalues are computed. The Ritz method reported in [16] was used to develop buckling solutions and comparisons have been made here with FEA to validate their accuracy. This section presents a summary of results for test cases given in Table 4-5, taken from Appendix B. Laminate definitions were selected from [35], [37] and are described in Table 4-6. Composite material properties are given in Table 4 7.

Table 4-5. Summary of buckling validation cases.

| Panel Geometry | Loads | Laminate | BCs |
|---|---|---|---|
| a=b=10 | $N_x$=-100 lb/in | QI, AP, $VAT^1$, $VAT^2$, $VAT^3$ | SSSS, CCCC, CFFF |
| Quad | $N_x$=-100; $N_y$=-10 | QI, AP, $VAT^1$ , $VAT^2$, $VAT^3$ | SSSS, CCCC, CFFF |

Table 4-6. Buckling panel laminate descriptions.

| Laminate | Stacking Sequence | $N_{ply}$ |
|---|---|---|
| QI | $[0/+45/-45/90]_S$ | 8 |
| AP | $[+45/-45/+45/-45]_S$ | 8 |
| $VAT^1$ | $[<-45\|45>,<45\|-45>]_{2S}$ | 8 |
| $VAT^2$ | $[<0\|45>,<0\|-45>]_{2S}$ | 8 |
| $VAT^3$ | $[90<0\|45>,90<0\|-45>]_{2S}$ | 8 |

Table 4-7. Lamina mechanical properties.

| $E_1$(Msi) | $E_2$(Msi) | $G_{12}$(Msi) | $\nu_{12}$ | $\rho$(lb/in$^3$) | $t_{ply}$(in) |
|---|---|---|---|---|---|
| 22.15 | 1.38 | 0.86 | 0.321 | 0.058 | .0053 |

A description of the panel fiber paths and the distribution of engineering laminate stiffness as a function of panel position are presented in Figure 4-26 through Figure 4-28. These laminates provide good examples of property tailoring using linear variable fiber path geometry. The VAT1 laminate has two regions near the panel edges where the stiffness is maximized. The VAT2 laminate is designed to achieve maximum Ex stiffness in the middle of the panel, whereas the VAT3 laminate provides a maximum Ey stiffness in the middle of the panel.

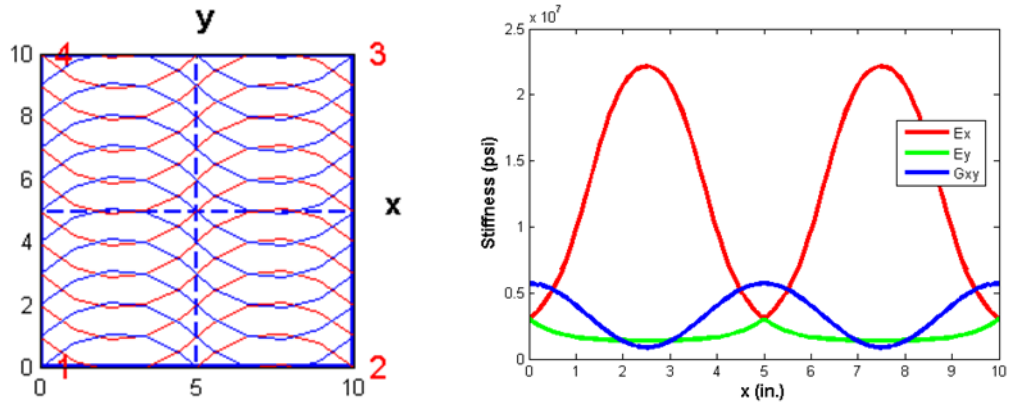


Figure 4-26. Fiber paths and laminate engineering constants for VAT1 laminate.

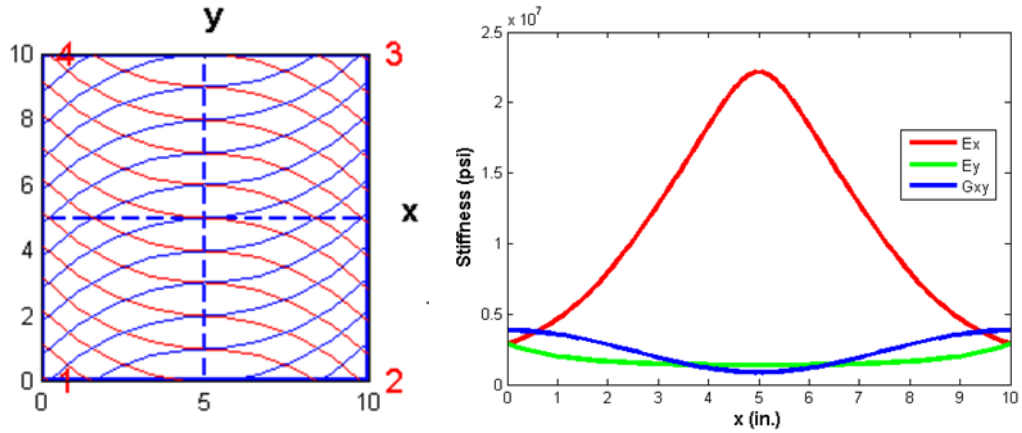


Figure 4-27. Fiber paths and laminate engineering constants for VAT2 laminate.

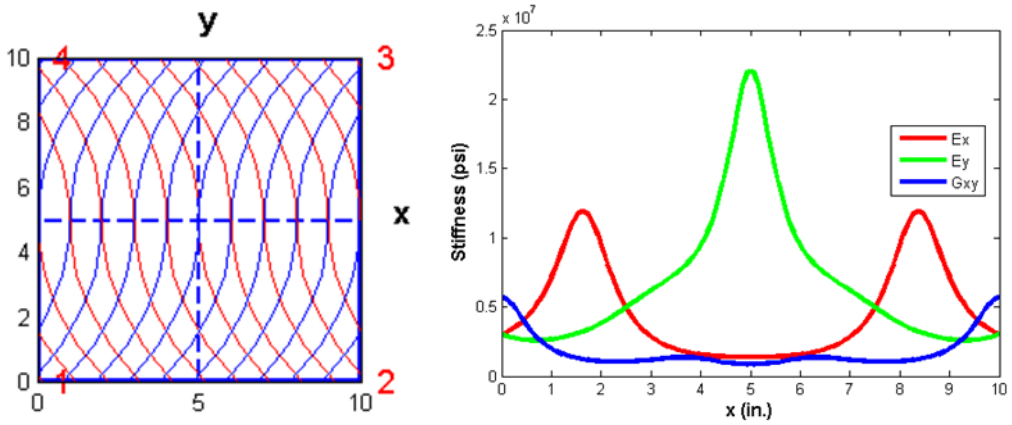


Figure 4-28. Fiber paths and laminate engineering constants for VAT3 laminate.

A comparison of buckling factor results for Ritz and FEA methods is given in Figure 4-29 and Table 4-8. Ritz and FEA buckling factor comparison for Nx loading. Similar results are given in Figure 4-30 and Table 4-9 for $N_y$ loading. The Ritz $N_x$ solutions agree within 3% of the FEM results with exception of the fully clamped cases and the simply supported angle ply laminate. The $N_y$ cases generally produced the same trends as $N_x$ loading but with larger errors.

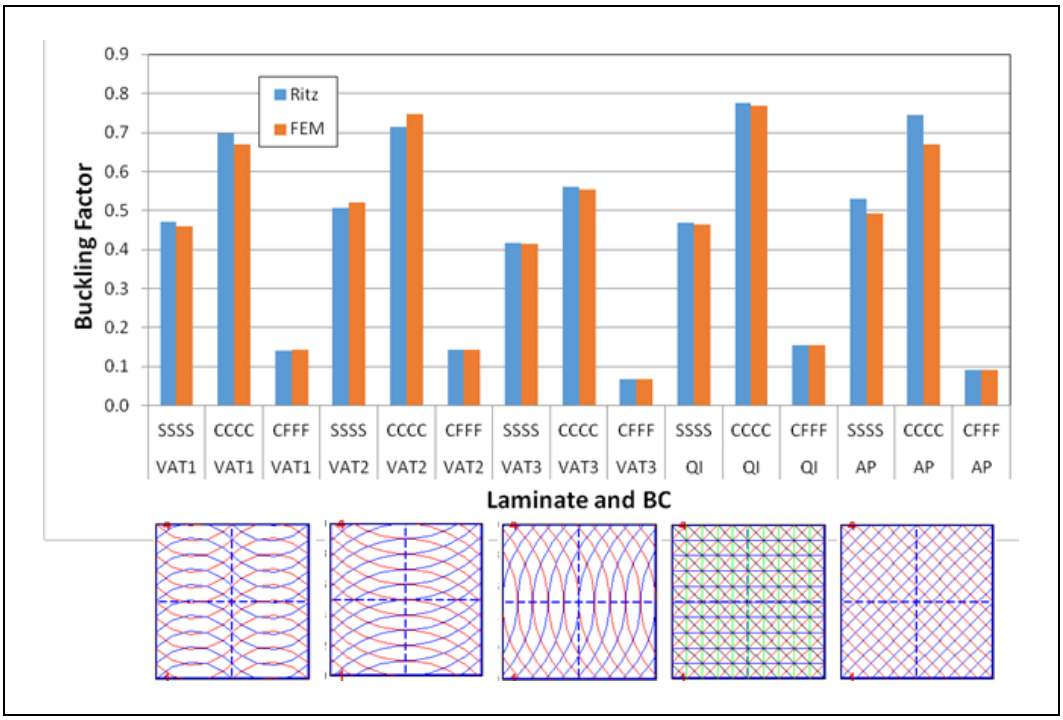


Figure 4-29. Buckling load factors for $N_x$ loading on square laminated panels.

Table 4-8. Ritz and FEA buckling factor comparison for $N_x$ loading.

| Laminate | BC | Buckling Factor | | % Error |
|---|---|---|---|---|
| | | Ritz | FEM | |
| VAT1 | SSSS | 0.470 | 0.460 | 2.13 |
| VAT1 | CCCC | 0.697 | 0.758 | -7.97 |
| VAT1 | CFFF | 0.141 | 0.142 | -0.51 |
| VAT2 | SSSS | 0.507 | 0.520 | -2.61 |
| VAT2 | CCCC | 0.714 | 0.840 | -14.99 |
| VAT2 | CFFF | 0.143 | 0.143 | 0.03 |
| VAT3 | SSSS | 0.417 | 0.413 | 0.78 |
| VAT3 | CCCC | 0.562 | 0.954 | -41.11 |
| VAT3 | CFFF | 0.069 | 0.068 | 0.09 |
| QI | SSSS | 0.469 | 0.464 | 1.08 |
| QI | CCCC | 0.777 | 0.976 | -20.37 |
| QI | CFFF | 0.154 | 0.154 | -0.05 |
| AP | SSSS | 0.530 | 0.493 | 7.49 |
| AP | CCCC | 0.745 | 0.977 | -23.81 |
| AP | CFFF | 0.091 | 0.091 | -0.12 |

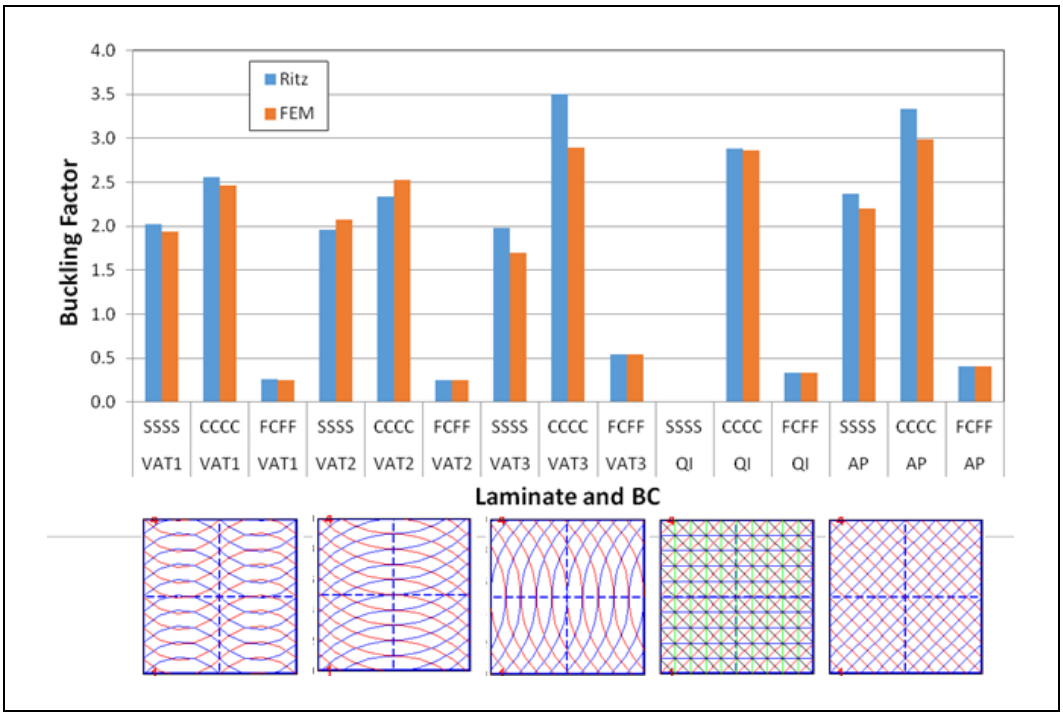


Figure 4-30. Buckling load factors for $N_y$ loading of square laminated panels.

Table 4-9. Ritz and FEA buckling factor comparison for $N_y$ loading.

| Laminate | BC | Buckling Factor | | Ratio | % Error |
|---|---|---|---|---|---|
| | | Ritz | FEM | | |
| VAT1 | SSSS | 1.516 | 1.419 | 1.069 | 6.85 |
| VAT1 | CCCC | 0.800 | 0.879 | 0.909 | -9.05 |
| VAT1 | CFFF | 0.213 | 0.195 | 1.092 | 9.23 |
| VAT2 | SSSS | 1.486 | 1.548 | 0.960 | -3.98 |
| VAT2 | CCCC | 1.826 | 3.105 | 0.588 | -41.18 |
| VAT2 | CFFF | 0.205 | 0.191 | 1.070 | 6.97 |
| VAT3 | SSSS | 1.577 | 1.263 | 1.248 | 24.79 |
| VAT3 | CCCC | 2.732 | 2.829 | 0.966 | -3.43 |
| VAT3 | CFFF | 0.441 | 0.427 | 1.032 | 3.19 |
| QI | SSSS | 1.588 | 1.511 | 1.051 | 5.11 |
| QI | CCCC | 2.260 | 2.762 | 0.818 | -18.16 |
| QI | CFFF | 0.584 | 0.730 | 0.800 | -19.96 |
| AP | SSSS | 1.836 | 1.637 | 1.121 | 12.11 |
| AP | CCCC | 2.635 | 3.293 | 0.800 | -19.98 |
| AP | CFFF | 0.331 | 0.310 | 1.069 | 6.90 |

A similar comparison between Ritz and FEA has been made for a quadrilateral panel configuration given in Figure 4-31. The validation cases are given in Table 4-5 and laminate definitions are provided in Table 4-6. A comparison of buckling factor results for Ritz and FEA methods is given in Figure 4-32 and Table 4-10 for $N_x$ loading. Similar results are given in Figure 4-33 and Table 4-11 for $N_y$ loading. The Ritz and FEM generally results agree within 10% for the $N_x$ loading. Similar to the square plate results, the $N_y$ cases also produced correlation trends consistent $N_x$ loading but have larger disagreement with the FEM. It can be concluded that the Ritz buckling solutions are suitable for conceptual and preliminary design activities, especially where many different configurations are being evaluated.

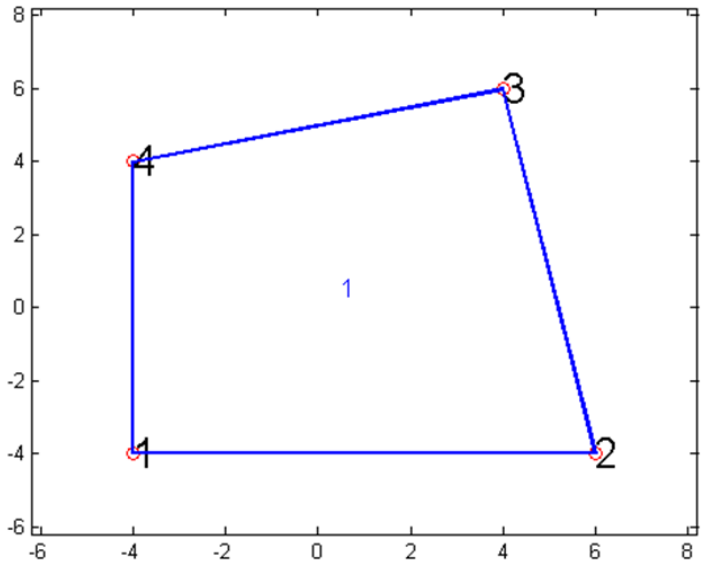


Figure 4-31. Quadrilateral panel configuration used for buckling validation.

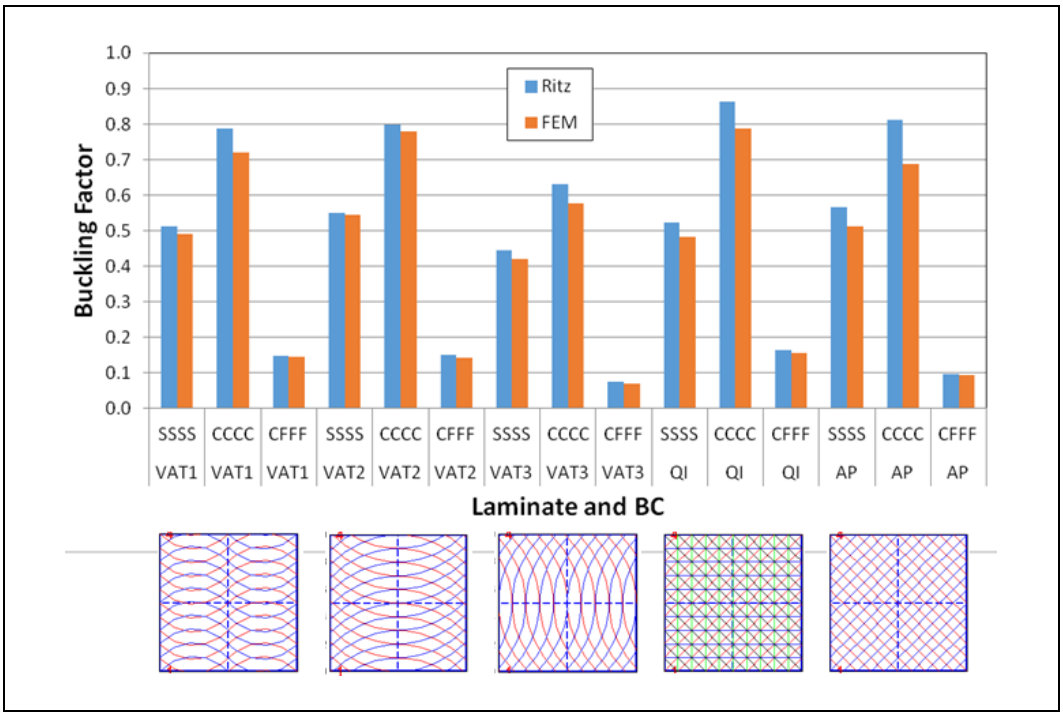


Figure 4-32. Ritz and FEA buckling factors for quadrilateral panel with $N_x$ loads.

Table 4-10. $N_x$ buckling factors for quadrilateral panels.

| Laminate | BC | Buckling Factor | | % Error |
|---|---|---|---|---|
| | | Ritz | FEM | |
| VAT1 | SSSS | 0.513 | 0.490 | 4.60 |
| VAT1 | CCCC | 0.788 | 0.798 | -1.21 |
| VAT1 | CFFF | 0.148 | 0.144 | 2.54 |
| VAT2 | SSSS | 0.549 | 0.545 | 0.76 |
| VAT2 | CCCC | 0.800 | 0.879 | -9.05 |
| VAT2 | CFFF | 0.151 | 0.142 | 6.85 |
| VAT3 | SSSS | 0.445 | 0.422 | 5.55 |
| VAT3 | CCCC | 0.632 | 0.945 | -33.19 |
| VAT3 | CFFF | 0.075 | 0.070 | 6.86 |
| QI | SSSS | 0.524 | 0.484 | 8.43 |
| QI | CCCC | 0.863 | 1.021 | -15.48 |
| QI | CFFF | 0.163 | 0.155 | 5.33 |
| AP | SSSS | 0.568 | 0.513 | 10.55 |
| AP | CCCC | 0.812 | 1.038 | -21.78 |
| AP | CFFF | 0.095 | 0.095 | 0.98 |

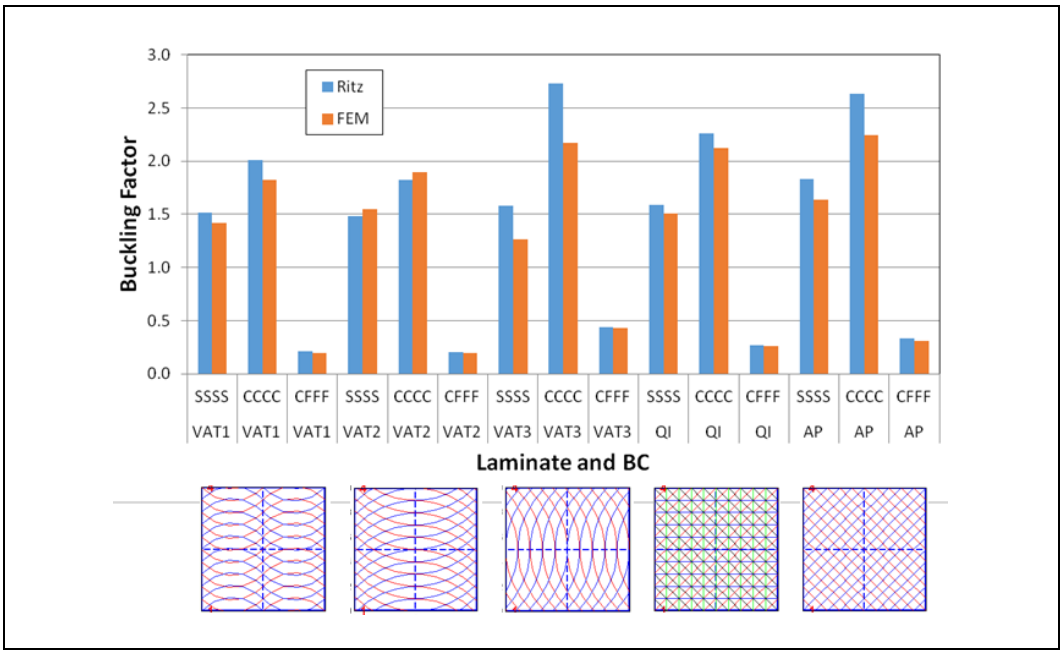


Figure 4-33. Buckling factor for $N_y$ loading of quadrilateral panel.

Table 4-11. $N_y$ buckling factors for quadrilateral panels.

| Laminate | BC | Buckling Factor | | % Error |
|---|---|---|---|---|
| | | Ritz | FEM | |
| VAT1 | SSSS | 1.516 | 1.419 | 6.85 |
| VAT1 | CCCC | 0.800 | 0.879 | -9.05 |
| VAT1 | CFFF | 0.213 | 0.195 | 9.23 |
| VAT2 | SSSS | 1.486 | 1.548 | -3.98 |
| VAT2 | CCCC | 1.826 | 3.105 | -41.18 |
| VAT2 | CFFF | 0.205 | 0.191 | 6.97 |
| VAT3 | SSSS | 1.577 | 1.263 | 24.79 |
| VAT3 | CCCC | 2.732 | 2.829 | -3.43 |
| VAT3 | CFFF | 0.441 | 0.427 | 3.19 |
| QI | SSSS | 1.588 | 1.511 | 5.11 |
| QI | CCCC | 2.260 | 2.762 | -18.16 |
| QI | CFFF | 0.584 | 0.730 | -19.96 |
| AP | SSSS | 1.836 | 1.637 | 12.11 |
| AP | CCCC | 2.635 | 3.293 | -19.98 |
| AP | CFFF | 0.331 | 0.310 | 6.90 |

## 4.7 Aero-structural Wing Analysis

Aeroelasticity is the study of interactions between aerodynamics and flexible aircraft structures. The interaction occurs as a result of the modification of aerodynamic loads due to structural deformation which, in turn is a function of the applied aerodynamic loads. The phenomenon can occur under both static and dynamic conditions and result in poor aircraft performance or even catastrophic failure. Interaction between the wing structural deflections and the aerodynamic loads determines the wing bending and twist at each flight condition. The wing's aeroelastic behavior governs the external loads and hence the internal loads and stresses, drag forces, control surface effectiveness, aircraft trim behavior and stability. It has been shown that concurrent optimization of structural and aerodynamic performance can improve overall aircraft performance in terms of reduced weight and drag, reduced gust loads, and improved flutter characteristics. This is accomplished by tailoring wing structural characteristics to provide desirable bending and torsion response for a range of flight conditions.

This section describes validation of the aeroelastic analysis methodology. The analysis consisted of the tow-steered wing in 4.4 fixed at the root subject to the flight condition described in Table 4-12. Aerodynamic loads computed by the flow solver were applied to the Ritz EPM to compute structural deflections which in turn were used to deform the aerodynamic surface. This process iterated until convergence was achieved.

Table 4-12 Flow conditions used for aeroelastic validation.

| *Mach* | *AOA* | $\rho$(slug/ft$^3$) | $S_{ref}$(ft$^2$) | $b_{ref}$(ft) | $c_{ref}$(ft) |
|---|---|---|---|---|---|
| 0.8 | 5.0 | 0.002377 | 72.0 | 16.0 | 4.5 |

The results of this study were used to compute the static aeroelastic shapes and to perform comparisons between the rigid and flexible loads distributions. Figure 4-34a shows the deflected shape resulting from the aerodynamic load where the wing exhibits bending and twist. Solution convergence is shown in Figure 4-34b for maximum tip deflection which is seen to increase by 65% due to aeroelastic effects. The associated rigid and flexible load distributions are shown in Figure 4-35a and Figure 4-35b.

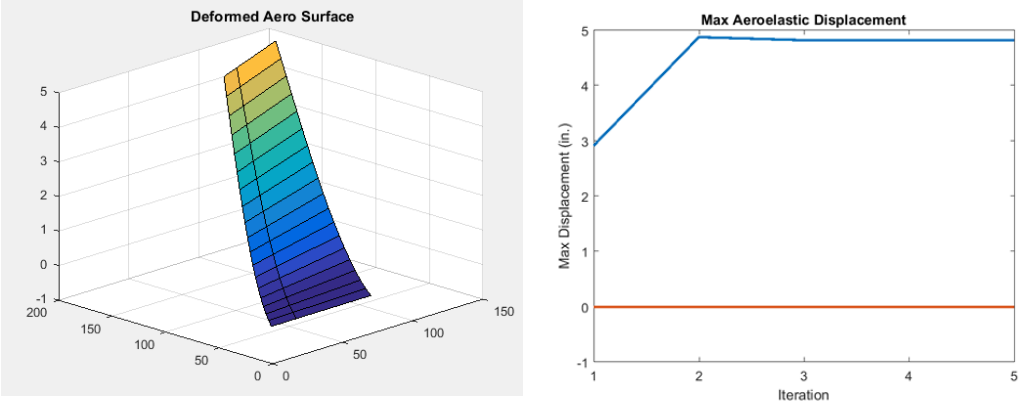


Figure 4-34 (a) Deformed wing surface, (b) Max displacement converence.

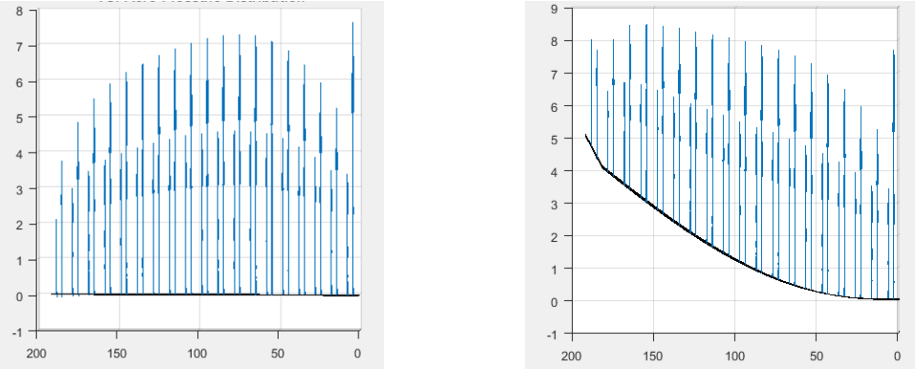

Figure 4-35 (a) Rigid aero load distribution, (b) Elastic aero load distribution.

The influence of aeroelastic effects on spanwise displacement and lift distribution is shown in Figure 4-36a and Figure 4-36b. Similarly, the spanwise lift coefficient and lift induced drag coefficient is given in Figure 4-37a and Figure 4-37b. These results confirmed that structural and aerodynamic response could be effectively coupled between the VSPAero flow model and the Ritz EPM structural model. This methodology will be used to develop rigid and flexible aerodynamic loads for the design optimization process.

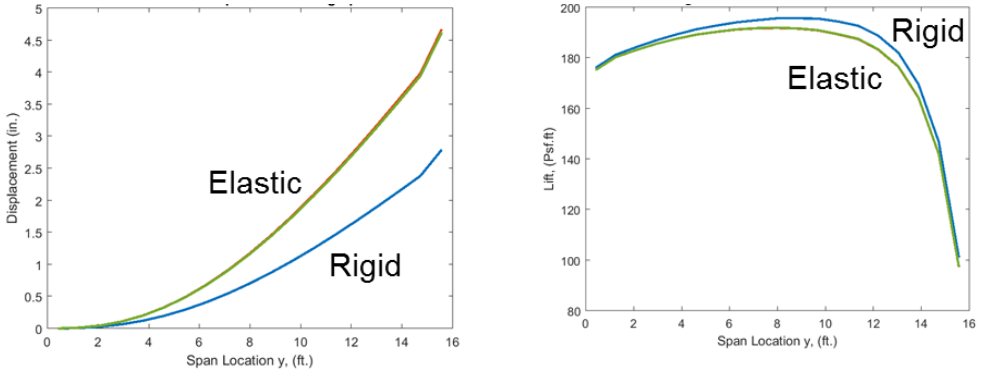


Figure 4-36 (a) Rigid/Elasitc displacement profile, (b) Rigid/Elastic lift distribution.

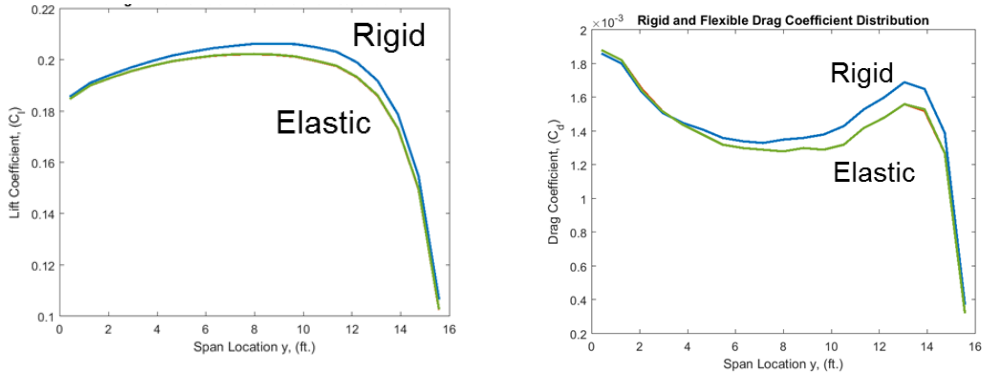


Figure 4-37. (a)Rigid/Elastic lift coefficient, (b) Rigid/Elastic lift due to drag coefficient.

# Chapter 5

## Design Optimization Model

This chapter describes the wing design optimization model and framework. A schematic description of the analysis codes and the framework configuration is provided. Design variables are defined to describe wing skin thickness distribution and fiber path. Design criteria are formulated as constraint functions and a minimum weight objection function is defined.

### 5.1 Objective Function and Design Variables

The swept wing shown in Figure 5-1 and described in section 4.1 is to be optimized for minimum weight by steering the fiber paths in the upper and lower wing skins independently subject to design constraints for strain, manufacturing and buckling. Each skin will be composed of 4 layers of orthotropic material all of which are offset to the same z-offset height of the wing OML surface. The skins are supported by eight ribs and eight spars having constant cross-section properties. The skin primary 0-degree fiber path shown in Figure 5-2 is defined by $\theta_U, \theta_L$, respectively, using equation (2.1), and is established by the four independent variables $\theta_{U_0}, \theta_{U_1}, \theta_{L_0}, \theta_{L_1}$ given by equation (5.1) in Table 5-1. The other layers are oriented at fixed angles of $\emptyset_k = (0, +45, -45, 90)$ degrees relative to the 0-degree path. Equation (2.2) is used to model the thickness of each layer as a second order Legendre polynomial with nine independent variables per layer or 36 variables per skin. This can be reduced to 27 variables by linking the +/-45 ply layers. Skin thicknesses are described by equations (5.2) in Table 5-1.

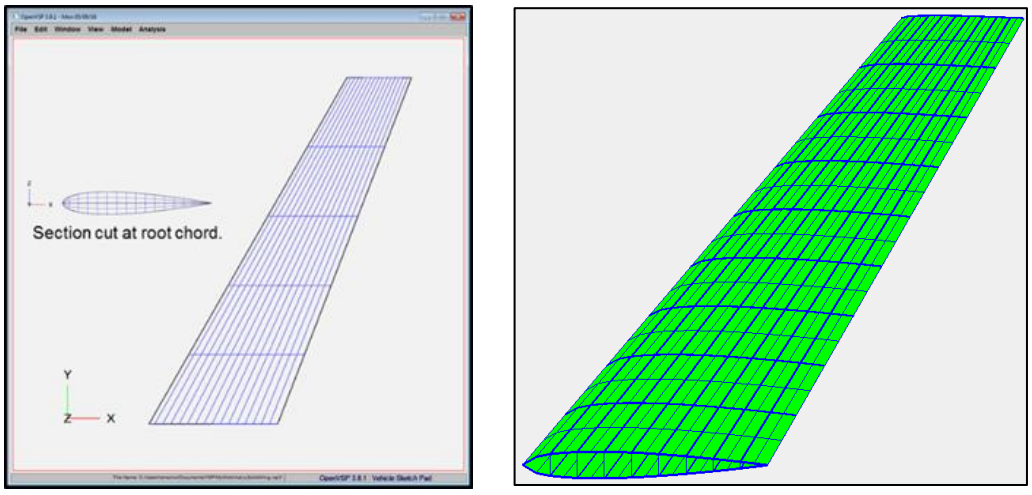


Figure 5-1. Swept wing surface geometry used for design optimization problem.

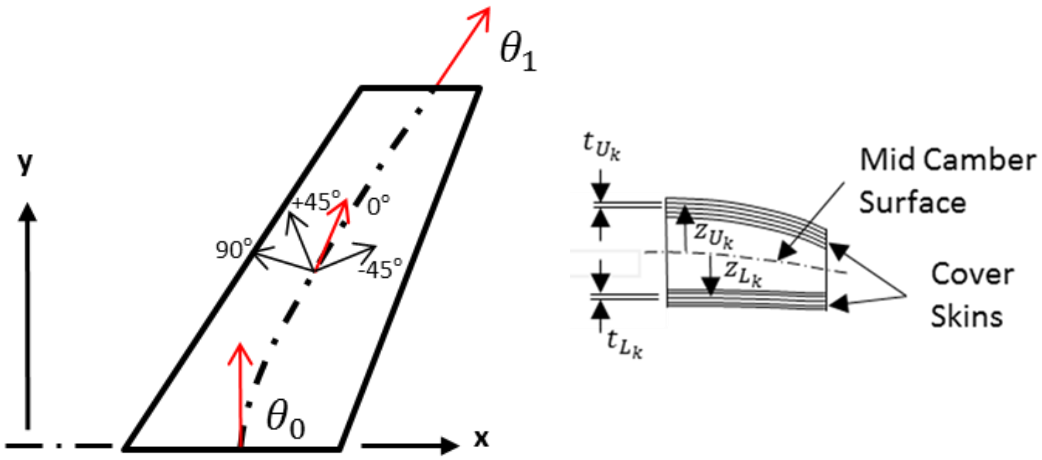


Figure 5-2. (a) Steering design variables and (b) Layer thickness design variables.

Table 5-1. Optimization design variables.

| Description | Expression | Independent Variables | |
|---|---|---|---|
| 0-Degree Reference Path | $\theta_U = (\theta_{U_1} - \theta_{U_0})\frac{y}{s} + \theta_{U_0}$<br>$\theta_L = (\theta_{L_1} - \theta_{L_0})\frac{y}{s} + \theta_{L_0}$ | $\theta_U(\theta_{U_0}, \theta_{U_1})$<br>$\theta_L(\theta_{L_0}, \theta_{L_1})$ | (5.1) |
| Layer Thickness | $t_{U_k}, t_{L_k}(\xi, \eta) = \sum_{i=0}^{I}\sum_{j=0}^{J} B_{ij}(\xi, \eta)t_{ij}$ | $t_{U_k}([t_{ij}]_{i=0:2;j=0:2})_{k=1\ldots4}$<br>$t_{L_k}([t_{ij}]_{i=0:2;j=0:2})_{k=1\ldots4}$ | (5.2) |

We define the formal optimization problem as

$$\min f(x) \tag{5.3}$$

subject to

$$g(x) = [g_\varepsilon, g_{\lambda_b}, g_{\lambda_f}, g_{lift}, g_{t_{min}}, g_{ply\%}] \leq 0 \tag{5.4}$$

$$h(x) = 0 \tag{5.5}$$

$$x_l \leq x \leq x_u \tag{5.6}$$

where

$$\{x\} = [\theta_U \;\; \theta_L \;\; t_{U_k} \;\; t_{L_k}]^T \tag{5.7}$$

## 5.2 Strain Constraints for Laminate Failure

Strain constraints are written in a normalized fashion as given by equation (5.8) to constrain wing material direction strains $\varepsilon_1, \varepsilon_1, \varepsilon_{12}$ to not exceed strain allowables $(\varepsilon_{1_{allow}}, \varepsilon_{2_{allow}}, \varepsilon_{12_{allow}})$. Strains are calculated at the mid-plane laminate surfaces for the upper and lower wing skins.

$$g_{strain}\ , (g_\varepsilon) = \left[\frac{\varepsilon_{x_{allow}}}{\varepsilon_x} - 1, \qquad \frac{\varepsilon_{y_{allow}}}{\varepsilon_y} - 1, \qquad \frac{\varepsilon_{xy_{allow}}}{\varepsilon_{xy}} - 1\right] \leq 0 \qquad (5.8)$$

## 5.3 Buckling Constraints for In Plane Skin Panel Loads

Buckling constraints are written in a normalized fashion as given by equation (5.9) to limit buckling from occurring in any skin panel.

$$g_{buckling}, (g_{\lambda_b}) = [\lambda_b - 1]_{panels} \leq 0 \qquad (5.9)$$

## 5.4 Flutter Constraint

Flutter is the most important of all the aeroelastic criteria. It is an unstable condition occurring when the structure vibrates and extracts energy from the air stream and often results in catastrophic failure. Classical flutter occurs when the aerodynamic forces of two modes of vibration (typically bending and torsion) cause the modes to couple. This behavior is illustrated in Figure 5-3 and occurs at a critical air speed known as the flutter speed. Below this speed oscillations are damped, whereas above it one of the modes becomes negatively damped to produce unstable oscillations. In general,

flutter can be difficult to predict and computationally expensive. Therefore, this study will implement a simple relationship given by equation (5.10) to separate the first bending from the first torsional modes by a factor of 8. While this is not representative of design practice, it serves the purpose of imposing a first order flutter constraint with a low computational cost.

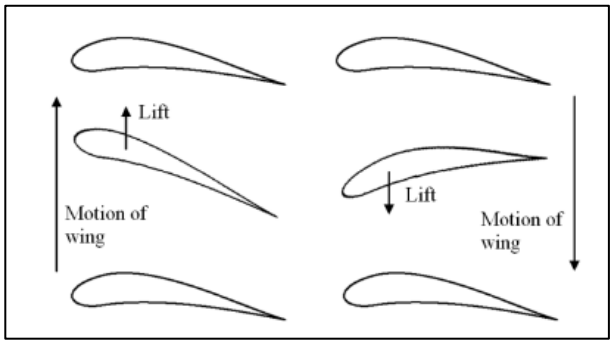

Figure 5-3. Illustration of flutter motions.

$$g_{flutter}, (g_f) = \frac{8 * \lambda_{1st\ torsion}}{\lambda_{1st\ bending}} - 1 \leq 0 \qquad (5.10)$$

## 5.5 Minimum Gage Constraints

Minimum skin gage thickness constraints are required to ensure that the total laminate thickness remains greater than a minimum acceptable gage thickness. For a laminated composite, this can be decomposed into a constraint for each of the primary skin layer thicknesses $[t_{\theta_1}, t_{\theta_2}, t_{\theta_3}, \ldots, t_{\theta_n}]$. For traditional laminates, this would include four layer thicknesses of $[t_0, t_{45}, t_{-45}, t_{90}]$. Additionally, because the skin layer thicknesses are defined by continuous polynomials, constraints must be formulated to ensure that each layer's thickness is everywhere greater than $t_{ply_{min}}$. This is formulated as

$$[A_m]\{x\} \leq \{b_m\} \tag{5.11}$$

Where

$$A_m = \begin{bmatrix} 0 & 0 & [t_{ij}]_{U_1} & 0 & 0 & 0 & 0 & 0 & 0 & 0 \\ 0 & 0 & 0 & [t_{ij}]_{U_2} & 0 & 0 & 0 & 0 & 0 & 0 \\ 0 & 0 & 0 & 0 & [t_{ij}]_{U_3} & 0 & 0 & 0 & 0 & 0 \\ 0 & 0 & 0 & 0 & 0 & [t_{ij}]_{U_4} & 0 & 0 & 0 & 0 \\ 0 & 0 & 0 & 0 & 0 & 0 & [t_{ij}]_{L_1} & 0 & 0 & 0 \\ 0 & 0 & 0 & 0 & 0 & 0 & 0 & [t_{ij}]_{L_2} & 0 & 0 \\ 0 & 0 & 0 & 0 & 0 & 0 & 0 & 0 & [t_{ij}]_{L_3} & 0 \\ 0 & 0 & 0 & 0 & 0 & 0 & 0 & 0 & 0 & [t_{ij}]_{L_4} \end{bmatrix} \tag{5.12}$$

and

$$\{b_m\} = t_{ply_{min}}[0 \quad 0 \quad 1 \quad 1 \quad 1 \quad 1 \quad 1 \quad 1 \quad 1 \quad 1]^T \tag{5.13}$$

## 5.6 Laminate Manufacturing Constraints

The ability to fabricate VAT laminates is constrained by the in-plane tow minimum steering radius of curvature required to avoid a tow buckling condition. If an individual tow of material is curved too much then it may buckle or develop defects as shown in Figure 5-4. Houmat [46] provided a closed form relation for calculating curvature of the linear fiber path model associated with a rectangular panel. Houmat's relation has been adapted in equations (5.14) and (5.15) to establish a tow steering curvature constraint.

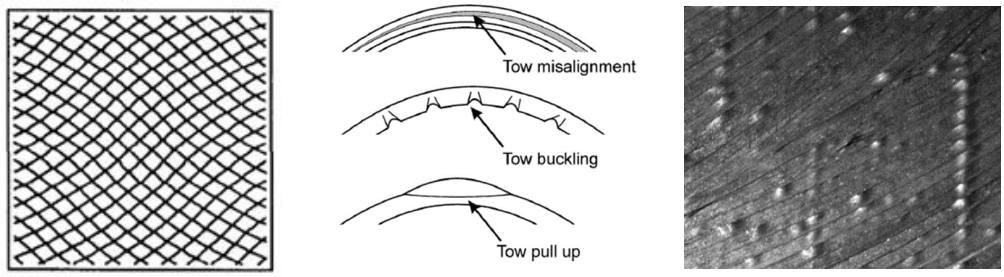


Figure 5-4. Curvilinear Fiber Paths and Defects Arising from Tow Steering [58], [59].

$$g_{path\_curvature} = \kappa_{path}/\kappa_{allow} - 1 \leq 0.0 \tag{5.14}$$

where

$$\kappa_{path} = \frac{2}{s}(\theta_1 - \theta_0)cos\left[\theta_0 + \frac{2}{s}(\theta_1 - \theta_0)y\right] \tag{5.15}$$

Additional constraints must be considered to control ply percentages, ply drop-off rate as depicted in Figure 5-5 and described by Costin and Wang [60]. Ply percentage constraints control the maximum and minimum thickness percentage of each orientation with respect to the total thickness. Ply drop-off rate is applied to constrain the maximum

rate of thickness change between adjacent zones and control the number of ply drops moving from a thick zone to a thin zone.

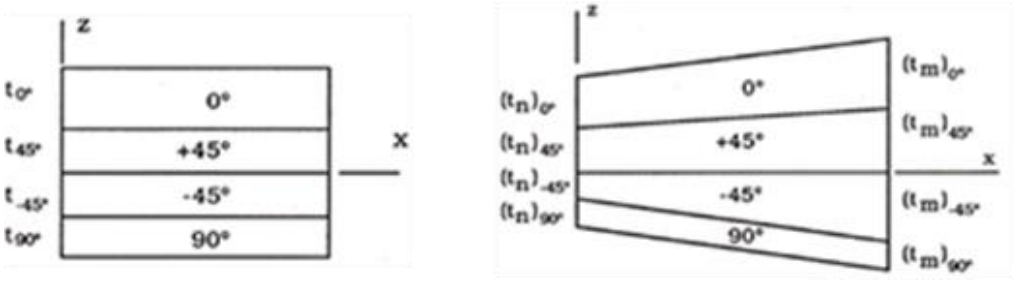


Figure 5-5. (a) Point ply percentages, (b) ply dropoff rate [60].

Constraint formulations were obtained from [60]. Allowable ply percentage constraints are given by (5.16) and ply drop ratio constraints are given by (5.17). These criteria will be applied at the Ritz integration points.

$$g_{ply\_percentage} = \frac{(t_k) - \frac{[P_u, -P_L]}{100}\sum_{k=1}^{4}(t_k)}{\sum_{k=1}^{4}(t_k)} \leq 0.0 \tag{5.16}$$

$$g_{ply\_drop} = \frac{1}{r_u}\frac{dt}{[dx, dy]} - 1.0 \leq 0.0 \tag{5.17}$$

# Chapter 6

## Wing Skin Optimization

This chapter describes a design study for a business jet wing skin application. Design conditions are developed to establish a wing with fixed substructure and variable thickness skins to support a MTOGW of 45,000 lbs. OpenVSP is used to develop wing geometry with modified airfoils to improve aerodynamic lift. The wing is extended in length from earlier studies in hopes of providing more aeroelastic flexibility. Rigid aerodynamic loads are developed using the VSPAero flow solver to achieve sufficient lift to meet a load factor of Nz=2.5.

The factored aerodynamic loads and wing geometry will serve as the basis for the structural optimization in combination with strain, flutter and maximum allowable ply percentage constraints. Implementation of buckling constraints were incomplete at the time of this study and were omitted. A constraint for minimum tow steering radius of curvature was omitted after recognizing the minimum possible steering radius for this wing would far exceed the minimum material allowable of 25 inches.

## 6.1 Design Conditions

The purpose of this optimization is to minimize wing skin weight for a business jet application. Specifications for the aircraft and wing are described in Table 6-1. The swept wing configuration from section 4.1 was modified to have a larger span with unsymmetric airfoils. The substructure layout utilizes 8 spars and 8 ribs located at equal chord and spar fractions, respectively. The wing must provide a lift to support 45,000 lb. GTOW with a normal load factor of 2.5g.

Table 6-1. Specifications for business jet wing design.

| | |
|---|---|
| Aircraft Performance Parameters | |
| Cruise Mach number | 0.8 |
| Cruise altitude | 40, 000 ft. |
| MTOGW | 45,000 lb. |
| Normal load factor, $N_z$ | 2.5g |
| Wing Geometry | |
| Semispan, b/2 | 20 ft. |
| Chord width [root, tip] | 6 ft., 2.25 ft. |
| Sweep | 30 degrees |
| t/c [root, tip] | 0.08, 0.06 |
| Camber [root, tip] | 0.2, 0.1 |
| Airfoil [root, tip] | NACA 2208, NACA 1206 |
| Structural Parameters | |
| Spar position [chord fraction] | 0.11/0.22/0.33/0.44/0.55/0.66/0.77/0.88 |
| Spar cap thickness, $t_{sc}$ | 0.2 in. |
| Spar cap width, $w_{sc}$ | 2.0 in. |
| Spar web thickness, $t_{sw}$ | 0.2 in. |
| Rib positions [semispan fraction] | 0.0/0.11/0.22/0.33/0.44/0.55/0.66/0.77/0.88/1.0 |
| Rib cap thickness, $t_{rc}$ | 0.2 in. |
| Rib cap width, $w_{rc}$ | 2.0 in. |
| Rib web thickness, $t_{rw}$ | 0.2 in. |

## 6.2 Design Constraints

A summary of the constraints used in the optimization process for the business jet wing skin sizing is given in Table 6-2. Structural strains were limited to maximum allowable material strains in tension, compression and shear, without any interaction between terms. Skin panel buckling constraints were not fully implemented at the time of this writing and were not active. Minimum gauge for each ply layer was limited to a minimum of 0.005 inches, unless the laminate was modeled as a single layer, in which case it was constrained to a value of 0.020 inches. Aerodynamic flutter was constrained the by the requirement that the first torsional mode was a factor of eight times greater than the first bending mode. The fiber path curvature constraint was also inactive.

Table 6-2. Design constraint summary.

| Constraint | Formulation | Notes |
|---|---|---|
| Strain | $g_{strain}\ , (g_{\varepsilon}) = \left[\frac{\varepsilon_x}{\varepsilon_{x_{allow}}} - 1, \frac{\varepsilon_y}{\varepsilon_{y_{allow}}} - 1,\ \frac{\varepsilon_{xy}}{\varepsilon_{xy_{allow}}} - 1\right] \leq 0$ | [0.0018, .0018, .0027] $\mu\varepsilon$ |
| Buckling | $g_{buckling},\ (g_{\lambda_b}) = [\lambda_b - 1]_{panels} \leq 0$ | Not active |
| Flutter | $g_{flutter}, (g_{\lambda_f}) = \frac{8 * \lambda_{1st\ torsion}}{\lambda_{1st\ bending}} - 1 \leq 0$ | |
| Minimum Gauge | $[A_m]\{x\} - \{b_m\} \leq 0$ | 0.005 in./layer |
| Fiber Path Curvature | $g_{path\_curvature} = \kappa_{path}/\kappa_{allow} - 1 \leq 0.0$ | $\kappa_{allow} = 0.04$,<br>Not active |
| Max/Min Ply % | $g_{ply\_percentage} = \frac{(t_k) - \frac{[P_u,\ -P_L]}{100}\sum_{k=1}^{4}(t_k)}{\sum_{k=1}^{4}(t_k)} \leq 0.0$ | $P_u$=0.6, $P_L$=0.1 |
| Allowable Ply Drop | $g_{ply\_drop} = \frac{1}{r_u}\frac{dt}{[dx, dy]} - 1.0 \leq 0.0$ | Not active |

This was based on knowing that $\kappa_{allow} = \frac{1}{25in}$ and noting the minimum possible sttering radius for a 20 foot wing semispan with a linear fiber path model, would be $\kappa_{path} = \frac{2\pi}{20ftx12in/ft.} = 0.0262$ which easily satisfies the fiber curvature constraint. The maximum and minimum allow ply percenages were $P_U$=0.6 and $P_L$=0.1. Ply drop constraints were inactive for the computed range of skin thickness gradients.

### 6.3 External Loads

External aerodynamic loads were developed using the VSPAero flow solver with a flight speed of Mach 0.8, a AOA of 2 degrees and assuming a rigid undeformed wing surface. A view of the distributed airloads for this condition is shown in Figure 6-1.

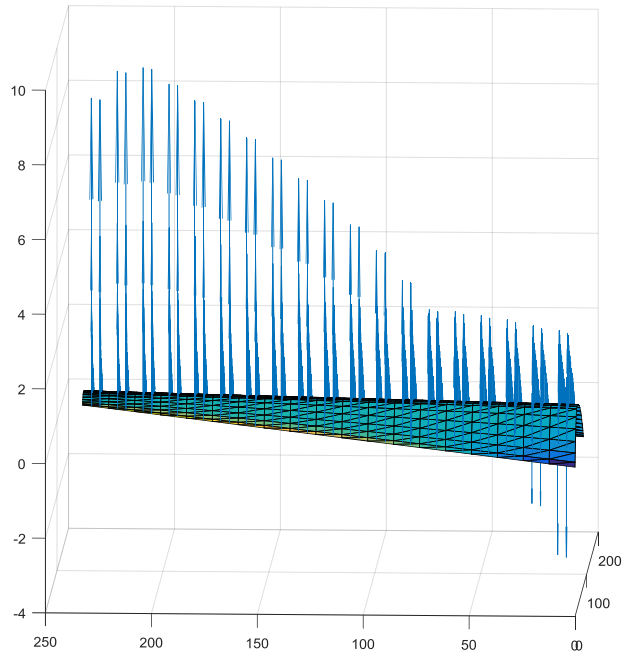


Figure 6-1. Aerodynamic load distribution for M0.8 and AOA=2.

## 6.4 Optimization Procedure

To compare performance of optimized straight-fiber laminates with tow-steered laminates, different laminate configurations were considered, based on orientation of the 0-degree reference fiber path. Unidirectional or "UD" laminates are traditional straight-fiber laminates with the 0-degree fiber path aligned such that ($\theta_U = 0$). UDrot laminates also utilize straight-fibers but the 0-degree reference path is rotated to a fixed, non-zero orientation ($\theta_U \neq 0$). VAT laminates are steered and allow the fiber path to vary linearly in the spanwise direction such that in general, $\theta_{U_0} \neq \theta_{U_1}$ . Laminate skin thickness is allowed to vary continuously using 2nd order Legendre polynomials (9 thickness coefficients per layer) evaluated at the same integration points as established by the Ritz EPM. Skin laminates are modeled using either a single layer with fixed ply percentages (9 thickness variables) or four independent layers (36 thickness variables) allowing for variable ply percentages across the wing planform. For the case of a single skin layer, the laminate ply percentages were chosen to be a 60/30/10 distribution to provide a structural bias along the 0-degree direction.

A matrix of design optimization cases were investigated as described by Table 6-3. Each case is a unique combination of laminate type (UD, UDrot, VAT), number of orthotropic wing skin ply layers ($N_{layer}$) and design constraints ($g_{strain}$, $g_{flutter}$, $g_{plypcnt}$). This approach was used to identify and separate the optimization behaviors based on constrains and number of active design variables. The upper and lower skin thicknesses and orientations were linked together [$(t_U = t_L)$ , $(\theta_U = \theta_L)$] and the optimizations were based only on the upper skin response.

Table 6-3. Design Optimization matrix for business jet wing.

| Case | Laminate | $N_{layer}$ | Ply %s | $g_{strain}$ | $g_{flutter}$ | $g_{plypcnt}$ |
|---|---|---|---|---|---|---|
| 1a | UD (9 variables) | 1 | 60/30/10 | x | | |
| 1b | "" | "" | "" | x | x | |
| 1c | "" | "" | "" | x | x | x |
| 2a | UDrot (10 variables) | 1 | 60/30/10 | x | | |
| 2b | "" | "" | "" | x | x | |
| 2c | "" | "" | "" | x | x | x |
| 3a | VAT (11 variables) | 1 | 60/30/10 | x | | |
| 3b | "" | "" | "" | x | x | |
| 3c | "" | "" | "" | x | x | x |
| 4a | UD (27 variables) | 4 | Variable | x | | |
| 4b | "" | "" | "" | x | x | |
| 4c | "" | "" | "" | x | x | x |
| 5a | UDrot (28 variables) | 4 | Variable | x | | |
| 5b | "" | "" | "" | x | x | |
| 5c | "" | "" | "" | x | x | x |
| 6a | VAT (29 variables) | 4 | Variable | x | | |
| 6b | "" | "" | "" | x | x | |
| 6c | "" | "" | "" | x | x | x |

## 6.5 Design Convergence

Design convergence was well behaved and numerical efficiency was good. Typically, a design optimization could be accomplished in 5 to 10 minutes, depending on the number of design variables and constraints. Computations were performed on a HP Z600 computer running 12 cores with a CPU speed of 2.66 GHz. Design histories for each optimization case are shown in Figure 6-2 through Figure 6-7. The histories are organized into design variable plots (Theta DVs = reference fiber direction), (Poly DVs = polynomial skin thickness coefficients), design objective function and constraint.

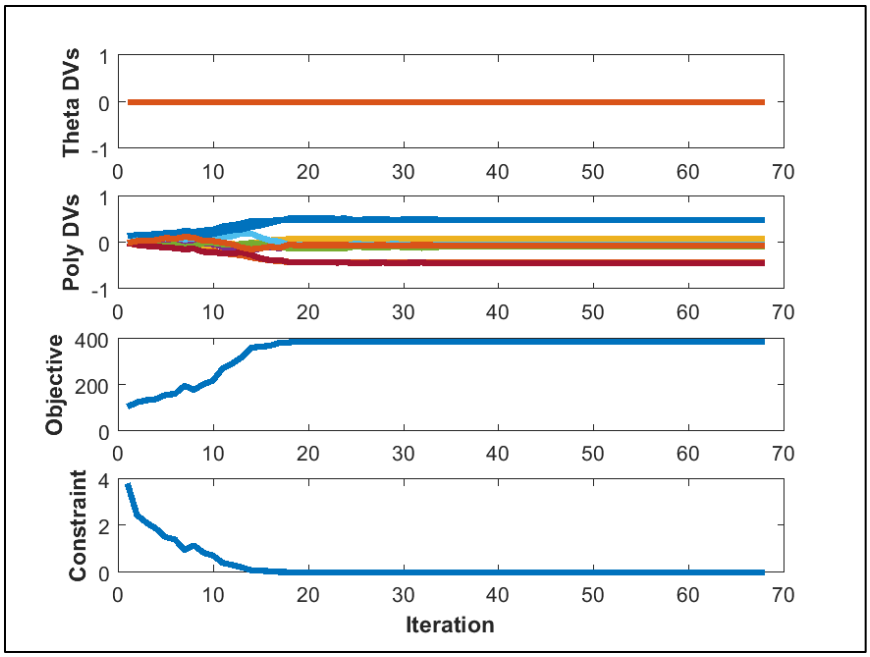


Figure 6-2. Design history for case1c UD (9 variables) laminate.

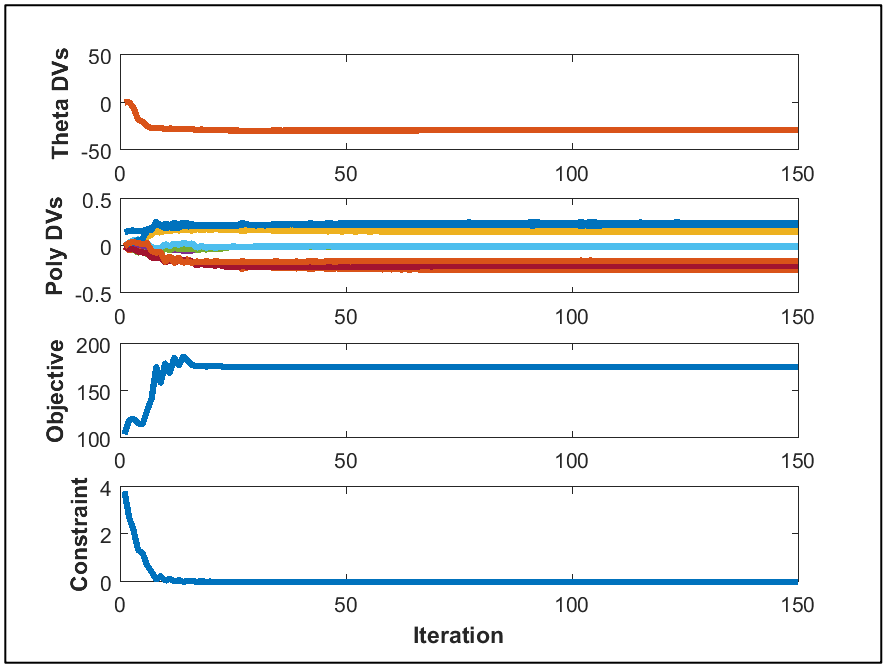


Figure 6-3. Design history for case2c UDrot (10 variables) laminate.

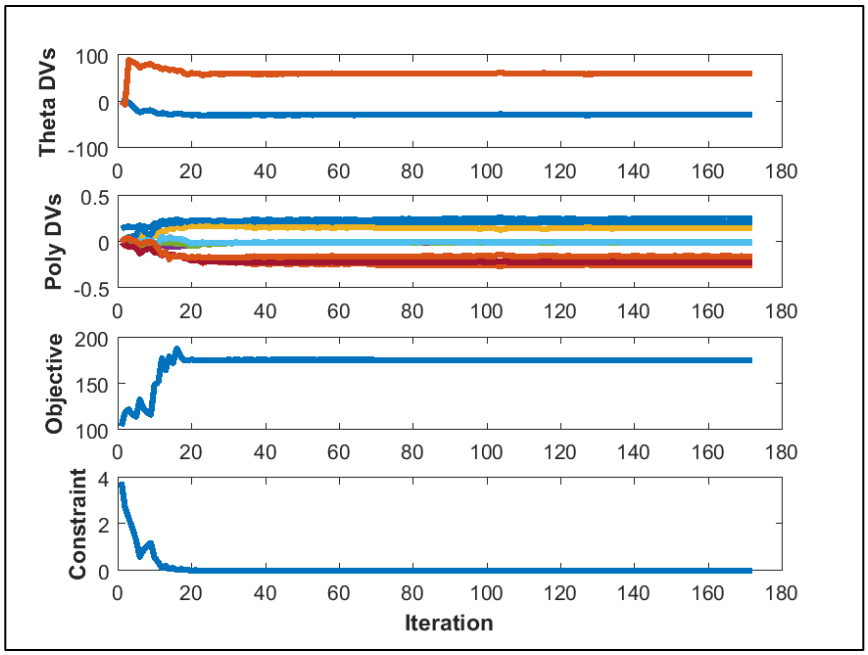


Figure 6-4. Design history for case3c VAT (11 variables) laminate.

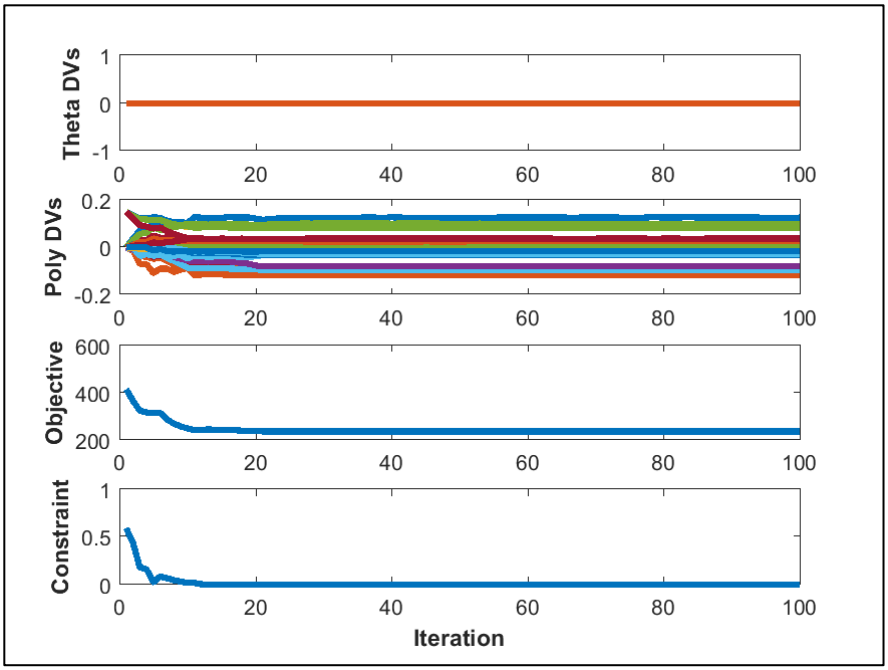


Figure 6-5. Design history for case4c UD (27 variables) laminate.

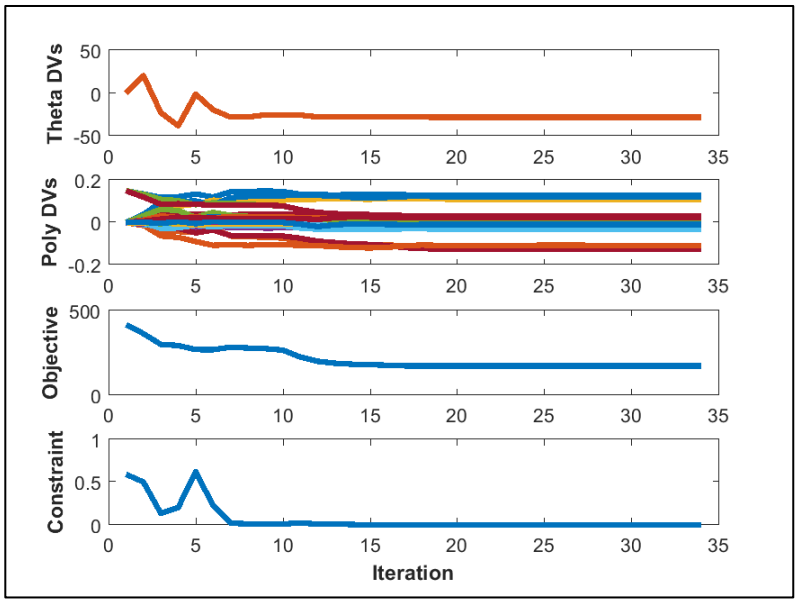


Figure 6-6. Design history for case5c UDrot (28 variables) laminate.

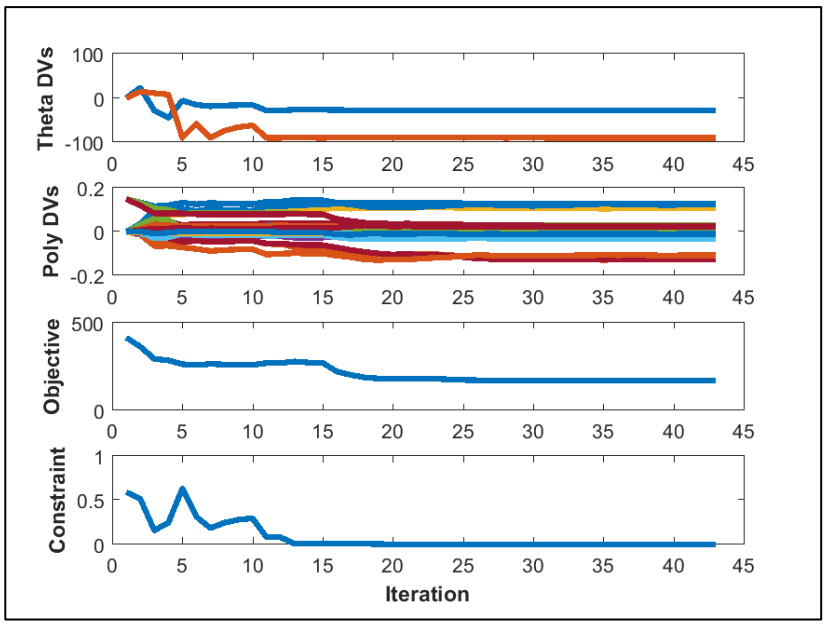


Figure 6-7. Design history for case6c UD (29 variables) laminate.

## 6.6 Optimization Results

Results from the optimization study are summarized in Table 6-4 and compared against one another in Figure 6-8. Several observations and conclusions can be made. First, it is noted that the Case 1 and Case 4 UD laminates [UD (9 variables), UD (27 variables)] produced the heaviest designs. This is an expected result since the 0-degree ply direction for these laminates is perpendicular to the wing root chord and skewed at an angle of 30-degrees from the wing primary structural axis. The Case 4 UD (27 variables) laminate offers the advantage of variable ply percentage laminate and shows a large weight reduction of ~43% over the Case 1 fixed ply percentage laminate. The additional independent layer thickness design variables allow a more optimized distribution of material. This can be seen more clearly in a comparison of the layer thickness distributions presented in Figure 6-9 and Figure 6-10. While the layer shapes are nearly identical, there is a substantial difference in thickness magnitude which accounts for the large weight difference.

Optimization of the fixed ply percentage laminates, Case 2 UDrot (10 variables) and Case 3 VAT (11 variables) yielded nearly identical weight results. They also showed no sensitivity to enforcement of multiple design constraints ($g_{strain}$, $g_{flutter}$, $g_{plypcnt}$) and yielded nearly identical skin weights (~ 175 lb). The UDrot (28 variables) and VAT (29 variables) laminates provided the lightest weight designs (~170 lb), but only a 3% improvement over the baseline UDrot and VAT laminates. A comparison of the layer thickness distributions are presented in Figure 6-11 and Figure 6-12.

Table 6-4. Optimized wing skin results.

| Case | Laminate | $N_{layer}$ | Ply %s | $g_{strain}$ | $g_{flutter}$ | $g_{plypcnt}$ |
|---|---|---|---|---|---|---|
| 1a | UD (9 variables) | 1 | 60/30/10 | x | | |
| 1b | "" | "" | "" | x | x | |
| 1c | "" | "" | "" | x | x | x |
| 2a | UDrot (10 variables) | 1 | 60/30/10 | x | | |
| 2b | "" | "" | "" | x | x | |
| 2c | "" | "" | "" | x | x | x |
| 3a | VAT (11 variables) | 1 | 60/30/10 | x | | |
| 3b | "" | "" | "" | x | x | |
| 3c | "" | "" | "" | x | x | x |
| 4a | UD (27 variables) | 4 | Variable | x | | |
| 4b | "" | "" | "" | x | x | |
| 4c | "" | "" | "" | x | x | x |
| 5a | UDrot (28 variables) | 4 | Variable | x | | |
| 5b | "" | "" | "" | x | x | |
| 5c | "" | "" | "" | x | x | x |
| 6a | VAT (29 variables) | 4 | Variable | x | | |
| 6b | "" | "" | "" | x | x | |
| 6c | "" | "" | "" | x | x | x |

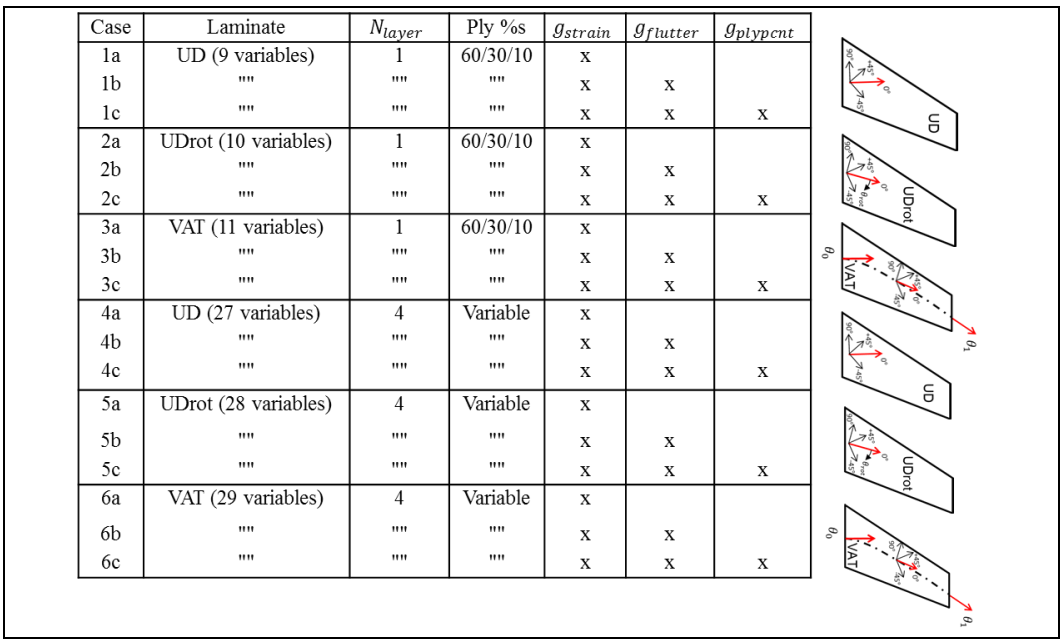


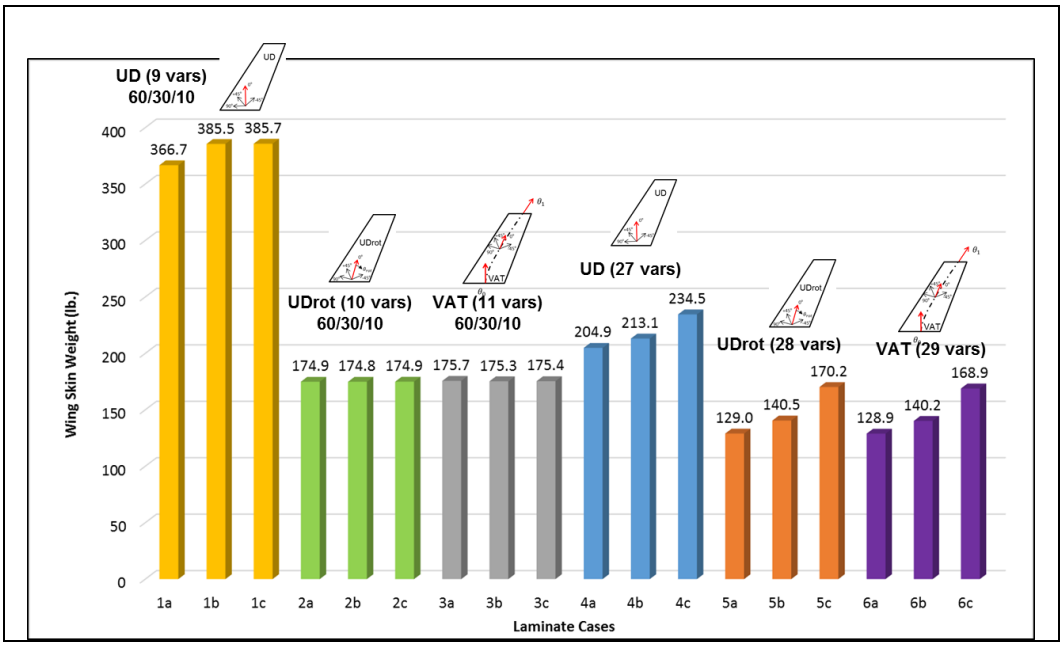


Figure 6-8. Comparison of optimized wing skin laminates.

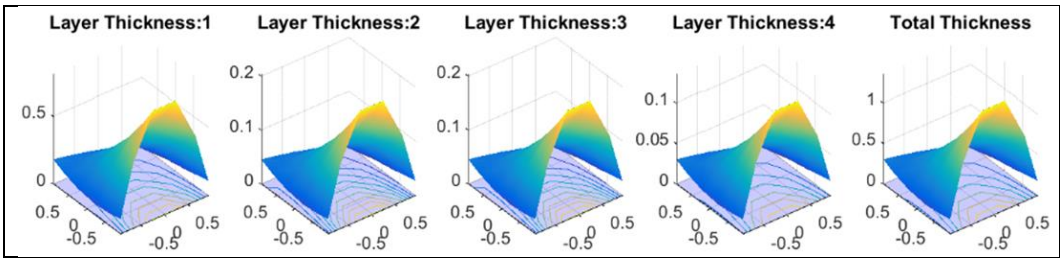


Figure 6-9. Thickness distribution for UD (9 variables) 60/30/10 laminate: case 1c.

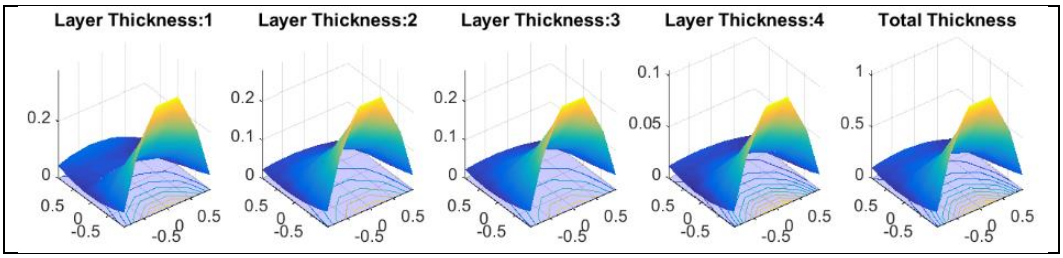


Figure 6-10. Thickness distribution for UD (27 variables) 60/30/10 laminate: case 4c.

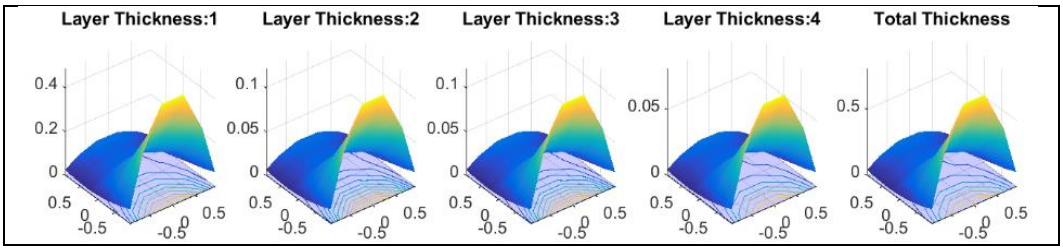


Figure 6-11. Thickness distribution for UDrot (10 variables) 60/30/10 laminate: case 2c.

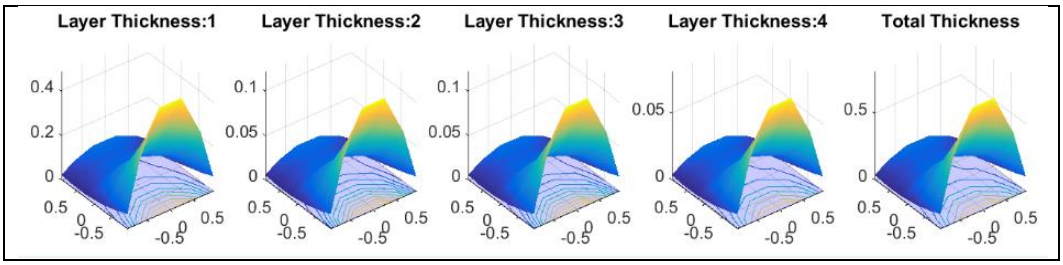


Figure 6-12. Thickness distribution for VAT (11 variables) 60/30/10 laminate: case 3c.

The UDrot (28 variables) and VAT (29 variables) laminates did however show a strong sensitivity to design constraints, where flutter imposed a weight increase of 7% over strength and ply percentage constraints imposed a weight penalty of 21% over flutter. Layer thickness and ply percentage disributions for these laminates is shown in Figure 6-13 through Figure 6-16. There are no recognizable differences between the layer thicknesses for these two laminates, but there are obvious differences in ply percentage distributions for the +/-45 plies. Fiber path for the lightest UDrot and VAT orientations are given in Figure 6-17 and Figure 6-18 were it can be seen there are significant differences.

However, the most notable observation was the fact that tow-steering offered no obvious improvements to the wing skin design. After further investigation, it was realized that the influence of the fixed substructure stiffness resulting from eight tightly spaced spars is a dominant factor in the spanwise direction. This conclusion was drawn by comparing the root and tip cross sections shown in Figure 6-19 and evaluating the planform sub-structural layout and skin thickness distribution shown in Figure 6-20. The ratio of EA_skin/EA_spars is 15.8 at the root and 2.1 at the tip. It was recognized that the spar spacing is essentially too close at the tip and not representative of typical aircraft geometry. Consequently, the wing sub-structure stiffness rapidly diminishes the benefits of steering in the spanwise direction.

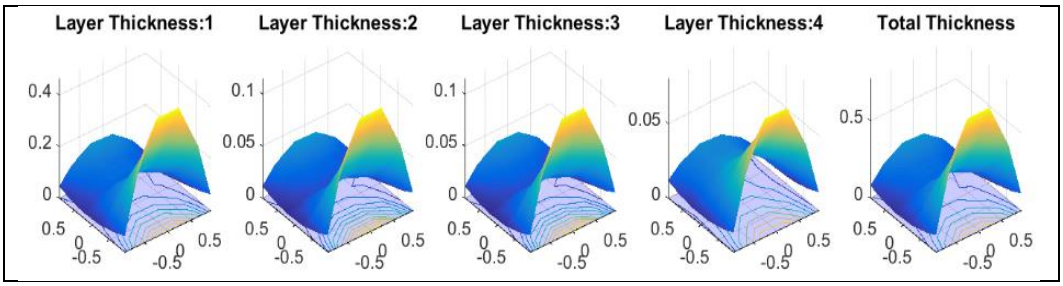


Figure 6-13. Thickness distribution for UDrot (37 variables) laminate: case 5c.

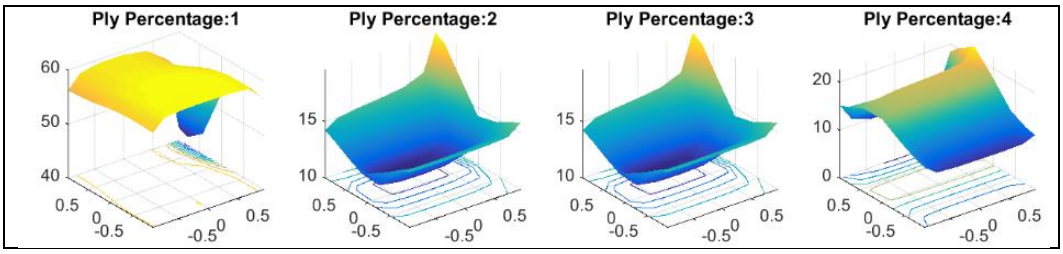


Figure 6-14. Ply percentage distribution for UDrot (28 variables) laminate: case 5c.

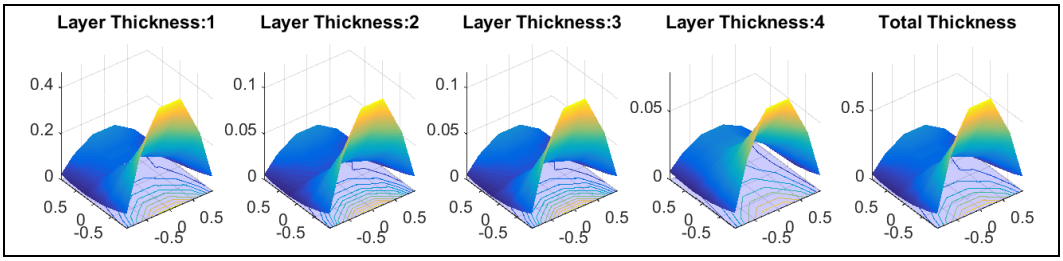


Figure 6-15. Thickness distribution for optimized VAT (29 variables) laminate: case 6c.

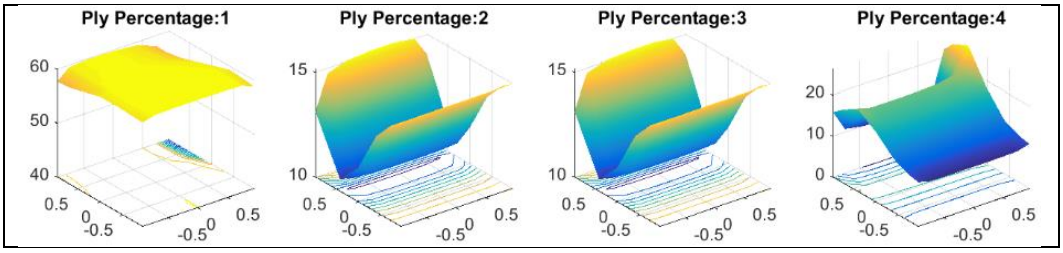


Figure 6-16. Ply percentage distribution for VAT (29 variables) laminate: case 6c.

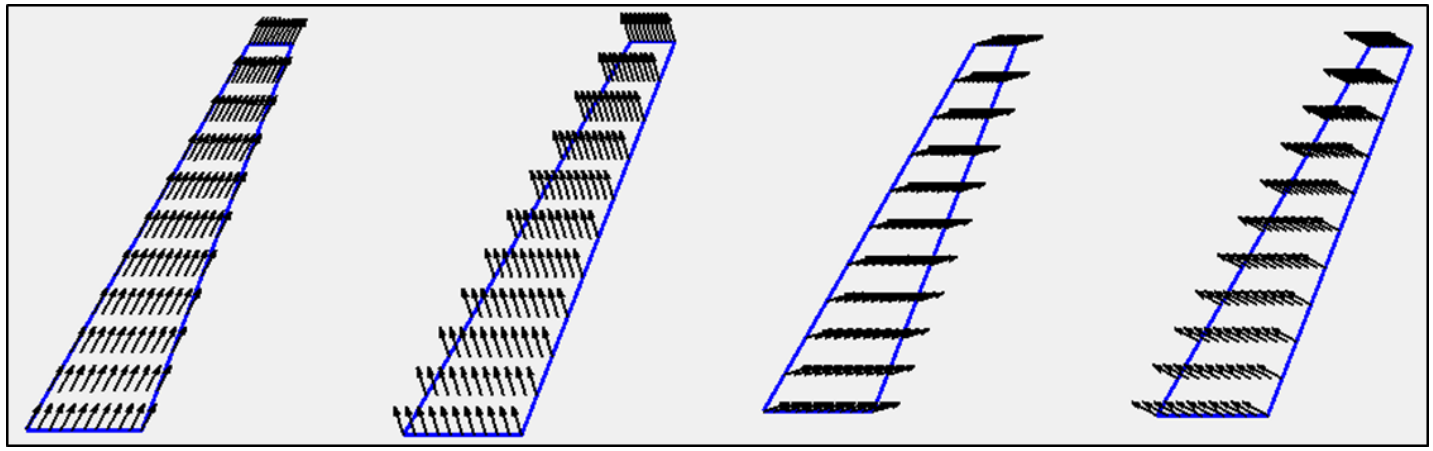

Figure 6-17. Fiber paths for optimized UDrot laminate.

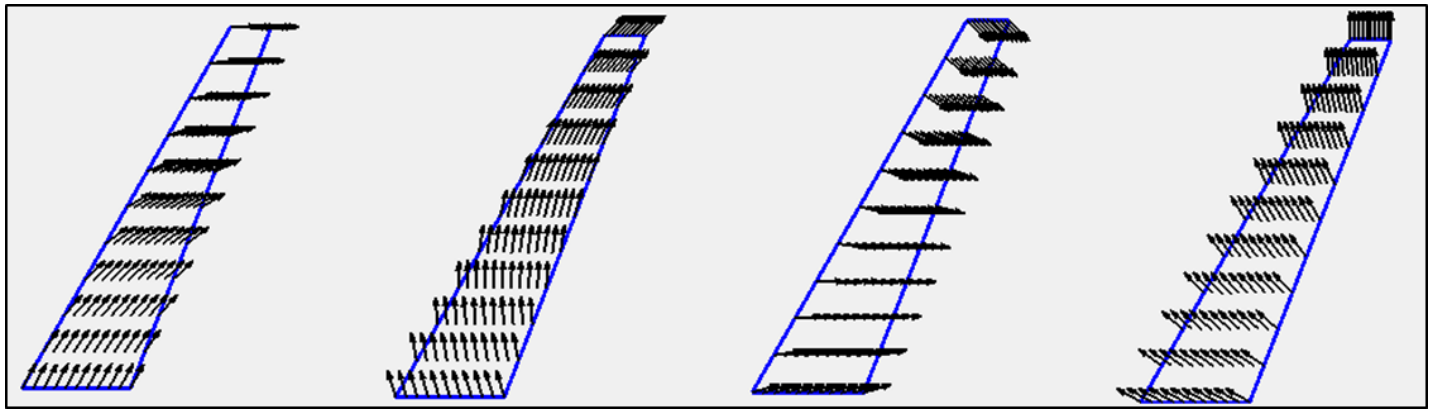

Figure 6-18. Fiber paths for optimized VAT laminate.

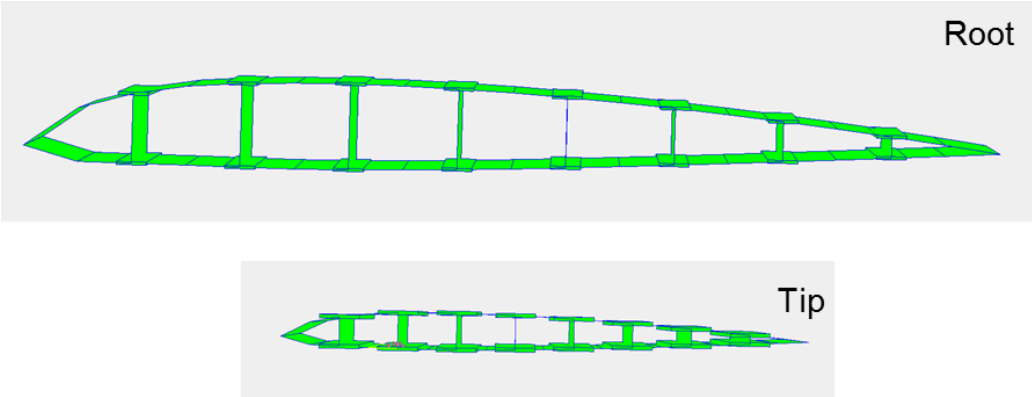


Figure 6-19. Wing cross-sections at root and tip locations.

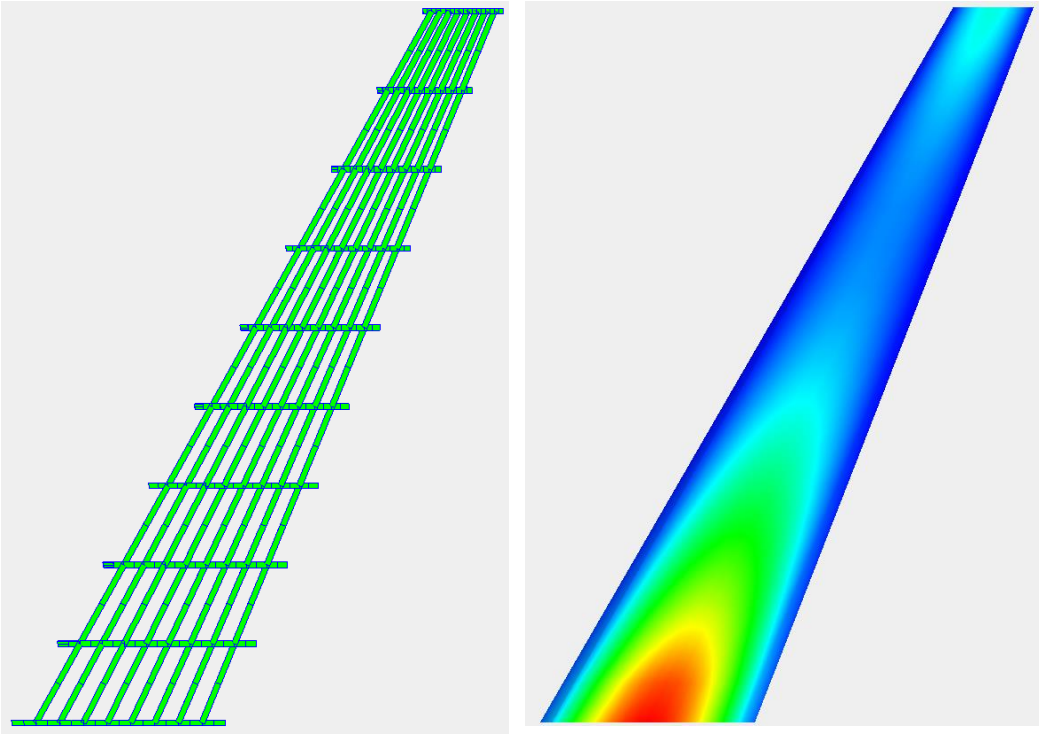

Figure 6-20. Planview of (a) substructure geometry and (b) optimized skin thickness.

## 6.7 Static Response of Optimized Designs

A comparison of Ritz EPM and FEA deflections and strains is shown in Figure 6-21 and Figure 6-22 for the UDrot (28 variables) optimized laminate. Similar results are presented in Figure 6-23 and Figure 6-24 for the VAT (29 variables) laminate.

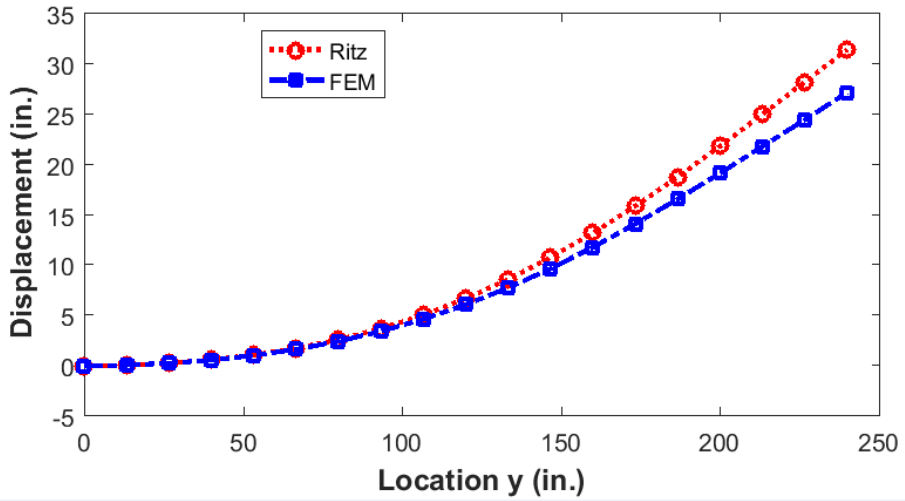


Figure 6-21. Ritz EPM and FEA spanwise deflection for UDrot (28 variables) laminate.

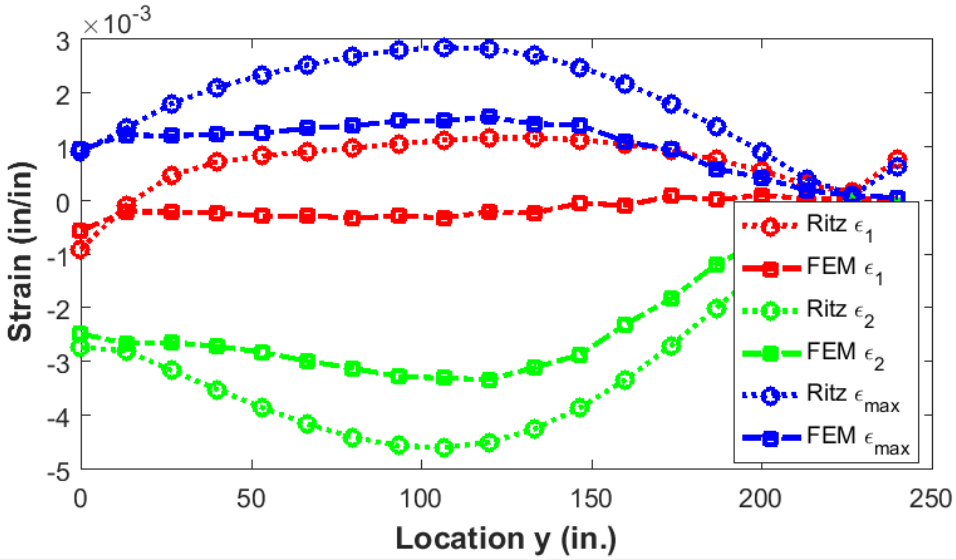


Figure 6-22. Ritz EPM and FEA spanwise strains for UDrot (28 variables) laminate.

Ritz and FEA deflections agree reasonably well for both laminate designs. The UDrot laminate does show a larger disagreement in strain results than the VAT design. However, this served to confirm there were no unusual features for either design.

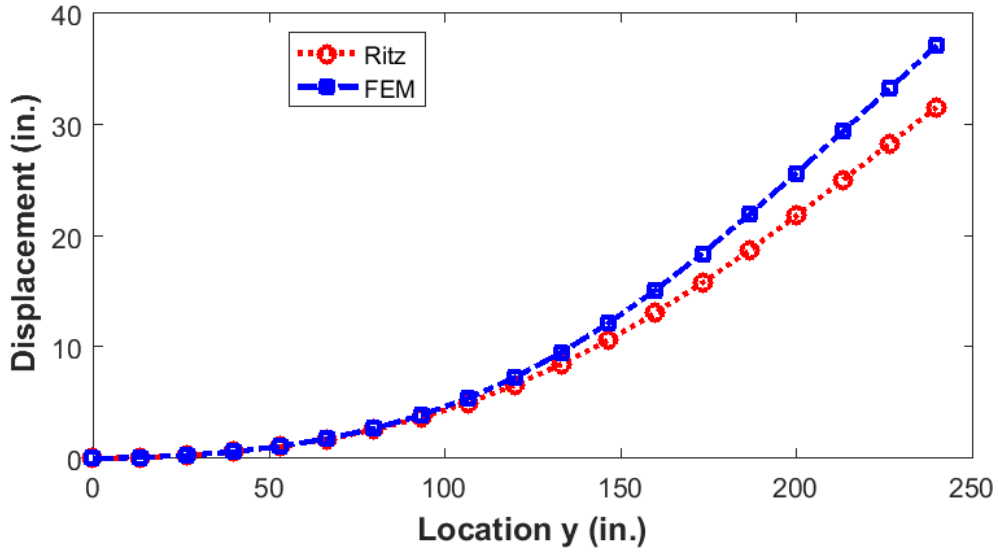


Figure 6-23. Ritz EPM and FEA spanwise deflection for VAT (29 variables) laminate.

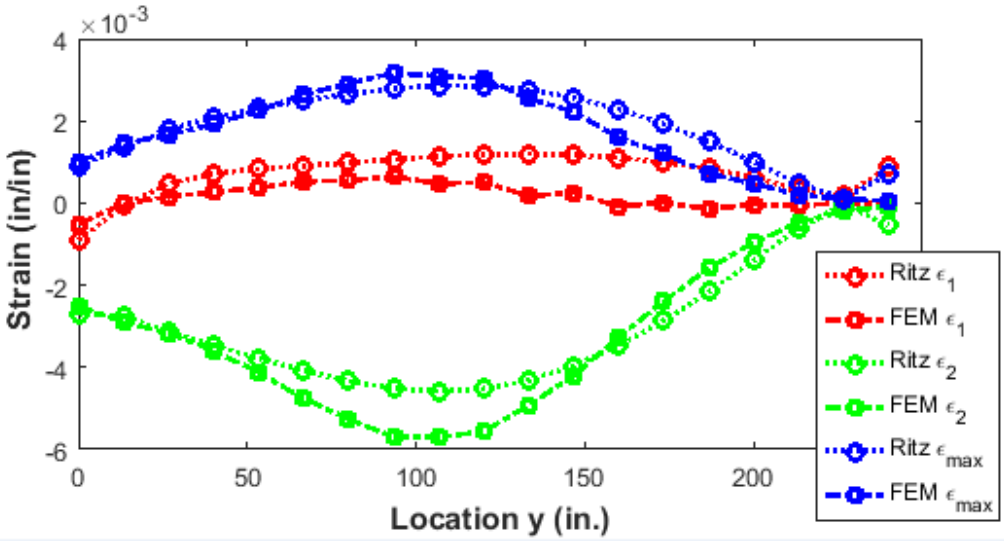


Figure 6-24. Ritz EPM and FEA spanwise strains for VAT (29 variables) laminate.

# Chapter 7

# Conclusions and Future Work

## 7.1 Conclusions

The purpose of this dissertation was to develop and demonstrate an efficient proof-of-concept methodology for tow-steered design of aircraft composite wing structures. Consideration was given to the disiplines of parametric design, aerodynamics, structures and manufacturing. The disciplines were coupled together in a framework that included the software components: OpenVSP, VSPAero, Ritz EPM and MATLAB. The capability enables design optimization for wing structures composed of traditional unidirection composites and tow steered composites. The parametric geometry and coupled analysis models provides the flexibility to model a wide range of wing designs rapidly at low computational cost. Validation studies were peformed to confirm behavior, performance and interaction between the components. The capability was exercised to optimize a business jet wing using tow-steering design criteria.

The Ritz EPM methodology was based on the work of Kapania and Liu [15] and extended to model composite laminates with curvilinear fiber paths. Validation studies using FEA confirmed that EPM is suitable for conceptual and preliminary design involving static and modal analyses. Computational efficiency of the EPM was best at polynomial orders $N_p \leq 6$ and optimization studies performed well using $N_p = 5$. The Ritz EPM was interfaced with the OpenVSP parametric design software using the DegenGeom Matlab export format to enable rapid geometry access. This integration enabled a straight forward coupling between design geometry, aerodynamics and structural response. Aerodynamic surface pressures were coupled to the EPM structural

model to compute deflections created by a flight condition. These displacements were used to deform the aerodynamic surface geometry which in turn were used to compute new loads. The process iterated until structural deflections were converged, and was typically accomplished within 5 iterations.

A business jet wing model was optimized to minimize wing skin weight using straight-fiber and tow-steered laminates. Design variables included linear fiber path orientation coefficients and thickness coefficients to model second order Legendre polynomial representations of composite layers. Wing skins were optimized by sizing the thickness coefficients and orienting the fiber paths of UD, UDrot and VAT laminates. The number of design variables ranged from 9 to 38 and constraints included strain, flutter and allowable ply percentages. Optimizations were performed using individual constraints such as strain, and also using combined constraints in the hope of gaining a better understanding of design drivers and the benefits for fiber steered skin design. Design convergence was well behaved and computational performance was good, enabling optimizations to complete in approximately fifteen minutes.

Three primary wing skin laminate types were investigated, including UD, UDrot and VAT. The UDrot (28 variables) and VAT (29 variables) provided the lightest weight designs with nearly identical weight results and there was no apparent advantage to tow steering. The lightest laminates showed a strong sensitivity to design constraints, where flutter imposed a weight increase of 7% over strength and ply percentage constraints imposed a weight penalty of 21% over flutter. However, these lightest designs were only 3% lighter than the UDrot (9 variables) and VAT (11 variables) laminates. An assessment of the wing substructure stiffness relative to the skin stiffness

(EA_skin/EA_spars) at the root and tip sections revealed ratios of 15.8 at the root and 2.1 at the tip. The wing sub-structure stiffness appears to rapidly diminish the benefits of steering in the spanwise direction. The limited scope of the design optimization study did not allow sufficient opportunity to exploit the advantages of tow steering. The following section outlines recommendations for future work.

## 7.2 Recommendations for Future Work

The developed framework can easily be extended to support a larger number of design variables and constraints that address sizing of wing substructure and modeling of higher order fiber path descriptions. The Ritz EPM can also be extended to model more complex wing assemblies that include multiple quadrilateral wing segments and control surfaces with associated aerodynamic flow coupling. Implementation of buckling constraints should be completed as it is typically an active design criteria for wings. A robust flutter solution implementation would be a natural extension of the current formulation to more accurately represent dynamic flutter effects and dependency on frequency, damping and airspeed. There is opportunity to include an aerodynamic trim and maneuver solution using the flow solver for development of air vehicle load conditions. Introduction of thermal loads and time dependency would be a straight forward extension and support for geometric nonlinear solutions would be advantageous.

The automated FEM generator can be more fully leveraged by supporting output of NASTRAN SOLUTION 200 design optimization models to enable higher fidelity optimizations and analyses. Attention should also be focused on the combined use of Ritz EPM with FEM to rapidly establish initial designs and map those solutions to a FEM

for increased refinement. More efficient programming languages such as Fortran, C++ and Python could be pursued to further improve performance.

Future validations should include sets of aircraft design points that consider trimmed aircraft aerodynamics, including several critical points in a flight envelope and consideration of various mass states and maneuver load conditions. Additional design studies should be performed to evaluate combination of traditional and fiber steered laminates to address the effects of design features such as laminate build-ups for mechanical fasteners and load introduction points.

## References


[1] W. G. Roeseler, B. Sarh and M. U. Kismarton, "Composite structures: The first 100 years. ," in *Proceedings of the 16th International Conference on Composite Materials*, Kyoto, Japan, 2007, July, .

[2] L. A. McCullers and R. W. Lynch, "Dynamic characteristics of advanced filamentary composite structures, vol II, aeroelastic synthesis procedure development, AFFDL-TR-111," Air Force Flight Dynamics Laboratry, Tech. Rep. AFFDL-TR-73-111, 1973.

[3] J. R. R. A. Martins, J. J. Alonso and J. J. Reuther, "A Coupled-Adjoint Sensitivity Analysis Method for High-Fidelity Aero-Structural Design," *Optimization and Engineering*, vol. 6, *(1)*, pp. 33-62, 2005. Available: https://doi.org/10.1023/B:OPTE.0000048536.47956.62. DOI: 10.1023/B:OPTE.0000048536.47956.62.

[4] J. E. Williams *et al*, *The USAF Stability and Control Digital Datcom: Users Manual*. 1976Available: http://books.google.de/books?id=mzi7YgEACAAJ.

[5] L. Miranda R., R. Elliot D. and W. Baker M., *A Generalized Vortex Lattice Method for Subsonic and Supersonic Flow Applications.* 1978.

[6] H. W. M. Hoeijmakers, "Panel methods for aerodynamic analysis and design, In: AGARD-FDP/VKI special course on engineering methods in aerodynamic analysis and design of aircraft," ADVISORY GROUP FOR AEROSPACE RESEARCH & DEVELOPMENT, 7 RUE ANCELLE 92200 NEUILLY SUR SEINE FRANCE, Tech. Rep. AGARD Report R-783, NLR TP 91404 L, 1992.

[7] G. L. Giles, "Design oriented structural analysis," National Aeronautics and Space Administration, Tech. Rep. NASA Technical Memorandum 109124, 1994.

[8] W. A. Rogers and R. W. Lynch, "Aeroelastic tailoring of advanced composite structures for military aircraft: Volume 3 - modification and user's guide for procedure TSO," AFFDL-76-100." Tech. Rep. AFFDL-76-100, 1978.

[9] G. GILES, "Equivalent plate analysis of aircraft wing box structures with general planform geometry," in Anonymous 1986, Available: http://dx.doi.org/10.2514/6.1986-940. DOI: doi:10.2514/6.1986-940.

[10] G. GILES, "Further generalization of an equivalent plate representation for aircraft structural analysis," in Anonymous 1987, Available: http://dx.doi.org/10.2514/6.1987-721. DOI: doi:10.2514/6.1987-721.

[11] G. Giles, "Equivalent plate modeling for conceptual design of aircraft wing structures," in Anonymous 1995, Available: http://dx.doi.org/10.2514/6.1995-3945. DOI: doi:10.2514/6.1995-3945.

[12] S. Stone *et al*, "Evaluation of equivalent laminated plate solution (ELAPS) in HSCT sizing," in Anonymous 2000, Available: http://dx.doi.org/10.2514/6.2000-1452. DOI: doi:10.2514/6.2000-1452.

[13] S. Tizzi, "Numerical Procedure for the Dynamic Analysis of Three-Dimensional Aeronautical Structures," *J. Aircr.*, vol. 34, *(1)*, pp. 120-130, 1997. Available: https://doi.org/10.2514/2.2145. DOI: 10.2514/2.2145.

[14] E. Livne, "Equivalent plate structural modeling for wing shape optimization including transverse shear," *Aiaa J.*, vol. 32, *(6)*, pp. 1278-1288, 1994. Available: https://doi.org/10.2514/3.12130. DOI: 10.2514/3.12130.

[15] R. K. Kapania and Y. Liu, "Static and Vibration Analyses of General Wing Structures Using Equivalent-Plate Models," *Aiaa J.*, vol. 38, *(7)*, pp. 1269-1277, 2000. Available: https://doi.org/10.2514/2.1098. DOI: 10.2514/2.1098.

[16] M. C. Henson and B. P. Wang, "Vibration and buckling of quadrilateral variable stiffness laminated composite plates," in *57th AIAA/ASCE/AHS/ASC Structures, Structural Dynamics, and Materials Conference*Anonymous 2016, Available: https://doi.org/10.2514/6.2016-1975. DOI: doi:10.2514/6.2016-1975.

[17] M. C. Henson and B. Wang, "Efficient methods for design and analysis of tow steered wing structures," in *58th AIAA/ASCE/AHS/ASC Structures, Structural Dynamics, and Materials Conference*Anonymous 2017, Available: https://doi.org/10.2514/6.2017-1304. DOI: doi:10.2514/6.2017-1304.

[18] B. WANG *et al*, "Laminate ply stacking sequence and ply termination selection," in Anonymous 1989, Available: http://dx.doi.org/10.2514/6.1989-1295. DOI: doi:10.2514/6.1989-1295.

[19] J. E. Lamar. Cranked arrow wing (F-16XL-1) flight flow physics with CFD predictions at subsonic and transonic speeds. 2003.

[20] J. Bohlmann and M. H. Love, "Aeroelastic tailoring and integrated wing design ," in 1989, .

[21] M. M. Vaniglia, "Fibre delivery assembly and fibre placement machine," 1988. Available: http://www.google.com/patents/EP0225563A3?cl=en.

[22] M. M. Vaniglia, "Fiber placement machine," 1990. Available: http://www.google.com/patents/US4907754.

[23] D. O. Evans, M. M. Vaniglia and P. C. Hopkins, "Fiber placement process study," in *34th International SAMPE Symposium*, May 8-11 1989, pp. 1822-1833.

[24] J. R. Barth, "Fabrication of complex composite structures using advanced fiber placement technology," in *35th International SAMPE Symposium*, April 2-5 1990, .

[25] M. L. Enders and P. C. Hopkins, "Developments in the fiber placement process," in *36th International SAMPE Symposium*, April 15-18, 1991, pp. 778-790.

[26] D. O. Evans, "Fiber placement," in . *ASM Handbook*, S. L. Donaldson and D. B. Miracle, Eds. ASM International, 2001, pp. 477-479.

[27] D. Evans, "Automated processing of aerospace composite components," in *NCMS, CTMA, Symposium2005*, 2005, .

[28] R. D. Hale *et al*, " Integrated Design and Analysis Tools for Reduced Weight, Affordable Fiber Steered Composites," 2003.

[29] V. M. Benson and J. Arnold, "Automated fiber placement of advanced materials (preprint)," AIR FORCE RESEARCH LAB WRIGHT-PATTERSON AFB OH MATERIALS AND MANUFACTURING DIRECTORATE, Tech. Rep. AFRL-ML-WP-TP-2006-424, 2006.

[30] A. W. Blom *et al*, "A Theoretical Model to Study the Influence of Tow-drop Areas on the Stiffness and Strength of Variable-stiffness Laminates," *J. Composite Mater.*, vol. 43, *(5)*, pp. 403-425, 2009. DOI: 10.1177/0021998308097675.

[31] M. HYER and R. CHARETTE, "The use of curvilinear fiber format in composite structure design," in Anonymous 1989, Available: http://dx.doi.org/10.2514/6.1989-1404. DOI: doi:10.2514/6.1989-1404.

[32] M. W. Hyer and H. H. Lee, "The use of curvilinear fiber format to improve buckling resistance of composite plates with central circular holes," *Composite Structures*, vol. 18, *(3)*, pp. 239-261, 1991. Available: http://www.sciencedirect.com/science/article/pii/026382239190035W. DOI: http://dx.doi.org/10.1016/0263-8223(91)90035-W.

[33] Z. GURDAL and R. OLMEDO, "In-plane response of laminates with spatially varying fiber orientations - Variable stiffness concept," *Aiaa J.*, vol. 31, *(4)*, pp. 751-758, 1993. Available: http://dx.doi.org/10.2514/3.11613. DOI: 10.2514/3.11613.

[34] B. F. Tatting and Z. Gurdal, "Design and manufacture of elastically tailored tow placed plates," Tech. Rep. NASA/CR—2002–211919, 2002.

[35] Z. Gurdal, B. Tatting and K. Wu, "Tow-placement technology and fabrication issues for laminated composite structures," in Anonymous 2005, Available: http://dx.doi.org/10.2514/6.2005-2017. DOI: doi:10.2514/6.2005-2017.

[36] Z. Gürdal, B. F. Tatting and C. K. Wu, "Variable stiffness composite panels: Effects of stiffness variation on the in-plane and buckling response," *Composites Part A: Applied Science and Manufacturing*, vol. 39, *(5)*, pp. 911-922, 2008. . DOI: http://dx.doi.org.ezproxy.uta.edu/10.1016/j.compositesa.2007.11.015.

[37] S. Nagendra *et al*, "Optimization of tow fiber paths for composite design," in Anonymous 1995, Available: http://dx.doi.org/10.2514/6.1995-1275. DOI: doi:10.2514/6.1995-1275.

[38] M. W. Tosh, "An Experimental and Numerical Investigation of Fibre Steering in Composite Structures." , ProQuest, UMI Dissertations Publishing, 2000.

[39] L. Parnas, S. Oral and Ã Ceyhan, "Optimum design of composite structures with curved fiber courses," *Composites Sci. Technol.*, vol. 63, *(7)*, pp. 1071-1082, 2003. Available: http://www.sciencedirect.com/science/article/pii/S0266353802003123. DOI: http://dx.doi.org/10.1016/S0266-3538(02)00312-3.

[40] K. Schueler, J. R. Miller and R. Hale, "Approximate Geometric Methods in Application to the Modeling of Fiber Placed Composite Structures," *Journal of COmputing and Information Science in Engineering*, vol. 4, pp. 251-256, 2004.

[41] A. W. Blom *et al*, "Fiber path definitions for elastically tailored conical shells," *Composites Part B*, vol. 40, *(1)*, pp. 77-84, 2009.

[42] Z. Wu *et al*, "Buckling analysis and optimisation of variable angle tow composite plates," *Thin-Walled Structures*, vol. 60, pp. 163-172, 2012. . DOI: http://dx.doi.org/10.1016/j.tws.2012.07.008.

[43] A. Alhajahmad, M. M. Abdalla and Z. Gurdal, "Optimal Design of Tow-Placed Fuselage Panels for Maximum Strength with Buckling Considerations," *J. Aircr.*, vol. 47, *(3)*, pp. 775-782, 2010. Available: http://arc.aiaa.org/doi/abs/10.2514/1.40357. DOI: 10.2514/1.40357.

[44] S. Honda, Y. Narita and K. Sasaki, "Discrete Optimization for Vibration Design of Composite Plates by Using Lamination Parameters," *Advanced Composite Materials*, vol. 18, *(4)*, pp. 297-297, 2009.

[45] H. Akhavan and P. Ribeiro, "Natural modes of vibration of variable stiffness composite laminates with curvilinear fibers," *Composite Structures*, vol. 93, *(11)*, pp. 3040, 2011.

[46] A. Houmat, "Nonlinear free vibration of laminated composite rectangular plates with curvilinear fibers," *Composite Structures*, vol. 106, pp. 211-224, 2013. . DOI: http://dx.doi.org/10.1016/j.compstruct.2013.05.058.

[47] H. Haddadpour and Z. Zamani, "Curvilinear fiber optimization tools for aeroelastic design of composite wings," *J. Fluids Struct.*, vol. 33, pp. 180, 2012.

[48] O. Stodieck *et al*, "Improved aeroelastic tailoring using tow-steered composites," *Composite Structures*, vol. 106, pp. 703, 2013.

[49] O. Stodieck *et al*, "Optimization of Tow-Steered Composite Wing Laminates for Aeroelastic Tailoring," *Aiaa J.*, vol. 53, *(8)*, pp. 2203-2215, 2015. Available: https://doi.org/10.2514/1.J053599. DOI: 10.2514/1.J053599.

[50] C. V. Jutte *et al*, "Aeroelastic tailoring of the NASA common research model via novel material and structural configurations," in Anonymous 2014, Available: http://dx.doi.org/10.2514/6.2014-0598. DOI: doi:10.2514/6.2014-0598.

[51] T. R. Brooks, G. Kennedy and J. Martins, "High-fidelity aerostructural optimization of a high aspect ratio tow-steered wing," in *57th AIAA/ASCE/AHS/ASC Structures, Structural Dynamics, and Materials Conference*Anonymous 2016, Available: https://doi.org/10.2514/6.2016-1179. DOI: doi:10.2514/6.2016-1179.

[52] O. Stodieck *et al*, "Aeroelastic Tailoring of a Representative Wing Box Using Tow-Steered Composites," *Aiaa J.*, vol. 55, *(4)*, pp. 1425-1439, 2017. Available: https://doi.org/10.2514/1.J055364. DOI: 10.2514/1.J055364.

[53] (). *OpenVSP*.

[54] J. R. Gloudemans, P. C. Davis and P. A. Gelhausen, "A rapid geometry modeler for conceptual aircraft," in *34th Aerospace Sciences Meeting and Exhibit, Reno, NV Jan*, 1996, .

[55] A. S. Hahn, "Vehicle sketch pad: A parametric geometry modeler for conceptual aircraft design," in *48th AIAA Aerospace Sciences Meeting and Exhibit*, 2010, .

[56] J. B. Belben and R. A. McDonald, "Enabling rapid conceptual design using geometry-based multi-fidelity models in VSP," in *51st AIAA Aerospace Sciences Meeting Including the New Horizons Forum and Aerospace Exposition, Grapevine (Dallas/Ft. Worth Region), Texas, USA*, 2013, .

[57] D. J. Kinney and R. A. McDonald. (August 22, 2016). *VSPAERO Theory* [OpenVSP Workshop 2016]. Available: http://www.openvsp.org/wiki/doku.php?id=workshop2016.

[58] D. H. -. A. Lukaszewicz, C. Ward and K. D. Potter, "The engineering aspects of automated prepreg layup: History, present and future," *Composites Part B: Engineering*, vol. 43, *(3)*, pp. 997-1009, 2012. Available: http://www.sciencedirect.com/science/article/pii/S1359836811005452. DOI: http://dx.doi.org/10.1016/j.compositesb.2011.12.003.

[59] D. R. Tenney *et al*, "NASA composite materials development: Lessons learned and future challenges," in *NATO Research and Technology Agency (RTA) AVT 164 - Support of Composite Systems*, 2009, .

[60] D. P. Costin and B. P. Wang, "Optimum design of a composite structure with manufacturing constraints," *Thin-Walled Structures*, vol. 17, *(3)*, pp. 185-202, 1993.

## Biographical Information

Michael C. Henson was born June 4, 1961 in Jacksonville, Florida. He attended Texas A&M University and completed his BSc and MSc in Civil Engineering in 1983 and 1985, respectively. He participated in the Advanced Composites Program while at Texas A&M. His thesis research was focused on the effects of moisture absorption in composite materals. Michael started full time employment at General Dynamics in September, 1985 and was assigned to the Advanced Methods Group.

Michael started work towards a PhD degree in June of 1987 while employed full time at General Dynamics. His course work was completed by 1995 but he decided to take a leave from schoolwork to focus on his family. He began dissertation research in 2013 and completed in December 2017. During that time, Michael has remained a full time employee of General Dynamics which later became Lockheed Martin Aeronautics.

Michael has participated in a wide range of projects and assignments while at Lockheed Martin. This work has included structural analysis tool and methods development, hypersonic nozzle structure development, airframe ground testing, composites certification, multidisciplinary optimization and general research and development. He remains employed at Lockheed Martin and is currently serving as a project manager.

## Appendix A.

## AIAA_2017-1304: Efficient Methods for Design and Analysis of Tow Steered Wing Structures

AIAA SciTech Forum
9 - 13 January 2017, Grapevine, Texas
58th AIAA/ASCE/AHS/ASC Structures, Structural Dynamics, and Materials Conference





# Efficient Methods for Design and Analysis of Tow Steered Wing Structures

Mike C. Henson[1]
Bo P. Wang[2]
*Mechanical and Aerospace Engineering, University of Texas at Arlington, Arlington, TX, 76019*



## Abstract

**This paper presents an efficient method for design and analysis of wing structures having general planform geometry constructed with tow steered laminated composite skins. Multiple quadrilateral segments are used with first-order shear deformation theory to model wing structural response as an equivalent plate assembly using the Ritz solution technique. The procedure is implemented efficiently into a framework that enables direct calibration with a finite element model and is suitable for application to conceptual and early preliminary design. The methods are used to calculate static response and vibration modes and frequencies.**

## Nomenclature

| | | |
|---|---|---|
| *CD* | = | Conceptual Design |
| *EPM* | = | Equivalent Plate Method |
| *FSDT* | = | First Order Shear Deformation Theory |
| *AFP* | = | Automated Fiber Placement |
| *FEM* | = | Finite Element Method |
| *FEA* | = | Finite Element Analysis |
| $x_i$,$y_i$ | = | plate corner point coordinates |
| $N_i$ | = | bilinear interpolation function |
| $\xi$, $\eta$ | = | natural coordinate system |
| $J$ | = | Jacobian matrix |
| $A_{ij}$,$B_{ij}$,$D_{ij}$ | = | laminated plate stiffnesses |
| $\theta(x,y)$ | = | fiber orientation |
| $Q_{ij}^k$ | = | lamina stiffness matrix for kth layer |
| $u$, $v$, $w$ | = | displacement components |
| $\emptyset_x$, $\emptyset_y$ | = | rotation components |
| $\varepsilon_x$, $\varepsilon_y$, $\varepsilon_{xy}$ | = | strain components |
| $\{q\}$ | = | displacement vector |
| $B_i(x)$ | = | polynomial displacement function |
| $B_{IJ}, B_{KL}, B_{MN}$ | = | coefficients of displacement functions |
| $N_p$ | = | order of polynomial basis function |
| $M_g$, $N_g$ | = | gauss integration points |

## I. Introduction

Rapid exploration of aircraft conceptual design (CD) space has increased the need for efficient modeling and analysis techniques. Many alternative configurations are evaluated in multidisciplinary design trades to determine the values of system-level variables such as gross weight and external geometry shape parameters which are used to measure overall vehicle performance. Airframe modeling and evaluation in the early stages of design is often avoided because structural layout and sizing activities cannot keep pace with configuration development. Structural performance criteria is typically reduced to empirical weight estimates and has limited relevance at this stage of design. However, airframe design trades conducted during CD can provide valuable insight to structural layout feasibility, performance and early risk assessment. A first-order estimate of material required for strength and aerolelastic constraints can serve three critical needs (Ref. 1). First, data is provided in terms of the weight required to meet the combined structural constraints for various planforms and assists in the elimination of infeasible aerodynamic surfaces. Second, a critical evaluation can be made of material efficiency in aeroelastically constrained designs, and last, a preliminary risk assessment of structural concepts and materials can be performed. The aerospace industry is keenly aware of these needs as it is estimated that 90% of the cost of a product is committed during the first 10% of the design cycle.

[1]PhD Candidate, Mechanical and Aerospace Engineering, Box 19023, Arlington, TX 76019, AIAA Senior Member.
[2] Professor, Mechanical and Aerospace Engineering, Box 19023, Arlington, TX 76019.

The Finite Element Method (FEM) is widely used for structural analysis because of its versatility and reliability. However, setup and solution time using traditional FEM techniques are generally not well suited to support rapidly evolving configuration development. Further, parametric design space exploration does not always facilitate creation of high fidelity vehicle geometry which further hampers the use of FEM in CD. Alternatively, equivalent continuum models can be used to simulate the behavior of complex structural assemblies for the purpose of developing conceptual airframe design solutions. Moreover, the combined use of continuum models with FEM can be used to rapidly calibrate and quantify uncertainties that may be present in lower order solutions. There have been several tools developed to study aircraft wing structures as continuum equivalent plate models (Ref. 2-10). For example, the TSO (Aeroelastic Tailoring and Structural Optimization) code enjoyed widespread use but was limited to trapezoidal planforms (Ref. 1 and Ref. 2). Giles developed ELAPS (Equivalent Laminated Plate Solution) while at NASA to analyze more complex wing planforms with internal structure (Ref. 3-7). Tizzi developed a method similar to Giles and later provided support for modeling internal rib and spar structure (Ref. 8). Livne (Ref. 9) formulated a wing equivalent plate model employing the use of First Order Shear Deformation Theory (FSDT). Kapania and Liu (Ref. 10) presented the use of FSDT with well-behaved Legendre basis functions to model trapezoidal wing structures. The work in Kapania and Liu was applied by Henson and Wang (Ref. 11) to model behavior of laminated quadrilateral plates with variable fiber path geometry.

This paper presents a methodology for modeling wing structures with tow-steered laminates. The directional properties of composite materials provide distinct advantages over metals in their ability to tailor aircraft structure for improved static and dynamic response at a reduced weight. Traditionally, straight-fiber laminated composites have been tailored by sizing the laminate into regions of constant thickness to meet the loads local to that region or zone. Tow steered laminates on the other hand possess stiffness properties that are a function of position and can be produced by continuously varying the ply fiber orientation. Automated Fiber Placement (AFP) has gained recognition for its ability to fabricate complex aircraft structure with improved precision and reduced cost. Current industry practice is to implement AFP much like the conventional hand layup process where fiber orientations are restricted to be constant within a given ply. However, fibers can also be steered in-plane and placed into a curvilinear orientation as shown in Figure 1 to achieve variable stiffness.

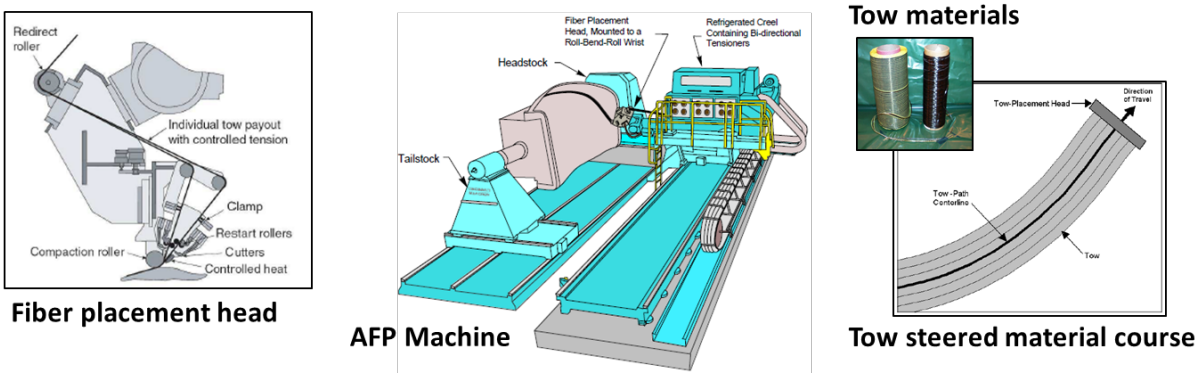


*Figure 1. Automated fiber placement equipment and tow steering.*

Researchers have demonstrated that fiber steering expands the design space by offering increased tailoring flexibility with improved performance and weight savings. Early work performed by Hyer et al. (Ref. 12 and 13) documented improvements that can be achieved in buckling performance with the use of curvilinear fiber orientations. Gurdal and Olmedo (Ref. 14) studied the in-plane elastic response of variable stiffness panels. Gurdal et al. (Ref. 15-17) investigated the design, analysis and manufacturing of VAT laminates for maximum buckling performance. Extensive research has also been devoted to modeling and analysis of curvilinear fiber paths (Ref. 18-26). Vibration studies have been conducted in (Ref. 27-29) to demonstrate fundamental frequency improvements and aeroelastic optimization with curvilinear fibers has been conducted in Ref. 30 and 31.

This paper presents a methodology for modeling wing structures fabricated with tow-steered composite skins as an equivalent plate assembly using FSDT and the Ritz solution method. High order Legendre polynomials are used to model the displacement fields and provisions are made to include the effects of rib-spar substructure. This work also attempts to address shortcomings identified in Ref. 7 which have been commonly associated with equivalent plate modeling techniques. The equivalent plate representation is also used to automatically generate a 3-D shell representation of the wing structure for calibration and design verification.

## II. Wing Geometry and Construction

### A. Wing Geometry Interface

Definition of three-dimensional wing geometry is facilitated through the use of the OpenVSP (Ref. 32) parametric aircraft geometry tool. OpenVSP allows creation of a 3D aircraft using common engineering parameters. It was originally developed at NASA by Gloudemans and others (Ref. 33 and 34) and has been released under the NASA Open Source Agreement. A model can be generated automatically using its built-in scripting language and processed into formats suitable for engineering analysis. A particularly useful format is the degenerative geometry file developed by Belben (Ref. 35) used to extract the geometry as a faceted 3D surface, or a flattened 2D idealization, or a stick model as shown in Figure 2. The 3D surface representation is used to extract wing geometry that is a function of the z-coordinate, such as section cuts at spar and rib centerlines and skin surface integration points. The 2D equivalent plate definition is derived from the OpenVSP degenerative plate idealization which defines the planform reference plane for construction of wing segments, and centerlines for ribs and spars.

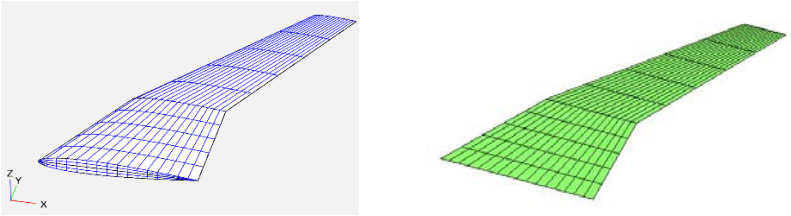

*Figure 2. Example OpenVSP wing exported to degenerative surface and plate idealizations.*

### B. Wing Planform

The wing planform is modeled as an assembly of quadrilateral segments as illustrated in Figure 3. Each segment is defined by four grid points and transformed from the physical ($x$-$y$) domain to a local ($\xi$-$\eta$) computational domain as described by Figure 4. The transformation is accomplished using Eq. *(1)*. $N_i$ are the bilinear Lagrangian interpolation functions used in the finite element method and $x_i$ and $y_i$ are the physical coordinates of the plate corner points. This makes it possible to select displacement basis functions with orthogonal properties and reduces the ($\xi$-$\eta$) computational domain to $[-1 \leq \xi, \eta \leq 1]$. It also facilitates mapping of fiber path orientations and simplifies application of boundary conditions.

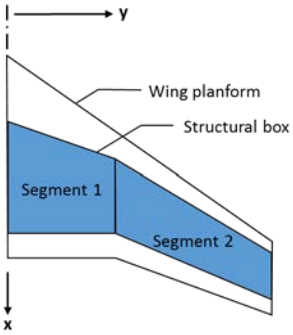


*Figure 3. Wing planform.*

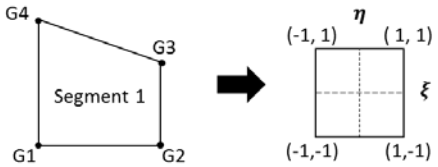


*Figure 4. Wing segment transformation.*

$$x(\xi,\eta) = \sum_{i=1}^{4} N_i(\xi,\eta)x_i$$
$$y(\xi,\eta) = \sum_{i=1}^{4} N_i(\xi,\eta)y_i \quad (1)$$

The Jacobian of this transform is used to transform quantities to the (ξ-η) domain and is given by

$$J = \begin{bmatrix} \frac{\partial x}{\partial \xi} & \frac{\partial y}{\partial \xi} \\ \frac{\partial x}{\partial \eta} & \frac{\partial y}{\partial \eta} \end{bmatrix}$$

$$\begin{aligned} \partial x/\partial \xi &= 1/4\,[(1+\eta)(x_3 - x_4) + (1-\eta)(x_2 - x_1)] \\ \partial y/\partial \xi &= 1/4\,[(1+\xi)(x_3 - x_2) + (1-\xi)(x_4 - x_1)] \\ \partial x/\partial \eta &= 1/4\,[(1+\eta)(y_3 - y_4) + (1-\eta)(y_2 - y_1)] \\ \partial y/\partial \eta &= 1/4\,[(1+\xi)(y_3 - y_2) + (1-\xi)(y_4 - y_1)] \end{aligned} \quad (2)$$

### C. Wing Cross Section

Wing skins are supported by rib and spar substructure as illustrated in Figure 5. The spars and ribs are modeled as assemblies of caps and webs as shown in Figure 6. The subscripts *1, 2* denotes spar and rib dimensions respectively.

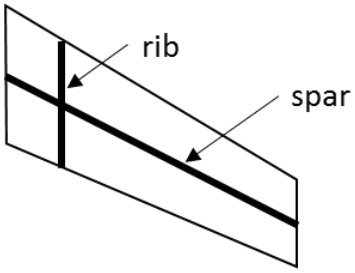


*Figure 5. Plan view of wing spar and rib.*

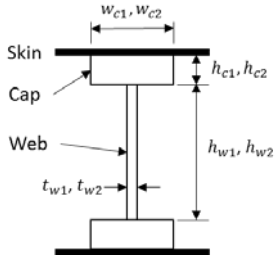


*Figure 6. Spar or rib geometry.*

Wing skin covers are modeled as layers of orthotropic material or as a single isotropic layer positioned relative to the z=0 reference plane. The 0-degree reference fiber direction is allowed to vary linearly along the primary structural axis $y'$for each wing segment using tow-steering construction and is governed by Eq. *(3)*. All layers are positioned at fixed angles of 0, +45, -45 and 90 degrees relative to the 0-degree fiber path throughout the skin as shown in Figure 7 and Figure 8. This provides the ability to steer laminate mechanical properties and preserving laminates with attractive manufacturing qualities. An extension of the linear variable curvilinear fiber path introduced by Gurdal and Olmedo in Ref. 14 is chosen for this study. It has the advantages of offering a wide range of variable stiffness designs and provides closed form relations for the fiber path and steering radius of curvature.

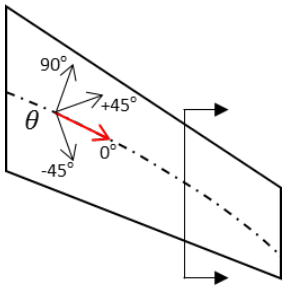


*Figure 7. Tow steered fiber reference path.*

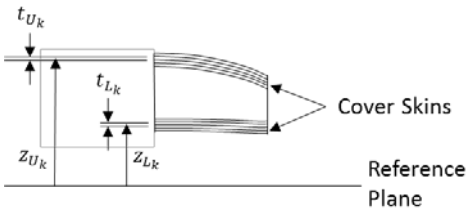


*Figure 8. Reference plane and wing skin layers.*

$$\theta(y') = \emptyset + (T_1 - T_0)\frac{y'}{s} + T_0 \quad (3)$$

### D. Wing Substructure Topology

Wing skin covers are subdivided into panels based on arrangement of the underlying rib-spar substructure as shown in Figure 9. Skin panel geometry is extracted from the spar-rib intersections and used to perform panel stability calculations. Skin panels are also transformed to a local (ξ-η) computational domain. Procedures outlined in Ref. 11 are used to perform the panel buckling analyses.

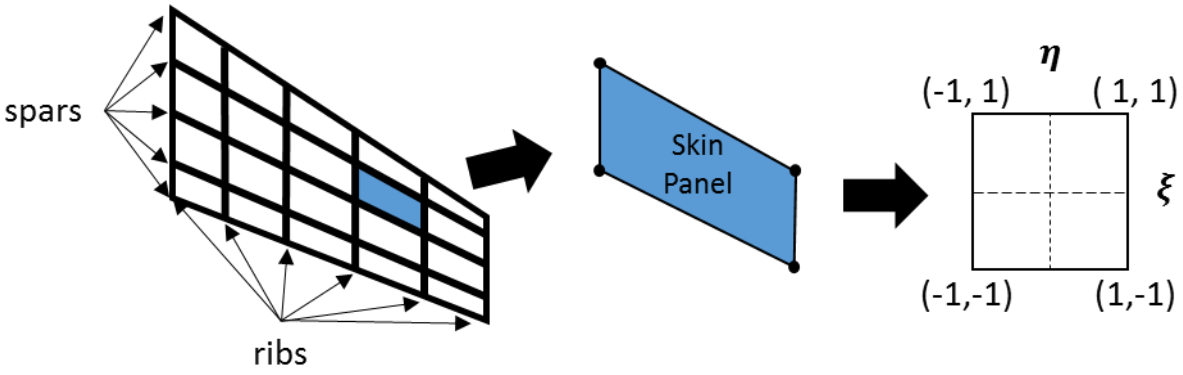


*Figure 9. Modeling of skin panels.*

## III. Analytical Approach

Both the Ritz and FEM methods have been implemented to model the wing structure. The Ritz approach is used to idealize the wing as an equivalent plate whereas the FEM approach utilizes a 3D discretized shell representation.

A First order shear deformation theory based on the Reissner-Mindlin formulation is used to capture transverse shear effects of the equivalent plate wing assembly. The Ritz method is used with Legendre polynomial basis functions to formulate static and free vibration problems. The curvilinear fiber path is modeled with laminate constitutive relations that allow the fiber angle to vary across the wing planform. The formulation is taken from Ref. 10 and 11 and repeated below for convenience.

### A. First Order Shear Deformation Theory

The displacement field $u, v, w$ throughout the wing is given by

$$\begin{aligned} u(x,y,z,t) &= u_0(x,y,t) + z\phi_x(x,y,t) \\ v(x,y,z,t) &= v_0(x,y,t) + z\phi_y(x,y,t) \\ w(x,y,z,t) &= w_0(x,y,t) \end{aligned} \tag{4}$$

Strain-displacement relations are given by

$$\begin{aligned} \varepsilon_x &= \varepsilon_x^0 + z\kappa_x^0 = \frac{\partial u_o}{\partial x} + z\frac{\partial \phi_x}{\partial x} \\ \varepsilon_y &= \varepsilon_y^0 + z\kappa_y^0 = \frac{\partial v_o}{\partial y} + z\frac{\partial \phi_y}{\partial y} \\ \varepsilon_z &= 0 \\ \gamma_{xy} = 2\varepsilon_{xy} &= \gamma_{xy}^0 + z\kappa_{xy}^0 = \left(\frac{\partial u_o}{\partial y} + \frac{\partial v_o}{\partial x}\right) + z\left(\frac{\partial \phi_x}{\partial y} + \frac{\partial \phi_y}{\partial x}\right) \\ \gamma_{yz} = 2\varepsilon_{yz} &= \frac{\partial v}{\partial z} + \frac{\partial w}{\partial y} = \phi_y + \frac{\partial w_0}{\partial y} \\ \gamma_{xz} = 2\varepsilon_{xz} &= \frac{\partial u}{\partial z} + \frac{\partial w}{\partial x} = \phi_x + \frac{\partial w_0}{\partial x} \end{aligned} \tag{5}$$

## B. Laminate Constitutive Relations

Composite skins are analyzed using constitutive relations based on classical lamination plate theory given by

$$\begin{Bmatrix}\sigma_{11}\\ \sigma_{22}\\ \tau_{12}\end{Bmatrix}=\begin{bmatrix}Q_{11} & Q_{12} & 0\\ Q_{12} & Q_{22} & 0\\ 0 & 0 & Q_{66}\end{bmatrix}\begin{Bmatrix}\varepsilon_{11}\\ \varepsilon_{22}\\ \varepsilon_{12}\end{Bmatrix} \tag{6}$$

where

$$\begin{aligned}Q_{11} &= E_1/(1-\nu_{12}\nu_{21})\\ Q_{12} &= E_1\nu_{21}/(1-\nu_{12}\nu_{21})\\ Q_{22} &= E_2/(1-\nu_{12}\nu_{21})\\ Q_{66} &= G_{12}\\ \nu_{21} &= \nu_{12}\,E_2/E_1\end{aligned} \tag{7}$$

Ply stress strain relations are given by

$$\begin{Bmatrix}\sigma_{xx}\\ \sigma_{yy}\\ \tau_{xy}\end{Bmatrix}=\begin{bmatrix}\bar{Q}_{11} & \bar{Q}_{12} & 0\\ \bar{Q}_{12} & \bar{Q}_{22} & 0\\ 0 & 0 & \bar{Q}_{66}\end{bmatrix}\begin{Bmatrix}\varepsilon_{xx}\\ \varepsilon_{yy}\\ \varepsilon_{xy}\end{Bmatrix}=[D]\{\varepsilon\} \tag{8}$$

Ply stiffnesses vary with local fiber direction $\theta(x,y)$ given by

$$\begin{aligned}\bar{Q}_{11}(x,y) &= U_1+U_2\cos[2\theta(x,y)]+U_3\cos[4\theta(x,y)]\\ \bar{Q}_{12}(x,y) &= U_4-U_3\cos[4\theta(x,y)]\\ \bar{Q}_{22}(x,y) &= U_1-U_2\cos[2\theta(x,y)]+U_3\cos[4\theta(x,y)]\\ \bar{Q}_{66}(x,y) &= U_5-U_3\cos[4\theta(x,y)]\\ \bar{Q}_{16}(x,y) &= -1/2\,U_2\sin[2\theta(x,y)]-U_3\cos[4\theta(x,y)]\\ \bar{Q}_{26}(x,y) &= -1/2\,U_2\sin[2\theta(x,y)]+U_3\cos[4\theta(x,y)]\end{aligned} \tag{9}$$

where the laminate invariants are given by

$$\begin{aligned}U_1 &= (3Q_{11}+3Q_{22}+2Q_{12}+4Q_{66})/8\\ U_2 &= (Q_{11}+Q_{22})/2\\ U_3 &= (Q_{11}+Q_{22}-2Q_{12}-4Q_{66})/8\\ U_4 &= (Q_{11}+Q_{22}+6Q_{12}-4Q_{66})/8\\ U_5 &= (Q_{11}+Q_{22}-2Q_{12}+4Q_{66})/8\end{aligned} \tag{10}$$

## C. Ritz Analysis Procedure

*1. Ritz Basis Functions*

The Ritz method is used to obtain an approximate solution to the displacement field of Eq. *(4)* by using assumed series expressions to describe the plate mid-plane deformation given by Eq. *(11)*. The $q_U, q_V, q_W, q_X, q_Y$ are unknown coefficients to be determined and the $B_{ij}, B_{kl}, B_{mn}, B_{pq}, B_{rs}$ basis functions are expressed in ξ-η.

$$\begin{aligned}u_0 &= \{B_{IJ}\}^T\{q_U\}=\sum_{i=1}^{I}\sum_{j=1}^{J}B_{ij}(\xi,\eta)q_{ij}(t)\\ v_0 &= \{B_{KL}\}^T\{q_V\}=\sum_{k=1}^{K}\sum_{l=1}^{L}B_{kl}(\xi,\eta)q_{kl}(t)\\ w_0 &= \{B_{MN}\}^T\{q_W\}=\sum_{m=1}^{M}\sum_{n=1}^{N}B_{mn}(\xi,\eta)q_{mn}(t)\\ \phi_x &= \{B_{PQ}\}^T\{q_X\}=\sum_{p=1}^{P}\sum_{q=1}^{Q}B_{pq}(\xi,\eta)\,q_{pq}(t)\\ \phi_y &= \{B_{RS}\}^T\{q_Y\}=\sum_{r=1}^{R}\sum_{s=1}^{S}B_{rs}(\xi,\eta)q_{rs}(t)\end{aligned} \tag{11}$$

where $I, J, K, L, M, N, P, Q, R, S$ are integers that depend on the order of the basis function polynomials.

This can be reduced to a more compact form

$$\begin{Bmatrix} u_0 \\ v_0 \\ w_0 \\ \phi_x \\ \phi_y \end{Bmatrix} = \left\{ \{B_{IJ}\}^T, \{B_{KL}\}^T, \{B_{MN}\}^T, \{B_{PQ}\}^T, \{B_{RS}\}^T \right\}^T \begin{Bmatrix} q_U \\ q_V \\ q_W \\ q_X \\ q_Y \end{Bmatrix} = [B]^T \{q\} \tag{12}$$

The displacement vector $\{q\}$ is

$$\{q\} = \{\{q_U\}^T, \{q_V\}^T, \{q_W\}^T, \{q_X\}^T, \{q_Y\}^T\}^T \tag{13}$$

The Ritz basis vectors $\{B\}$ are given by

$$[B] = \left\{ \{B_{IJ}\}^T, \{B_{KL}\}^T, \{B_{MN}\}^T, \{B_{PQ}\}^T, \{B_{RS}\}^T \right\}^T \tag{14}$$

*2. Strain Energy and Stiffness Matrix*

Strain energy for the wing structure is given by

$$U = \frac{1}{2} \iiint_V \{\sigma\}\{\varepsilon\} dV = \frac{1}{2} \iiint_V \{\varepsilon\}^T [D] \{\varepsilon\} dV \tag{15}$$

Strains are transformed to the (ξ-η) domain using the Jacobian relations

$$\begin{Bmatrix} \frac{\partial f}{\partial \xi} \\ \frac{\partial f}{\partial \eta} \end{Bmatrix} = \begin{bmatrix} \frac{\partial x}{\partial \xi} & \frac{\partial y}{\partial \xi} \\ \frac{\partial x}{\partial \eta} & \frac{\partial y}{\partial \eta} \end{bmatrix} \begin{Bmatrix} \frac{\partial f}{\partial x} \\ \frac{\partial f}{\partial y} \end{Bmatrix} = [J] \begin{Bmatrix} \frac{\partial f}{\partial x} \\ \frac{\partial f}{\partial y} \end{Bmatrix}$$

$$or \begin{Bmatrix} \frac{\partial f}{\partial x} \\ \frac{\partial f}{\partial y} \end{Bmatrix} = [J]^{-1} \begin{Bmatrix} \frac{\partial f}{\partial \xi} \\ \frac{\partial f}{\partial \eta} \end{Bmatrix}$$

$$where\ [\bar{J}] = [J]^{-1} = \frac{1}{|J|} \begin{bmatrix} J_{22} & -J_{12} \\ -J_{21} & J_{11} \end{bmatrix} = \begin{bmatrix} \bar{J}_{11} & \bar{J}_{12} \\ \bar{J}_{21} & \bar{J}_{21} \end{bmatrix} \tag{16}$$

The strain tensor is rewritten as

$$\{\varepsilon\} = \begin{Bmatrix} \varepsilon_x \\ \varepsilon_y \\ \varepsilon_{xy} \\ \varepsilon_{yz} \\ \varepsilon_{zx} \end{Bmatrix} = \begin{bmatrix} \bar{J}_{11} & \bar{J}_{12} & 0 & 0 & 0 & 0 & z\bar{J}_{11} & z\bar{J}_{12} & 0 & 0 & 0 & 0 \\ 0 & 0 & \bar{J}_{21} & \bar{J}_{22} & 0 & 0 & 0 & 0 & z\bar{J}_{21} & z\bar{J}_{22} & 0 & 0 \\ \bar{J}_{21} & \bar{J}_{22} & \bar{J}_{11} & \bar{J}_{12} & 0 & 0 & z\bar{J}_{21} & z\bar{J}_{22} & z\bar{J}_{11} & z\bar{J}_{12} & 0 & 0 \\ 0 & 0 & 0 & 0 & \bar{J}_{21} & \bar{J}_{22} & 0 & 0 & 0 & 0 & 1 & 0 \\ 0 & 0 & 0 & 0 & \bar{J}_{11} & \bar{J}_{12} & 0 & 0 & 0 & 0 & 0 & 1 \end{bmatrix} \{\bar{\varepsilon}\}$$

or

$$\{\varepsilon\} = [T_e]\{\bar{\varepsilon}\} \tag{17}$$

where

$$\{\bar{\varepsilon}\} = \begin{bmatrix} \frac{\partial u_o}{\partial \xi} & \frac{\partial u_o}{\partial \eta} & \frac{\partial v_o}{\partial \xi} & \frac{\partial v_o}{\partial \eta} & \frac{\partial w_o}{\partial \xi} & \frac{\partial w_o}{\partial \eta} & \frac{\partial \phi_x}{\partial \xi} & \frac{\partial \phi_x}{\partial \eta} & \frac{\partial \phi_y}{\partial \xi} & \frac{\partial \phi_y}{\partial \xi \eta} & \phi_x & \phi_y \end{bmatrix}^T$$

The Ritz basis functions can be used to write

$$\{\bar{\varepsilon}\} = [C]\{\bar{\varepsilon}\} \tag{18}$$

where

$$[C] = \begin{bmatrix} [B_{IJ,\xi\eta}] & 0 & 0 & 0 & 0 \\ 0 & [B_{KL,\xi\eta}] & 0 & 0 & 0 \\ 0 & 0 & [B_{MN,\xi\eta}] & 0 & 0 \\ 0 & 0 & 0 & [B_{PQ,\xi\eta}] & 0 \\ 0 & 0 & 0 & 0 & [B_{RS,\xi\eta}] \\ 0 & 0 & 0 & \{B_{PQ}\}^T & 0 \\ 0 & 0 & 0 & 0 & \{B_{RS}\}^T \end{bmatrix}$$

Substituting Eqs. *(17)* and *(18)* into Eq. *(15)* gives

$$U = \frac{1}{2}\iiint_V \{q\}^T[C]^T[T_e]^T[D][T_e][C]\{q\}dV \tag{19}$$

We can rewrite the strain energy to define a stiffness matrix in terms of $\{q\}$ as

$$U = \{q\}^T[K_q]\{q\} \tag{20}$$

where

$$[K_q] = \frac{1}{2}\iiint_V [C]^T[T_e]^T[D][T_e][C]dV \tag{21}$$

*3. Kinetic Energy and Mass Matrix*

Kinetic energy for the wing structure is given by

$$T = \frac{1}{2}\iiint_V \rho\bar{v}\,dV = \frac{1}{2}\iiint_V p\{\bar{v}\}^T\{\bar{v}\}dV \tag{22}$$

where the velocity vector $\bar{v}$ is given by

$$\{\bar{v}\} = \left\{\frac{\partial\bar{d}}{\partial t}\right\} = \begin{Bmatrix} \frac{\partial u_o}{\partial t} + z\frac{\partial\phi_x}{\partial t} \\ \frac{\partial v_o}{\partial t} + z\frac{\partial\phi_y}{\partial t} \\ \frac{\partial w_o}{\partial t} \end{Bmatrix} = \begin{bmatrix} 1 & 0 & 0 & z & 0 \\ 0 & 1 & 0 & 0 & z \\ 0 & 0 & 1 & 0 & 0 \end{bmatrix} \begin{Bmatrix} \frac{\partial u_o}{\partial t} \\ \frac{\partial v_o}{\partial t} \\ \frac{\partial w_o}{\partial t} \\ \frac{\partial\phi_x}{\partial t} \\ \frac{\partial\phi_y}{\partial t} \end{Bmatrix} = [Z][H]\{\dot{q}\}$$

Where $\{\bar{d}\}$ is the displacement vector

$$\{\bar{d}\} = \begin{Bmatrix} u \\ v \\ w \end{Bmatrix}, \qquad [\mathrm{Z}] = \begin{bmatrix} 1 & 0 & 0 & z & 0 \\ 0 & 1 & 0 & 0 & z \\ 0 & 0 & 1 & 0 & 0 \end{bmatrix}$$

$$[H] = \begin{bmatrix} \{B_{IJ}\}^T & 0 & 0 & 0 & 0 \\ 0 & \{B_{KL}\}^T & 0 & 0 & 0 \\ 0 & 0 & \{B_{MN}\}^T & 0 & 0 \\ 0 & 0 & 0 & \{B_{PQ}\}^T & 0 \\ 0 & 0 & 0 & 0 & \{B_{RS}\}^T \end{bmatrix} \tag{23}$$

The kinetic energy can be written as

$$T = \frac{1}{2}\iiint_V p\{\dot{q}\}^T[Z]^T[H]^T[Z][H]\{\dot{q}\}dV \tag{24}$$

Rewriting in matrix form gives

$$T = \frac{1}{2}\{\dot{q}\}^T\left[M_q\right]\{\dot{q}\} \tag{25}$$

where

$$\left[M_q\right] = \iiint_V p[Z]^T[H]^T[Z][H]dV \tag{26}$$

*4. Numerical Integration of Mass and Stiffness Matrix*

Numerical integration is used to evaluate stiffness and mass matrices given by Eq. *(21)* and Eq. *(26)* respectively. It is assumed that the order of the Ritz basis function polynomials are chosen such that $I = J = K = L = M = N = P = Q = R = S = k$. Thus, $\left[K_q\right]$ and $\left[M_q\right]$ will have dimension $N \times N$, where $N = 5k^2$.

The transformation given by Eq. *(1)* and the Jacobian given by Eq. *(2)* are used to write a general expression for transforming the integral $I(x, y, z)$ to $G(\xi, \eta, z)$ as follows

$$I = \iiint_V F(x, y, z)dV = \int_{-1}^{1}\int_{-1}^{1} G(\xi, \eta)d\xi d\eta \tag{27}$$

where

$$G(\xi, \eta) = \sum_{i=1}^{N_z}\int_{z_{i1}}^{z_{i2}} F[x(\xi, \eta), y(\xi, \eta), z]\,|J|dz \tag{28}$$

and $N_z$ is the number of integration zones in the z-direction and $z_{i1}$ and $z_{i2}$ are integration limits for the *i*-th zone. Gaussian quadrature is used to write the numerical value of Eq. (27) as

$$I \cong \sum_{i=1}^{M_g}\sum_{j=1}^{N_g} {g_i}^{(M_g)}\,{g_j}^{(N_g)} G\left[{\xi_i}^{(M_g)}, {\eta_i}^{(N_g)}\right] \tag{29}$$

Where ${g_i}^{(M_g)}$ and ${g_j}^{(N_g)}$ are quadrature weights, ${\xi_i}^{(M_g)}$ and ${\eta_i}^{(N_g)}$ are integration sampling points, and $M_g$ and $N_g$ are the maximum number of sampling points.

*a. Skins*

The contribution of lower and upper skin laminates in Figure 8 to mass and stiffness matrices is given by

$$\iiint_V F(x, y, z)dV = \int_{-1}^{1}\int_{-1}^{1}\left(\sum_{i=1}^{N_L}\int_{z_{L_k}-\frac{1}{2}t_{L_k}}^{z_{L_k}+\frac{1}{2}t_{L_k}} F|J|dz\right)d\xi d\eta + \int_{-1}^{1}\int_{-1}^{1}\left(\sum_{i=1}^{N_U}\int_{z_{U_k}-\frac{1}{2}t_{U_k}}^{z_{U_k}+\frac{1}{2}t_{U_k}} F|J|dz\right)d\xi d\eta \tag{30}$$

where the subscripts *L, U* designate lower and upper skin, respectively. Calculation of Eq. *(21)* and Eq. *(26)* using Eq. *(30)* gives the skin stiffness and matrices $[M_{skin}]$ and $[K_{skin}]$

*b. Spar Caps*

Contributions to mass and stiffness from spar caps shown in *Figure 6* are given by

$$\iiint_V F(x, y, z)dV = \int_{-1}^{1} d\eta \int_{\xi_s(\eta)-\frac{w_s}{c}}^{\xi_s(\eta)+\frac{w_s}{c}} d\xi \left(\int_{z_L+t_L}^{z_L+t_L+h_s} + \int_{z_U-t_U-h_s}^{z_U-t_U}\right) F[x(\xi, \eta), y(\xi, \eta), z]\,|J|dz \tag{31}$$

$$= \int_{-1}^{1} d\eta \int_{-1}^{1} ({}^{w_s}/_{c}) d\xi \left( \int_{z_L+t_L}^{z_L+t_L+h_s} + \int_{z_U-t_U-h_s}^{z_U-t_U} \right) F\{x[({}^{w_s}/_{c})\xi + \xi_s(\eta), \eta], y[({}^{w_s}/_{c})\xi + \xi_s(\eta), \eta], z\} |J| dz$$

where $c$ is the chord length at $\eta$: $c = \frac{1}{2}c_0(1-\eta) + \frac{1}{2}c_1(1+\eta)$, $c_0$ is the chord length at wing root, and $c_1$ is the chord length at wing tip, and $\xi_s(\eta)$ I s the spar postion.

*c. Spar Webs*

Contributions to mass and stiffness from spar webs shown in *Figure 6* are given by

$$\iiint_V F(x,y,z)dV = \int_{\xi_s-\frac{w_s}{c}}^{\xi_s+\frac{w_s}{c}} \int_{-1}^{1} \int_{z_L+t_L+h_s}^{z_U-t_U-h_s} F[x(\xi,\eta), y(\xi,\eta), z]\,|J| d\xi d\eta dz$$
$$= \int_{-1}^{1} d\eta \int_{-1}^{1} ({}^{t_s}/_{c}) d\xi \int_{z_L+t_L+h_s}^{z_U-t_U-h_s} F\left\{x\left[\left({}^{t_s}/_{c}\right)\xi + \xi_s(\eta), \eta\right], y\left[\left({}^{t_s}/_{c}\right)\xi + \xi_s(\eta), \eta\right], z\right\} |J| dz \quad (32)$$

Eqs. *(31)* and *(32)* are summed for all spar caps and webs to give the stiffness and mass matrices of the ribs $[M_{spar}]$ and $[K_{spar}]$.

*d. Rib Caps*

Contributions to mass and stiffness from rib caps are given by

$$\iiint_V F(x,y,z)dV = \int_{-1}^{1} \int_{\eta_r-\frac{w_r}{c}}^{\eta_r+\frac{w_r}{s}} \left( \int_{z_L+t_L}^{z_L+t_L+h_r} + \int_{z_U-t_U-h_r}^{z_U-t_U} \right) F[x(\xi,\eta), y(\xi,\eta), z]\,|J| d\xi d\eta dz$$
$$= \int_{-1}^{1} d\xi \int_{-1}^{1} ({}^{w_r}/_{c}) d\eta \left( \int_{z_L+t_L}^{z_L+t_L+h_r} + \int_{z_U-t_U-h_r}^{z_U-t_U} \right) F\{x[\xi, ({}^{w_r}/_{s})\eta + \eta_r(\xi)], y[\xi, ({}^{w_r}/_{s})\eta + \eta_r(\xi)], z\} |J| dz \quad (33)$$

where $s$ is the wing span and $\eta_r(\xi)$ is the rib position function.

*e. Rib Webs*

Contributions to mass and stiffness from rib caps are given by

$$\iiint_V F(x,y,z)dV = \int_{-1}^{1} \int_{\eta_r-\frac{t_r}{c}}^{\eta_r+\frac{t_r}{s}} \int_{z_L+t_L+h_r}^{z_U-t_U-h_s} F[x(\xi,\eta), y(\xi,\eta), z]\,|J| d\xi d\eta dz$$
$$= \int_{-1}^{1} d\xi \int_{-1}^{1} ({}^{t_r}/_{s}) d\eta \int_{z_L+t_L+h_r}^{z_U-t_U-h_s} F\left\{x\left[\xi, \left({}^{t_r}/_{s}\right)\eta + \eta_r(\xi)\right], y\left[\xi, \left({}^{t_r}/_{s}\right)\eta + \eta_r(\xi)\right], z\right\} |J| dz \quad (34)$$

Eqs. *(33)* and *(34)* are summed for all rib caps and webs to give the stiffness and mass matrices of the ribs $[M_{rib}]$ and $[K_{rib}]$

*5. Potential Energy of External Transverse Loads*

The work $W$ due to a uniform transverse load $p_o$ and point loads $P_l$ can be expressed as

$$W = \iint_A p_o\{q_W\}\, dxdy + \sum_l P_l\{q_W\} \quad (35)$$

We may write this in terms of a generalized load vectors

$$W = \{P_q\} = \{P_0\} + \{P_L\} \quad (36)$$

where

$$\{P_o\} = \iint_A p_o [d_t]^T \{q\} |J| d\xi d\eta \tag{37}$$

$$\{P_L\} = \sum_l P_l \, [d_t]^T \{q\}|_{(\xi_l, \eta_l)} \tag{38}$$

$$[d_t] = [0 \quad 0 \quad \{B_{MN}\}^T \quad 0 \quad 0] \tag{39}$$

*6. Boundary Conditions: Null Space Approach*

Boundary conditions include combinations of simple, clamped or free edge displacement conditions along plate edges. To simplify their specification for a generalized quadrilateral geometry, they are applied in the (ξ-η) computational domain given by Eq.*(40)*.

$$\begin{gathered} u = 0 \\ w = 0 \\ w = 0 \\ \phi_x = 0 \\ \phi_y = 0 \end{gathered} \tag{40}$$

The basis functions do not satisfy these conditions and must be enforced in a more general way. Eq.*(40)* can be written in matrix form for fully clamped conditions as

$$[A]\{q\} = 0$$

or

$$[A]\{q\} = \begin{Bmatrix} u|_{\xi=-1} \\ v|_{\xi=-1} \\ w|_{\xi=-1} \\ \phi_x|_{\xi=-1} \\ \phi_y|_{\xi=-1} \\ \dots \end{Bmatrix} \{q\} = 0 \tag{41}$$

Eq. *(41)* indicates the coefficients $\{q\}$ are not linearly independent. A set of linearly independent coordinates $\{\bar{q}\}$ are defined such that

$$\{q\} = [T]\{\bar{q}\} \tag{42}$$

Here $[T]$ is an unknown transformation matrix. Substituting Eq. *(42)* into Eq. *(41)* gives

$$[A][T]\{\bar{q}\} = \{0\} \tag{43}$$

Since $\{q\}$ is a set of independent coordinates, it follows that

$$[A][T] = [0] \tag{44}$$

Thus $[T]$ is the null space of matrix $[A]$, or

$$[T] = null([A]) \tag{45}$$

The energy expressions can now be expressed in terms of the fully generalized, linearly independent coordinates $\{\bar{q}\}$. The strain energy is written as

$$U = \frac{1}{2}\{\bar{q}\}^T [T]^T [K_q][T]\{\bar{q}\} = \frac{1}{2}\{\bar{q}\}^T [K_{\bar{q}}]\{\bar{q}\}$$

where

$$[K_{\bar{q}}] = [T]^T [K_q][T] \tag{46}$$

The kinetic energy is written as

$$T = \frac{1}{2}\{\dot{\bar{q}}\}[T]^T [M_q][T]\{\dot{\bar{q}}\} = \frac{1}{2}\{\dot{\bar{q}}\}[M_{\bar{q}}]\{\dot{\bar{q}}\} \tag{47}$$

where

$$[M_{\bar{q}}] = [T]^T [M_q][T]$$

Similarly, the potential energy terms can be written as

$$W = \{P_q\}[T]\{q\} = \{P_{\bar{q}}\}^T \{\bar{q}\} \tag{48}$$

*7. Analysis Problems*

The free vibration eigenvalue problem is formulated by taking the stationary value

$$\frac{\partial(T-U)}{\partial(B_{IJ}, B_{KL}, B_{MN}, B_{PQ}, B_{RS})} = 0 \tag{49}$$

The natural frequencies and mode shapes for the plate are obtained by solving the eigenvalue problem.

$$[K_{\bar{q}} - \lambda M_{\bar{q}}]\{\bar{q}\} = 0 \tag{50}$$

The static analysis problem is formulated from the stationary value

$$\frac{\partial(U+W)}{\partial(B_{IJ}, B_{KL}, B_{MN}, B_{PQ}, B_{RS})} = 0 \tag{51}$$

The displacement vector is obtained by solving

$$[K_{\bar{q}}]\{\bar{q}\} = \{F_{\bar{q}}\} \tag{52}$$

The mass matrix $[M_{\bar{q}}]$ and stiffness matrix $[K_{\bar{q}}]$ represent the total system mass stiffness such that

$$[K_{\bar{q}}] = [K_{Total}] = [K_{skin}] + [K_{spar}] + [K_{rib}] \tag{53}$$

$$[M_{\bar{q}}] = [M_{Total}] = [M_{skin}] + [M_{spar}] + [M_{rib}] \tag{54}$$

## IV. Implementation

Numerical solutions were implemented using OpenVSP and MATLAB (Ref. 35). This process is depicted in Figure 10 and begins with definition of the wing geometry using OpenVSP. The wing can be designed interactively or automatically generated using the OpenVSP scripting language. The wing definition is exported to a degenerative geometry file and imported to Matlab for development of the equivalent plate analysis. Static and vibration analyses can be performed for the full wing assembly and buckling solutions are performed for wing skin panels. The methodology also provides a capability to generate an in-line Nastran finite element model representation of the wing.

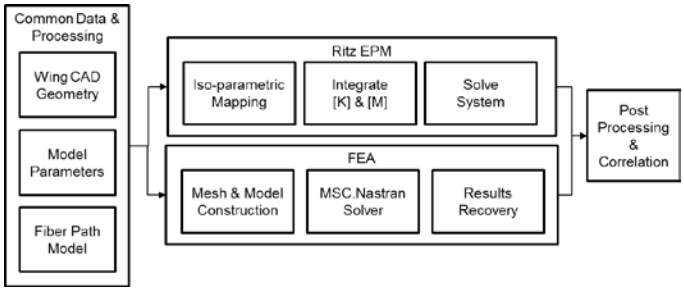


*Figure 10. Process flow of tow steered wing skin analysis.*

## A. Ritz Equivalent Plate Model

The Ritz EPM modeling process is depicted in Figure 12 and has been implemented as a MATLAB numerical procedure. The 3D wing surface geometry is extracted as a degenerative geometry export file from the OpenVSP software and can be read directly by MATLAB. Analysis parameters input to define the analysis problem type, polynomial degree, skin layer orientations and thickness, rib/spar geometry and rib/spar materials/section properties.

The wing mid-camber physical geometry is extracted from the OpenVSP geometry and mapped to the (ξ-η) computational domain as seen in Figure 12 a-b. Gaussian quadrature integration points defined in the (ξ-η) space are used to compute a fiber path field representing the 0-degree tow-steered reference direction and then projected to the wing skin surfaces to obtain the lower and upper layer offset heights ($z_U$, $z_U$) as seen in Figure 12 c-e.

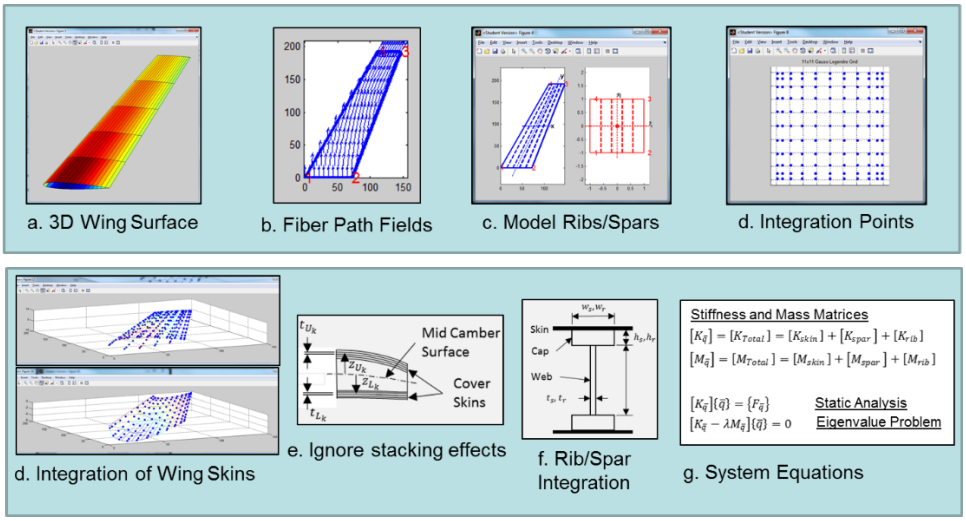


*Figure 11. Ritz Equivalent Plate Modeling Process.*

To simplify calculations, stacking sequence effects are ignored and all layers for a given cover skin are assumed to be located at the same distance from the the mid-camber reference surface. The skin stiffness and mass matrices are computed using numerical integration of Eq. *(21)* and *(30)*. A similar process is used to calculate mass and stiffness matrices for ribs and spar section geometry depicted in Figure 12 f and defined by Eqs. *(21)*, *(31)*, *(32)*, *(33)* and *(34)*. The total stiffness and mass matrices are computed as an assembly of the skin, ribs and spars and the used to solve a static or eigenvalue analysis problem as shown in Figure 12 g.

## B. Finite Element Model

The wing finite element model was constructed using the framework as shown in Figure 12. The wing mid-camber geometry is extracted from the OpenVSP geometry and used to create a 2D planform mesh with element edge lengths sized to accommodate rib and spar structure. The 2D mesh is projected to the upper and lower wing surfaces to create a shell model of the wing. Beam elements are used to model spar and rib caps while webs are modeled using CQUAD4 elements. Composite skin layers were modeled using PCOMP property definitions with a SMEAR laminate stacking sequence to match the Ritz EPM. Local ply orientations were extracted at element centroids evaluated from the fiber path field.

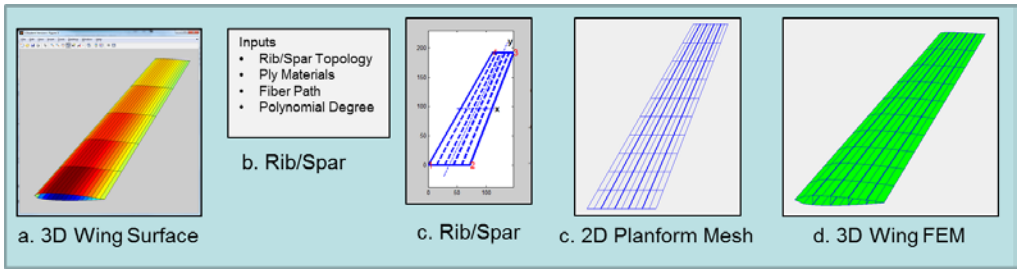


*Figure 12. Wing Finite Element Modeling Process.*

# V. Results and Discussion

## A. Validation Models

Validation models were used to assess the accuracy and performance of the modeling methods for various wing constructions clamped at the root. Results were generated for free vibration and static load conditions using both the Ritz EPM and MSC.NASTRAN commercial FEM solver. Two planform geometries, uniform and swept, were chosen for this study as shown in Figure 11. Both have a span of 192 in., a root chord with of 72in. and a tip chord width of 35 in. The uniform wing uses a rounded rectangular air foil with a constant thickness-chord ratio of 0.833. The swept wing cross-section is symmetrical and based on a NACA 0015 air foil with a thickness-chord ratio of 0.15 at the root and 0.06 at the tip.

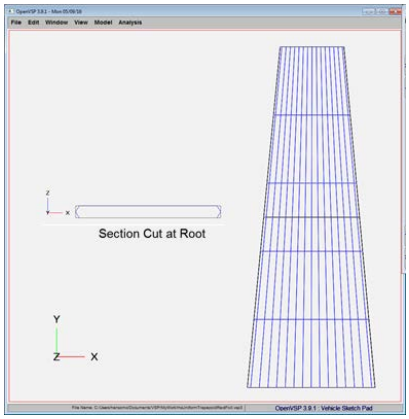


Uniform Planform

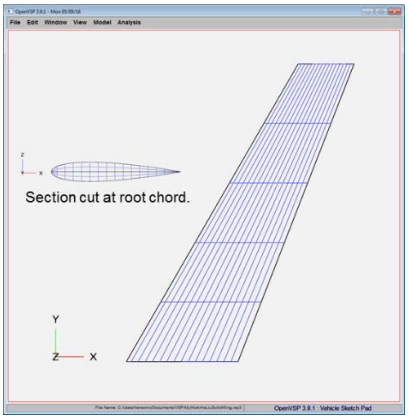


Swept Planform

| Parameter | Uniform Planform | Swept Planform |
|---|---|---|
| Span | 192 in. | 192 in. |
| Root Chord Width | 72 in. | 72 in. |
| Tip Chord Width | 36 in. | 36 in. |
| Sweep Angle | 5.5° | 30° |
| Air Foil | Rounted Rectangle | NACA 0015 |
| t/c (root) | 0.0833 | 0.15 |
| t/c (tip) | 0.0833 | 0.06 |

*Figure 13. Wing Planform Geometries.*

Three wing models of varying complexity were constructed as described in Table 1. The trapezoidal plate represents a uniform trapezoid wing shaped surface constructed of an isotropic material with a linearly varying thickness from root to tip. The core filled wing represents a uniform trapezoid with upper and lower unidirectional composite skins and full-depth honeycomb core. The tow steered wing represents a swept trapezoid wing with tow-steered composite skins and four supporting spars. Table 2 summarizes the materials and mechanical properties used in the analysis models.

*Table 1. Model Parameters.*

| Model | Planform | $n_{spars}$ | $n_{ribs}$ | Skin Definition | Skin Material | Rib/Spar/Core Material |
|---|---|---|---|---|---|---|
| Trapezoidal Plate | Uniform | - | - | Linear Varying Thickness $t_{root}$=0.180in., $t_{tip}$=0.090 | Aluminum | - |
| Core Filled Wing | Uniform | - | - | 4-Layer Unidirectional Laminate [0/+45/-45/90] | Carbon/Ep | Honeycomb |
| Tow Steered Wing | Swept | 4 | 0 | 4-Layer Tow Steered Laminate [0/+45/-45/90] | Carbon/Ep | Aluminum |

*Table 2. Materials and Mechanical Properties.*

| Material | *E or $E_1$(Msi)* | *$E_2$(Msi)* | *$G_{12}$(Msi)* | *$\nu$ or $\nu_{12}$* | *$\rho$*(lb/in$^3$) |
|---|---|---|---|---|---|
| Aluminum | 10.0 | - | | 0.3 | 0.10 |
| Carbon/Epoxy | 22.15 | 1.38 | 0.86 | 0.321 | 0.058 |
| Honeycomb | 0.68 | 0.68 | 0.26 | | .00231 |

## B. Trapezoidal Plate Results

Comparisons are made in Figure 14 of free vibration results between the Ritz EPM and those obtained from FEA using MSC.Nastran. The EPM utilized a polynomial of degree 11 with 605 DOF and the FEM model employed 144 shell CQUAD4 elements and 169 nodes with 1014 DOF. It can be seen that the first three modes computed using EPM lie within 8.90% of the FEA results and modes higher than four lie with 8.37-17.17%.

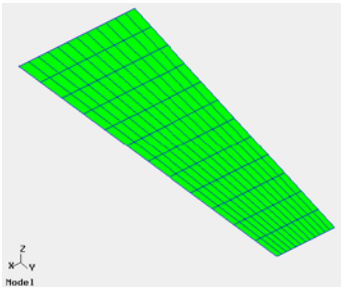


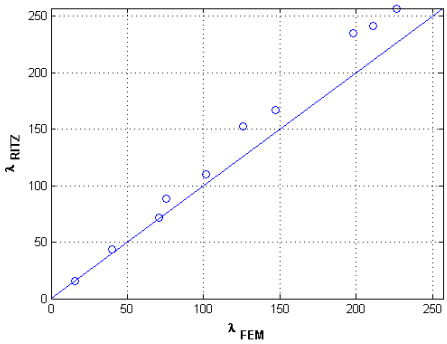


| Ritz EPM | FEM | % Error |
|---|---|---|
| 15.9 | 15.5 | 2.49 |
| 43.6 | 40.0 | 8.90 |
| 71.5 | 70.8 | 0.90 |
| 88.4 | 75.4 | 17.17 |
| 109.7 | 101.3 | 8.37 |
| 152.2 | 125.6 | 21.12 |
| 166.7 | 147.0 | 13.42 |
| 235.2 | 198.0 | 18.76 |
| 240.9 | 210.8 | 14.27 |
| 256.8 | 226.1 | 13.59 |

*Figure 14. Comparison of Ritz EPM and FEM Free Vibration Eigenvalues for Trapezoidal Plate.*

Comparisons are made in Figure 15 between Ritz EMP and FEA for deflections and principal strains resulting from a uniform pressure loading of p=-0.05psi. The results agree well between Ritz and FEA.

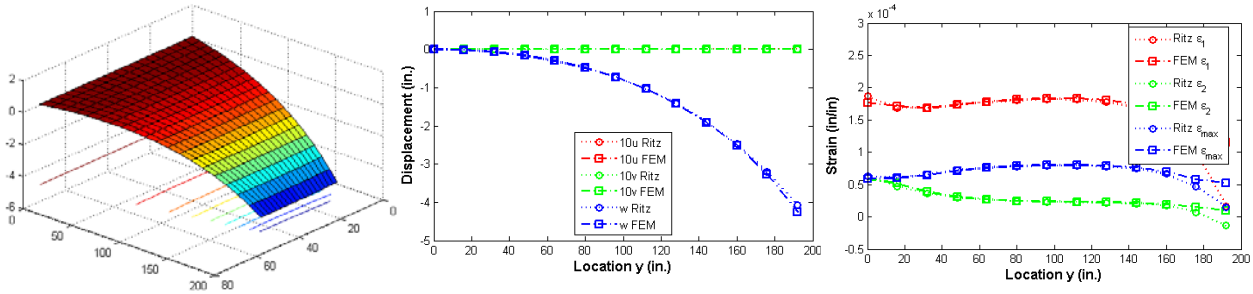


*Figure 15. Comparison of Ritz EPM and FEM Results for Uniform Pressure Loading of Trapezoidal Plate.*

Comparisons are made in between Ritz EMP and FEA for deflections and principal strains resulting from a tip torque +/- 1 lb. applied to the leading and trailing edge tip. The results agree well between Ritz and FEA with exception of the final endpoint near the wing tip.

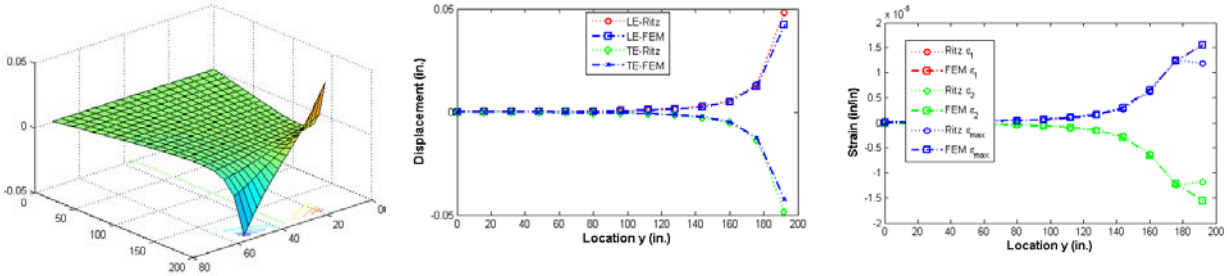


*Figure 16. Comparison of Ritz EPM and FEM Results for Tip Torque Loading of Trapezoidal Plate.*

## C. Core Filled Wing

Comparisons are made in Figure 17 of free vibration results between the Ritz EPM and those obtained from FEA using MSC.Nastran. The EPM utilized a polynomial of degree 11 with 605 DOF and the FEM model employed 288 shell CQUAD4 elements, 144 solid (CPENTA, CHEXA) elements and 338 nodes with 2028 DOF. It can be seen that modes 1, 2, 4 and 5 computed using EPM lie within -5.93% of the FEA results and the other modes lie between -20.58% and 25.22%.

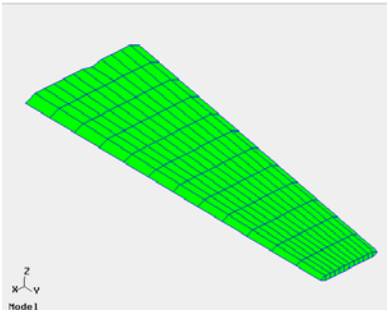

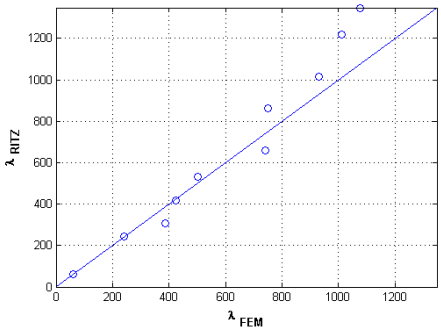


| Ritz EPM | FEM | % Error |
|---|---|---|
| 60.6 | 59.4 | 2.08 |
| 244.7 | 241.2 | 1.45 |
| 307.1 | 386.7 | -20.57 |
| 417.2 | 424.3 | -1.68 |
| 530.9 | 500.7 | 6.03 |
| 660.2 | 739.2 | -10.69 |
| 863.8 | 750.9 | 15.03 |
| 1014.2 | 928.1 | 9.27 |
| 1218.7 | 1011.7 | 20.46 |
| 1348.1 | 1076.1 | 25.28 |

*Figure 17. Comparison of Ritz EPM and FEM Free Vibration Eigenvalues for Core Filled Wing with C/Ep Skins.*

Comparisons are made in Figure 18 between Ritz EMP and FEA for deflections and principal strains resulting from a uniform pressure loading of p=-0.5psi. The displacement results agree well between Ritz and FEA.

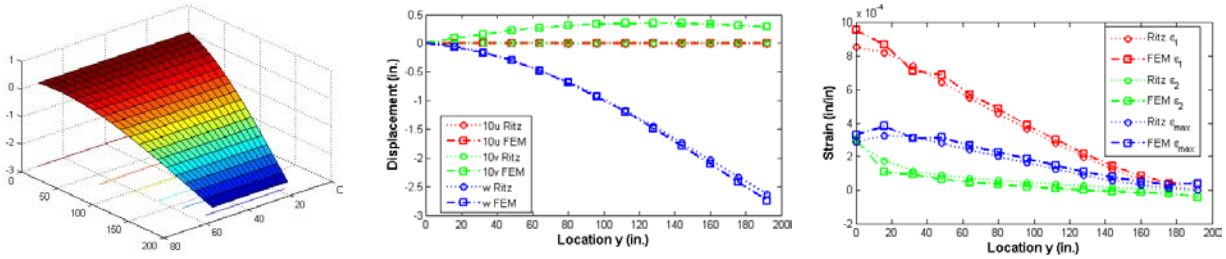


*Figure 18. Comparison of Ritz and FEM Results for Uniform Pressure Loading of Core Filled Wing with C/Ep Skins.*

Comparisons are made in Figure 19 between Ritz EPM and FEA for deflections and principal strains resulting from a tip torque load condition. The torque loading was defined by a unit load acting on the leading edge tip in the +z direction and a unit loading acting on the trailing edge tip in the –z direction. The results agree reasonably well between Ritz and FEA but show a growing difference moving towards the wing tip.

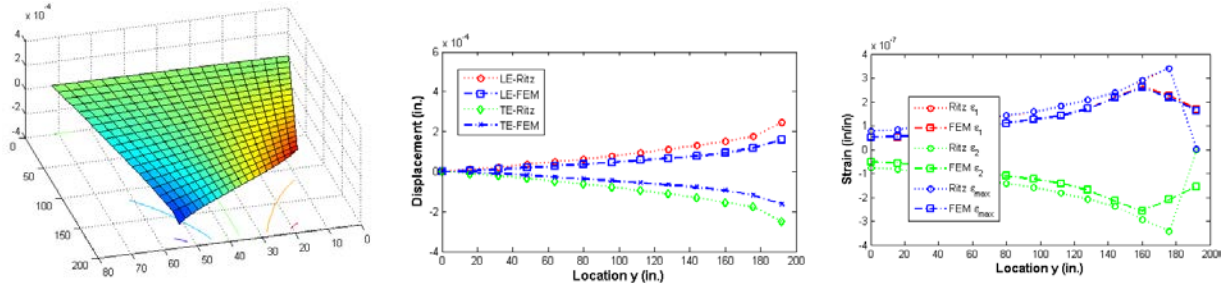


*Figure 19. Comparison of Ritz EPM and FEM Results for Tip Torque Loading of Core Filled Wing with C/Ep Skins.*

## D. Tow Steered Wing

The tow steered wing has cover skins comprised of 4 tow-steered layers as shown in Figure 20. The reference 0-degree path varies linearly from wing to tip as given by Eq. *(3)* and has an initial orientation of 0-degrees at the root and -30-degrees at the tip. The +45, -45 and 90 layers are linked to the 0-degree reference path and follow the same variation. The upper and lower skins use the same definition in this example. The skins are supported by 4 evenly distributed spars as shown by the FEM given in Figure 21.

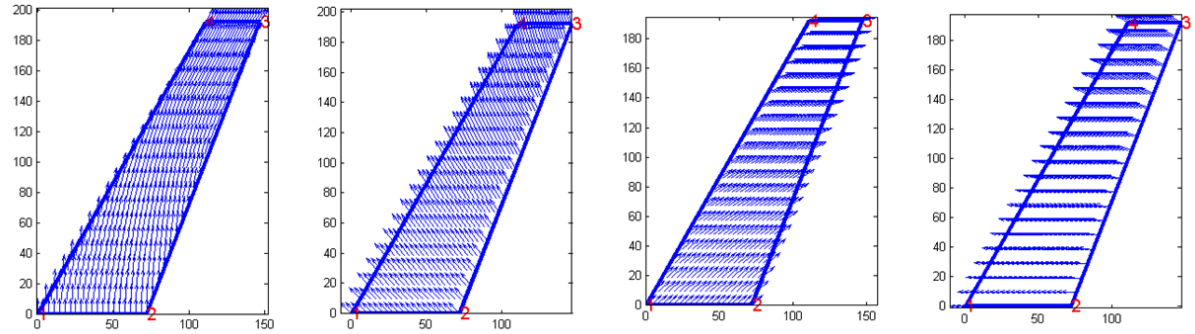

*Figure 20. Fiber Path Fields for 0, +45, -45, 90 Layers of Tow Steered Wing.*

Comparisons are made in Figure 20 of free vibration results between the Ritz EPM and those obtained from FEA using MSC.Nastran for the tow steered wing. The EPM utilized a polynomial of degree 11 with 605 DOF and the FEM model employed 880 shell CQUAD4 elements, 160 beam elements representing the spar caps and 882 nodes with 5292 DOF. It can be seen that the first 5 modes computed using EPM lie within -9.59 to 1.71% of the FEA results and the other modes lie between 10.36% and 40.63%.

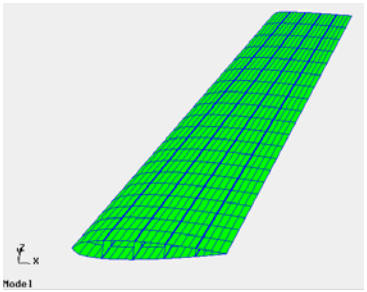

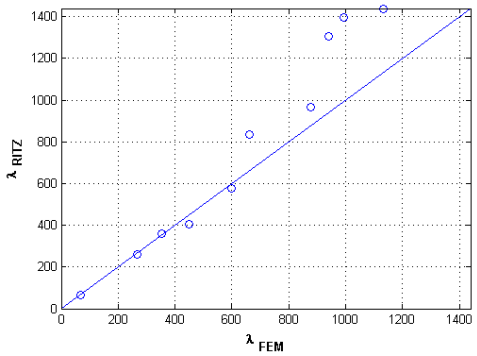


| Ritz EPM | FEM | % Error |
|---|---|---|
| 66.5 | 67.0 | -0.66 |
| 260.0 | 268.5 | -3.15 |
| 358.9 | 352.9 | 1.71 |
| 405.8 | 448.8 | -9.59 |
| 576.6 | 597.4 | -3.48 |
| 836.0 | 661.1 | 26.46 |
| 967.8 | 876.9 | 10.36 |
| 1305.3 | 939.4 | 38.95 |
| 1398.4 | 994.4 | 40.63 |
| 1439.4 | 1131.3 | 27.23 |

*Figure 21. Comparison of Ritz EPM and FEM Free Vibration Eigenvalues for Tow Steered Wing.*

Comparisons are made in Figure 21between Ritz EMP and FEA for deflections and principal strains resulting from a uniform pressure loading of p=-0.5psi. The displacement and strain results agree reasonably well and exhibit consistent between Ritz and FEA, but the principal strains show more significant disagreement particularly at the wing root.

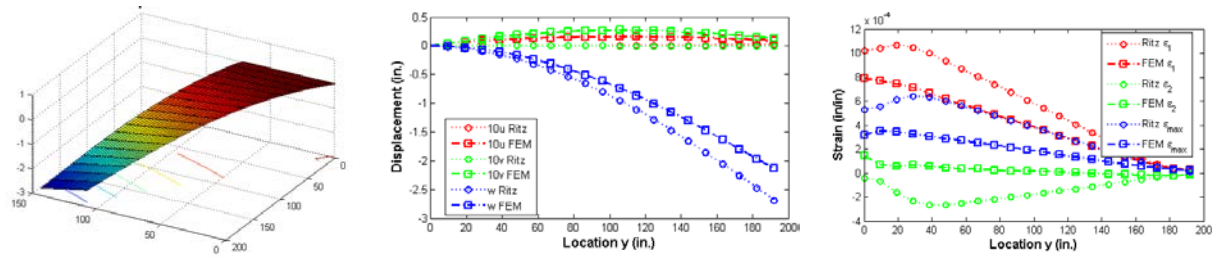


*Figure 22. Comparison of Ritz and FEM Results for Uniform Pressure Loading of Tow Steered Wing.*

Comparisons are made in Figure 22 between Ritz EPM and FEA for deflections and strains resulting from a tip torque load condition. The torque loading was defined by a unit load acting on the leading edge tip in the +z direction and an unit loading acting on the trailing edge tip in the –z direction. The displacement results agree well between Ritz and FEA whereas larger differences are present in the strain results.

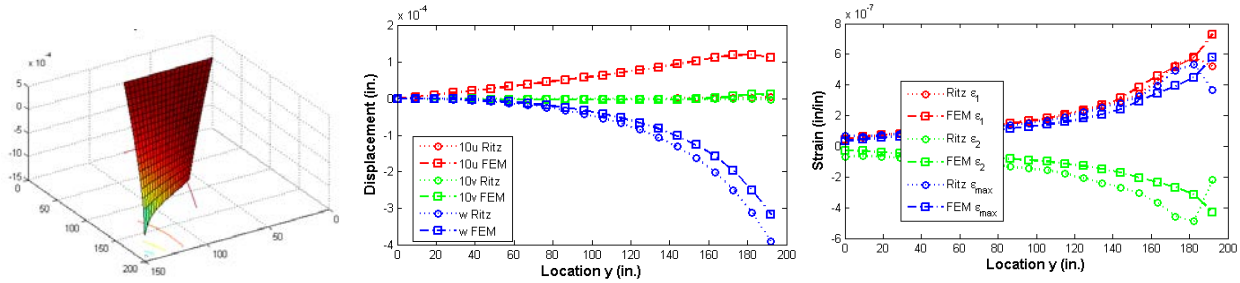


*Figure 23. Comparison of Ritz EPM and FEA Results for Tip Torque Loading of Tow Steered Wing.*

## E. Efficiency Comparison

A comparison of efficiency between the Ritz EPM and FEA has been made in Table 3. Details in terms of degrees of freedom (DOF), run time and number of FEA elements, for each of the wing analyses has been compared between EPM using two polynomial levels of ($N_p = 6, 8, 10$) and for FEA. Run times between EPM ($N_p = 6, 8$) and FEA are generally comparable, however substantial increases in run time result using EPM at ($N_p$ =10). A comparison of the DOF shows that FEA has a substantially larger DOF, ranging from 1.8X-5.6X (trapezoidal plate) and between 8.7X to 29.4X (tow steered wing).

The comparison should be considered somewhat qualitative since the EPM was coded in MATLAB m-file code and MSC/NASTRAN is coded in FORTRAN and highly optimized. Recoding EPM using a language such as FORTRAN or C++ would provide a more direct comparison of computational effort.

*Table 3. Efficiency Comparison of Ritz EPM and FEA.*

| Case | EPM ($N_p$=6) | | EPM ($N_p$=8) | | EPM ($N_p$=10) | | FEA | | |
|---|---|---|---|---|---|---|---|---|---|
| | DOF | Time (s) | DOF | Time (s) | DOF | Time (s) | No. of Elements | DOF | Time (s) |
| Trapezoidal Plate | 180 | 0.15 | 320 | 0.67 | 605 | 7.01 | 144 | 1014 | 1.51 |
| Core Filled Wing | 180 | 1.06 | 320 | 2.43 | 605 | 11.88 | 432 | 2028 | 1.71 |
| Tow Steered Wing | 180 | 4.78 | 320 | 10.32 | 605 | 30.23 | 1040 | 5292 | 2.40 |

## VI. Closing Remarks

An efficient framework has been developed to enable static and vibration analyses of wing structures and accommodates tow-steered wing skin constructions. It supports use of both a Ritz EPM and FEA analysis methodology. Comparison of results generated by the Ritz EMP with those using the commercial MSC.Nastran FEA code showed reasonably good agreement between the two methods. Accuracy of the EPM free vibration mode shapes and natural frequencies was generally limited to the first three to six modes. It was also shown that static displacements and strains also have generally good agreement between EPM and FEA. The capability is suitable for early conceptual wing design. More investigation is recommended to improve accuracy of the EPM.



## References

[1]McCullers, L. A., and R. W. Lynch. "Dynamic Characteristics of Advanced Filamentary Composite Structures", Vol II, Aeroelastic Synthesis Procedure Development, AFFDL-TR-111. AFFDL-TR-73-111 Vol. Air Force Flight Dynamics Laboratory, 1973.

[2]Rogers, W. A., and R. W. Lynch. "Aeroelastic Tailoring of Advanced Composite Structures for Military Aircraft: Volume 3 - Modification and User's Guide for Procedure TSO," AFFDL-76-100. AFFDL-76-100 Vol. , 1978.

[3]Giles, G.L. "Equivalent Plate Analysis of Aircraft Wing Box Structures with General Planform Geometry." American Institute of Aeronautics and Astronautics, 1986. Structures, Structural Dynamics, and Materials and Co-Located Conferences.

[4]Giles, G.L. "Further Generalization of an Equivalent Plate Representation for Aircraft Structural Analysis." American Institute of Aeronautics and Astronautics, 1987. Structures, Structural Dynamics, and Materials and Co-Located Conferences.

[5]Giles, G.L. "Equivalent Plate Modeling for Conceptual Design of Aircraft Wing Structures." American Institute of Aeronautics and Astronautics, 1995.

[6]Giles, G.L. Design Oriented Structural Analysis. NASA Technical Memorandum 109124 Vol. National Aeronautics and Space Administration, 1999.

[7]Stone, C.S., Henderson, J.L., Nazari, M.M., Boyd, W.N., Becker, B.T., Bhatia, K.G., "Evaluation of Equivalent Laminated Plate Solution (ELAPS) In HSCT Sizing", American Institute of Aeronautics and Astronautics, 2000.

[8]Tizzi, S., "Numerical Procedure for the Dynamic Analysis of Three-Dimensional Aeronautical Structures", Journal of Aircraft, 34, No. 1, 1997, pp. 121-130.

[9]Livne, E., "Equivalent Plate Structural Modeling for Wing Shape Optimization Including Transverse Shear", AIAA Journal, Vol. 32,No. 6, 1994, pp. 1278-1288.

[10]Kapania, R.K. and Liu, Y. "Static and Vibration Analyses of General Wing Structures Using Equivalent Plate Models", American Institute of Aeronautics and Astronautics, 2000. Structures, Structural Dynamics, and Materials and Co-Located Conferences.

[11]Henson, M.C., and Wang, B.P. "Vibration and Buckling of Quadrilateral Variable Stiffness Laminated Composite Plates", American Institute of Aeronautics and Astronautics, 2016 Sci-Tech Conference.

[12]Hyer, M., and R. Charette. "The use of Curvilinear Fiber Format in Composite Structure Design." American Institute of Aeronautics and Astronautics, 1989. Structures, Structural Dynamics, and Materials and Co-Located Conferences.

[13]Hyer, M. W., and H. H. Lee. "The use of Curvilinear Fiber Format to Improve Buckling Resistance of Composite Plates with Central Circular Holes." Composite Structures 18.3 (1991): 239-61.

[14]Gurdal, Z., and Olmedo, R., "In-Plane Response of Laminates with Spatially Varying Fiber Orientations - Variable Stiffness Concept." AIAA Journal 31.4 (1993).

[15]Tatting, B. F., and Z. Gurdal. Design and Manufacture of Elastically Tailored Tow Placed Plates. NASA/CR-2002–211919 Vol. , 2002.

[16]Gurdal, Z., Tatting, B., and Wu, K. "Tow-Placement Technology and Fabrication Issues for Laminated Composite Structures." In: Proceedings of the 46th AIAA/ASME/ASCE/AHS/ASC Structures, Structural Dynamics and Material (SDM) Conference, Austin, TX, April 18-21, 2005, Paper Number AIAA 2005-2017.

[17]Gürdal, Z., Tatting, B. F., and Wu., C. K., Variable stiffness composite panels: Effects of stiffness variation on the in-plane and buckling response. Composites Part A: Applied Science and Manufacturing 39(5), pp. 911-922. 2008.

[18]Nagendra, S., Kodiyalam, S., Davis, J., and Parthasarathy, V. "Optimization of Tow Fiber Paths for Composite Design." American Institute of Aeronautics and Astronautics, 1995. Structures, Structural Dynamics, and Materials and Co-Located Conferences.

[19]Tosh, Matthew William. "An Experimental and Numerical Investigation of Fibre Steering in Composite Structures." ProQuest, UMI Dissertations Publishing, 2000.
[20]Parnas, Levend, Oral and Ceyhan. "Optimum Design of Composite Structures with Curved Fiber Courses." Composites Science and Technology 63.7 (2003): 1071-82.
[21]Schueler, K., J. R. Miller, and R. Hale. "Approximate Geometric Methods in Application to the Modeling of Fiber Placed Composite Structures." Journal of Computing and Information Science in Engineering 4 (2004): 251-6. Print.
[22]Blom, Adriana W., Setoodeh, S., Hol, J.M.A.M, Gurdal, Z. "Design of Variable-Stiffness Conical Shells for Maximum Fundamental Eigenfrequency." Computers and Structures 86.9 (2008): 870-8.
[23]Blom, Adriana W., Tatting, B.F., Hol, M.A.M., Gurdal, Z. "Fiber Path Definitions for Elastically Tailored Conical Shells." Composites Part B 40.1 (2009): 77-84.
[24]Wu, Z., Weaver, P. M., Raju, G. and Kim, B. C. Buckling analysis and optimisation of variable angle tow composite plates. Thin-Walled Structures 60pp. 163. 2012.
[25]Alhajahmad, Ahmad, Mostafa M. Abdalla, and Zafer Gurdal. "Optimal Design of Tow-Placed Fuselage Panels for Maximum Strength with Buckling Considerations." Journal of Aircraft 47.3 (2010): 775-82.
[26]Honda, Shinya, Yoshihiro Narita, and Katsuhiko Sasaki. "Discrete Optimization for Vibration Design of Composite Plates by using Lamination Parameters." Advanced Composite Materials 18.4 (2009): 297-.
[27]H. Akhavan and P. Ribeiro. Natural modes of vibration of variable stiffness composite laminates with curvilinear fibers. Composite Structures 93(11), pp. 3040. 2011.
[28]Houmat, A., Nonlinear free vibration of laminated composite rectangular plates with curvilinear fibers. Composite Structures 106pp. 211-224. 2013.
[29]Houmat, A., Nonlinear free vibration analysis of variable stiffness symmetric skew laminates. *European Journal of Mechanics - A/Solids 50*pp. 70-75. 2015.
[30]Haddadpour, H., and Zamani, Z. “Curvilinear fiber optimization tools for aeroelastic design of composite wings”, J. Fluids Struct. 33pp. 180. 2012.
[31]Stodieck, O., Cooper, J. E., Weaver. J. E. and Kealy, P. Improved aeroelastic tailoring using tow-steered composites. Composite Structures 106pp. 703. 2013.
[32]"OpenVSP." http://www.openvsp.org/, 2012.
[33]Gloudemans, J., Davis, P. and Gelhausen, P. “A Rapid Geometry Modeler for Conceptual Aircraft," in Proceedings of the 34th Aerospace Sciences Meeting, no. January, (Reno, NV), 1996.
[34]Hahn, A. “Vehicle Sketch Pad: A Parametric Geometry Modeler for Conceptual Aircraft Design," in Proceedings of the 48th AIAA Aerospace Sciences Meeting, no. January, (Orlando, FL), 2010.
[35]Belben, J.B., “Enabling Rapid Conceptual Design Using Geometry-Based Multi-Fidelity Models In VSP”, M.S. Thesis, April, 2013.
[36]MATLAB 2014.0, The MathWorks, Inc., Natick, Massachusetts, United States.

## Appendix B.

## AIAA-2016-1975: Vibration and Buckling of Quadrilateral Variable Stiffness Laminated Composite Plates

# Vibration and Buckling of Quadrilateral Variable Stiffness Laminated Composite Plates

M C. Henson[1] and BP. Wang[2]

*Mechanical and Aerospace Engineering, University of Texas at Arlington, Arlington, TX, 76019*

## Abstract

**This paper presents vibration and buckling results for variable stiffness laminated composite panels having arbitrary quadrilateral shape. The Ritz method is used with Mindlin plate and lamination theory to develop solutions for variable stiffness panels. Straight fiber laminates with discretely varying stiffness are studied and compared with laminates having curvilinear fiber paths. Solutions are compared with finite element results.**

## Nomenclature

| | | |
|---|---|---|
| *AFP* | = | Advanced Fiber Placement |
| *VAT* | = | Variable Angle Tow |
| $x_i$,$y_i$ | = | plate corner point coordinates |
| $N_i$ | = | bilinear interpolation function |
| $\xi$, $\eta$ | = | natural coordinate system |
| $J$ | = | Jacobian matrix |
| $\Pi$ | = | potential energy |
| $A_{ij}$,$B_{ij}$,$D_{ij}$ | = | laminated plate stiffnesses |
| $\theta(x,y)$ | = | fiber orientation |
| $Q_{ij}^k$ | = | lamina stiffness matrix for kth layer |
| $u$, $v$, $w$ | = | displacement components |
| $\varepsilon_x$, $\varepsilon_y$, $\varepsilon_{xy}$ | = | strain components |
| $\kappa_x$, $\kappa_y$, $\kappa_{xy}$ | = | curvature components |
| $N_x$, $N_y$, $N_{xy}$ | = | stress resultants |
| $\{q\}$ | = | displacement vector |
| $B_i(x)$ | = | polynomial displacement function |
| $U_{ij}$ $V_{kl}W_{mn}$ | = | coefficents displacement functions |
| $N_p$ | = | order of polynomial basis function |
| $M_g$, $N_g$ | = | gauss integration points |

## I. Introduction

A key parameter in aircraft system performance is airframe weight. The directional properties of composite materials provide distinct advantages over metals in their ability to tailor aircraft structure for improved static and dynamic response at a reduced weight. Traditionally, straight-fiber laminated composites have been tailored by sizing the laminate into regions of constant thickness to meet the loads local to that region or zone. A 0-degree reference fiber direction is established for each part, commonly oriented in the principal load direction and assumed to remain constant. For each region, plies with the same fiber orientation, most often combinations of [0/+45/-45/90] ply angles, are summed together to calculate the percentage of fibers in each direction. The total thickness and ply percentages are then used to tailor the in-plane laminate stiffness and strength properties whereas the ply stacking sequence is used to tailor laminate bending properties.

[1] Graduate Student, Mechanical and Aerospace Engineering, Box 19023, Arlington, TX 76019, AIAA Senior Member.
[2] Professor, Mechanical and Aerospace Engineering, Box 19023, Arlington, TX 76019.

Plies are added or terminated to provide the stiffness and strength needed to sustain the loads in each zone, resulting in a laminate with regions of discretely varying properties. An example of this tailoring for a fighter aircraft wing skin is shown in **Figure 1**.

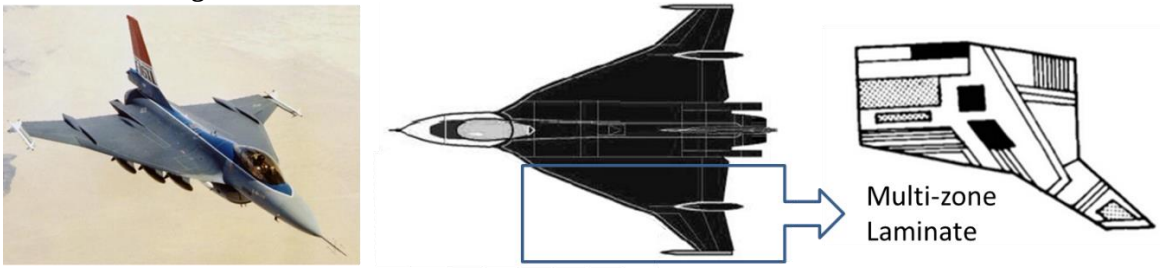


***Figure 1. Multi-zone Laminated Composite Tailoring of F-16XL Fighter Aircraft Wing Skin (Ref. 1).***

Variable stiffness laminates on the other hand possess stiffness properties that are a function of position and can be produced by continuously varying the ply fiber orientation. Automated Fiber Placement (AFP) has gained recognition for its ability to fabricate complex aircraft structure with improved precision and reduced cost. Current industry practice is to implement AFP much like the conventional hand layup process where fiber orientations are restricted to be constant within a given ply. However, fibers can also be steered in-plane and placed into a curvilinear orientation as shown in **Figure 2** to achieve variable stiffness, referred to as Variable Angle Tow (VAT) laminates.

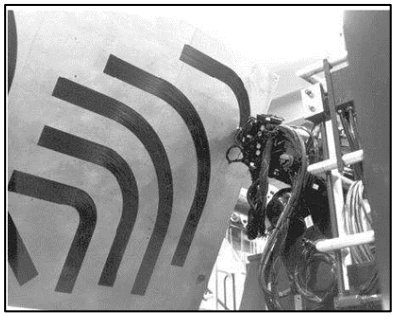

***Figure 2. AFP Curved Fiber Paths (Ref. 2).***

Researchers have demonstrated that fiber steering expands the design space by offering increased tailoring flexibility with improved performance and weight savings. Early work performed by Hyer et al. (Ref. 3 and 4) documented improvements that can be achieved in buckling performance with the use of curvilinear fiber orientations. Gurdal and Olmedo (Ref. 5) studied the in-plane elastic response of variable stiffness panels. Gurdal et al. (Ref. 6-8) investigated the design analysis and manufacturing of VAT laminates for maximum buckling performance. Extensive research has also been devoted to modeling and analysis of curvilinear fiber paths (Ref. 9-16). Vibration studies have been conducted in (Ref. 17-20) to demonstrate fundamental frequency improvements and aeroelastic optimization with curvilinear fibers has been conducted in Ref. 21and 22.

Tailoring of variable stiffness laminates however requires more complex engineering design and analysis methodologies. The objective of this work is to investigate the application of a general purpose Ritz procedure to enable design and analysis of VAT laminates for aircraft skin panels. The methodology has been applied to static, vibration and buckling analyses of rectangular, skew and quadrilateral panel geometries.

## II. Aircraft Panel Definition and Mapping

To facilitate design and analysis, aircraft skins are subdivided into panels based on arrangement of the underlying substructure as shown in **Figure 3**. The resulting skin panel geometries have arbitrary quadrilateral shape and are subject to a large number of in plane and transverse loading conditions.

The quadrilateral panel geometry is transformed from the physical ($x$-$y$) domain to a ($\xi$-$\eta$) computational domain as described by **Figure 4**. The transformation is accomplished using Eq. (*1*). $N_i$ are the bilinear Lagrangian interpolation functions used in the finite element method and $x_i$ and $y_i$ are the physical coordinates of the plate corner points. This makes it possible to select displacement basis functions with orthogonal properties and reduces the ($\xi$-$\eta$) computational domain to $[-1 \leq \xi, \eta \leq 1]$. It also facilitates mapping of fiber path orientations and simplifies application of boundary conditions.

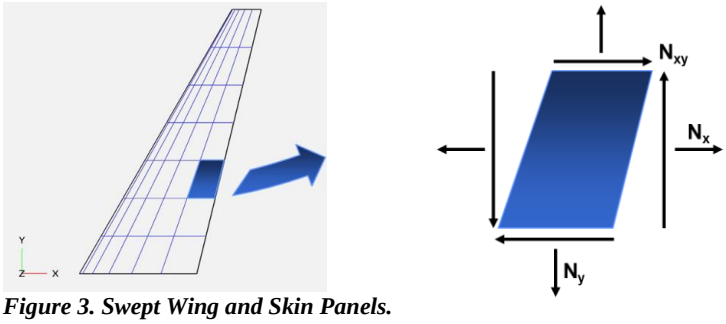


*Figure 3. Swept Wing and Skin Panels.*

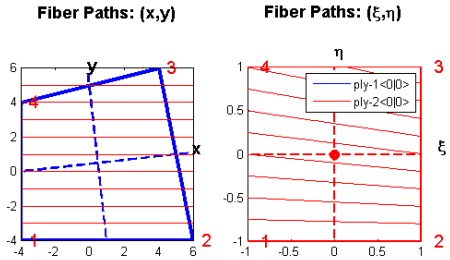


$$x(\xi,\eta) = \sum_{i=1}^{4} N_i(\xi,\eta)x_i$$
$$y(\xi,\eta) = \sum_{i=1}^{4} N_i(\xi,\eta)y_i \quad (1)$$

*Figure 4. Physical and computational domains.*

The Jacobian of this transformation is defined by Eq. (*2*) and is needed to transform panel strains into the natural coordinate system.

$$J = \begin{bmatrix} \frac{\partial x}{\partial \xi} & \frac{\partial y}{\partial \xi} \\ \frac{\partial x}{\partial \eta} & \frac{\partial y}{\partial \eta} \end{bmatrix}$$

$$\begin{aligned} \partial x/\partial \xi &= 1/4\,[(1+\eta)(x_3 - x_4) + (1-\eta)(x_2 - x_1)] \\ \partial y/\partial \xi &= 1/4\,[(1+\xi)(x_3 - x_2) + (1-\xi)(x_4 - x_1)] \\ \partial x/\partial \eta &= 1/4\,[(1+\eta)(y_3 - y_4) + (1-\eta)(y_2 - y_1)] \\ \partial y/\partial \eta &= 1/4\,[(1+\xi)(y_3 - y_2) + (1-\xi)(y_4 - y_1)] \end{aligned} \quad (2)$$

## III. Variable Stiffness Laminates

### A. Curvilinear Fiber Path Definition

The linear variable curvilinear fiber path introduced by Gurdal and Olmedo in Ref. 5 is chosen for this study. It has the advantages of offering a wide range of variable stiffness designs and provides closed form relations for the fiber path and steering radius of curvature. It assumes that a reference fiber angle drawn from the panel origin midpoint would vary linearly from a value $T_0$ to a value of $T_1$, at some characteristic distance (d) from the midpoint, usually taken as half the panel width. The fiber paths are also assumed to be anti-symmetric about the origin. The linear angle model was generalized by Tatting and Gurdal in Ref. 6 by rotating the axis of variation by an angle Ø as described by Eq. (*3*) and shown in **Figure 5**. This represents a single fiber reference path and would be the basis for generating all other courses. The established convention for describing variable angle laminates is of the form Ø< $T_0$ |$T_1$> and offers a wide range of freedom in describing tow-steered laminates.

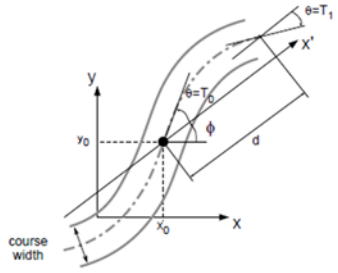


$$\theta(x') = \emptyset + (T_1 - T_0)\,\frac{|x'|}{d} + T_0 \quad (3)$$

*Figure 5. Linear variable fiber angle definition (Ref. 5).*

### B. Fiber Curvature Constraints

The ability to fabricate VAT laminates is constrained by the in-plane tow steering radius. If an individual tow of material is curved too much then it may buckle or develop defects as shown in **Figure 6**. The process is limited by the minimum steering radius of curvature required to avoid a tow buckling condition.

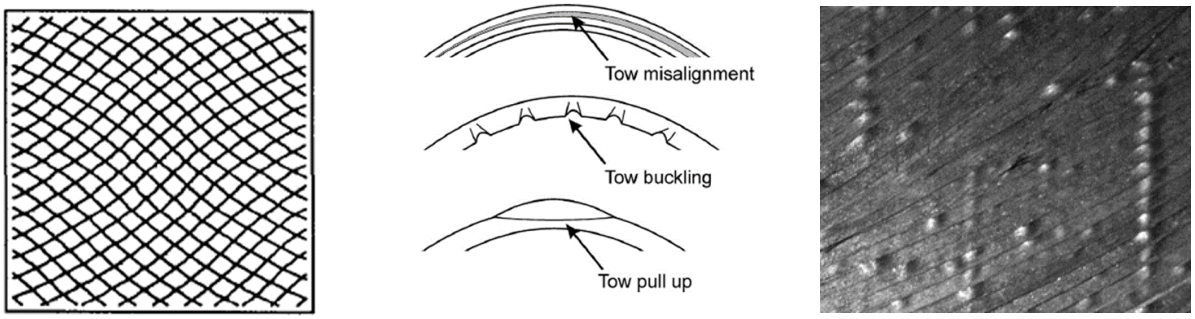


***Figure 6.Curvlinear Fiber Paths and Defects Arising from Tow Steering (Ref. 23 and 24).***

To avoid these conditions a constraint is defined as given in Ref. 19 and Ref. 20 for rectangular and skew panels.

$$\kappa_{path} = \frac{2}{a}(T_1 - T_0)cos\left[T_0 + \frac{2}{a}(T_1 - T_0)x\right] \tag{4}$$

$$\kappa_{skew\_path} = \frac{2}{bcos\phi_{skew}}cos\left[T_0 + \frac{2(T_1 - T_0)}{bcos\phi_{skew}}(T_1 - T_0)x\right] \quad 0 \le \acute{x} \le \frac{b}{2}cos\phi_{skew} \tag{5}$$

**Figure 7** shows the design space for a square panel $a = b = 20$ with an allowable steering radius of 12 inches which has been developed from Eq. (*4*).

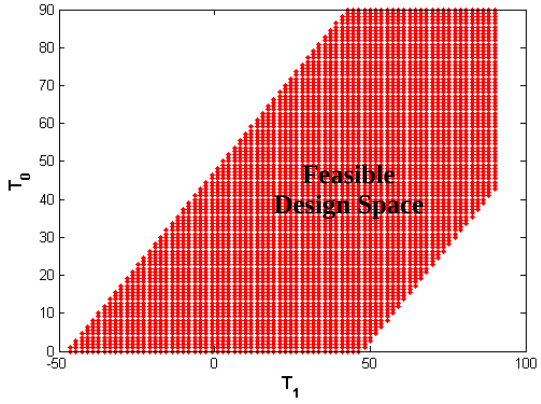


***Figure 7. Design Space for a ply of shifted curvilinear fibers (a=20in.).***

## IV. Analytical Approach

The analytical approach utilizes the Ritz method with high order displacement basis functions that provide solutions to static, free vibration and buckling eigenvalue problems. The basis functions are expressed in terms of a set of natural coordinates for a quadrilateral plate transformed from its rectangular Cartesian system. Using Eq. (*1*) the physical (*x-y*) quadrilateral domain is transformed to the (ξ-η) computational domain. The curvilinear fiber path model given by Eq. (*3*) is used to facilitate a linearly varying fiber orientation along the x or y panel axes. The Jacobian given by Eq. (*2*) is used to relate derivatives, fiber paths and boundary conditions between the two domains. Finally, variational methods are used to develop energy expressions for vibration, buckling stability and linear statics which are then solved using numerical integration.

### A. Displacements and Strains

The displacement field of the plate is given by Eq. (*6*) and (*7*).

$$\begin{aligned} u(x,y,z,t) &= u_0(x,y,t) + z\phi_x \\ v(x,y,z,t) &= v_0(x,y,t) + z\phi_y \\ w(x,y,z,t) &= w_0(x,y,t) \end{aligned} \tag{6}$$

$$\phi_x = \frac{\partial u}{\partial z}, \quad \phi_y = \frac{\partial v}{\partial z} \tag{7}$$

The strain-displacement relations are given by Eq. (*8*)

$$\begin{aligned} \varepsilon_x = \varepsilon_x^0 + z\kappa_x^0 &= \frac{\partial u_o}{\partial x} + z\frac{\partial \phi_x}{\partial x} \\ \varepsilon_y = \varepsilon_y^0 + z\kappa_y^0 &= \frac{\partial v_o}{\partial y} + z\frac{\partial \phi_y}{\partial y} \\ \varepsilon_z &= 0 \\ \gamma_{xy} = 2\varepsilon_{xy} = \gamma_{xy}^0 + z\kappa_{xy}^0 &= \left(\frac{\partial u_o}{\partial y} + \frac{\partial v_o}{\partial x}\right) + z\left(\frac{\partial \phi_x}{\partial y} + \frac{\partial \phi_y}{\partial x}\right) \\ \gamma_{yz} = 2\varepsilon_{yz} &= \frac{\partial v}{\partial z} + \frac{\partial w}{\partial y} = \phi_y + \frac{\partial w_0}{\partial y} \\ \gamma_{xz} = 2\varepsilon_{xz} &= \frac{\partial u}{\partial z} + \frac{\partial w}{\partial x} = \phi_x + \frac{\partial w_0}{\partial x} \end{aligned} \tag{8}$$

### C. Laminate Constitutive Relations

Variable stiffness laminates can be analyzed using constitutive relations based on classical lamination plate theory for thin laminates given by

$$\begin{Bmatrix} \sigma_{11} \\ \sigma_{22} \\ \tau_{12} \end{Bmatrix} = \begin{bmatrix} Q_{11} & Q_{11} & 0 \\ Q_{11} & Q_{11} & 0 \\ 0 & 0 & Q_{11} \end{bmatrix} \begin{Bmatrix} \varepsilon_{11} \\ \varepsilon_{22} \\ \varepsilon_{12} \end{Bmatrix} \tag{9}$$

where

$$\begin{aligned} Q_{11} &= E_1/(1-\nu_{12}\nu_{21}) \\ Q_{12} &= E_1\nu_{21}/(1-\nu_{12}\nu_{21}) \\ Q_{22} &= E_2/(1-\nu_{12}\nu_{21}) \\ Q_{66} &= G_{12} \\ \nu_{21} &= \nu_{12}\, E_2/E_1 \end{aligned} \tag{10}$$

Ply stress strain relations are given by

$$\begin{Bmatrix} \sigma_{xx} \\ \sigma_{yy} \\ \tau_{xy} \end{Bmatrix} = \begin{bmatrix} \bar{Q}_{11} & \bar{Q}_{11} & 0 \\ \bar{Q}_{11} & \bar{Q}_{11} & 0 \\ 0 & 0 & \bar{Q}_{11} \end{bmatrix} \begin{Bmatrix} \varepsilon_{11} \\ \varepsilon_{22} \\ \varepsilon_{12} \end{Bmatrix} \tag{11}$$

Ply stiffnesses will vary with $\theta(x,y)$

$$\begin{aligned} \bar{Q}_{11}(x,y) &= U_1 + U_2\cos[2\theta(x,y)] + U_3\cos[4\theta(x,y)] \\ \bar{Q}_{12}(x,y) &= U_4 - U_3\cos[4\theta(x,y)] \\ \bar{Q}_{22}(x,y) &= U_1 - U_2\cos[2\theta(x,y)] + U_3\cos[4\theta(x,y)] \\ \bar{Q}_{66}(x,y) &= U_5 - U_3\cos[4\theta(x,y)] \\ \bar{Q}_{16}(x,y) &= -1/2\, U_2\sin[2\theta(x,y)] - U_3\cos[4\theta(x,y)] \\ \bar{Q}_{26}(x,y) &= -1/2\, U_2\sin[2\theta(x,y)] + U_3\cos[4\theta(x,y)] \end{aligned} \tag{12}$$

Where the the laminate invariants are given by

$$\begin{aligned} U_1 &= (3Q_{11} + 3Q_{22} + 2Q_{12} + 4Q_{66})/8 \\ U_2 &= (Q_{11} + Q_{22})/2 \\ U_3 &= (Q_{11} + Q_{22} - 2Q_{12} - 4Q_{66})/8 \\ U_4 &= (Q_{11} + Q_{22} + 6Q_{12} - 4Q_{66})/8 \\ U_5 &= (Q_{11} + Q_{22} - 2Q_{12} + 4Q_{66})/8 \end{aligned} \tag{13}$$

## D. Energy Expressions

Based on Hamilton's principle, the stationary potential energy is given by Eq. (*14*).

$$\Pi = U + V + W - T = stationary\ value \tag{14}$$

where

$U = strain\ energy$ given by Eq. (*15*)
$V = potential\ energy\ of\ inplane\ loads\ due\ to\ inplane\ and\ bending\ deflections$ given by Eq. (*16*)
$W = potential\ energy\ of\ lateral\ loads\ p\ and\ P_l\ and\ bending\ deflections$ given by Eq. (*17*)
$T = kinetic\ energy\ of\ the\ plate$ given by Eq. (*18*)

$$U = \frac{1}{2}\iiint_V \{\sigma\}\{\varepsilon\}dV = \frac{1}{2}\iiint_V \{\varepsilon\}^T[D]\{\varepsilon\}dV \tag{15}$$

$$V = \oint_\Gamma \widehat{N}\cdot\bar{u}\,d\Gamma = \oint_\Gamma \left[\{N_x\hat{\imath} + N_y\hat{\jmath} + N_{xy}(\hat{\imath}+\hat{j})\}\cdot\{u_o\hat{\imath} + v_o\hat{\jmath})\}\right]d\Gamma \tag{16}$$

$$W = -\iint_A p\{w\}\,dxdy - \sum_l P_l\,w(x_l, y_l) \tag{17}$$

$$T = \frac{1}{2}\iiint_V \rho\bar{v}\,dV = \frac{1}{2}\iiint_V p\{\bar{v}\}^T\{\bar{v}\}dV \tag{18}$$

## E. Ritz Analysis Procedure

### *1. Ritz Basis Functions*

The Ritz method is used to obtain an approximate solution to the displacement field of Eq. (*6*) by using assumed series expressions to describe the plate mid-plane deformation given by Eq. (*19*). The $q_{ij}, q_{kl}, q_{mn}, q_{pq}, q_{rs}$ are unknown coefficients to be determined and the $B_{ij}, B_{kl}, B_{mn}, B_{pq}, B_{rs}$ basis functions are expressed in ξ-η.

$$\begin{aligned}
u_0 &= \{B_{IJ}\}^T\{q_U\} = \sum_{i=1}^{I}\sum_{j=1}^{J} B_{ij}(\xi,\eta)q_{ij}(t)\\
v_0 &= \{B_{KL}\}^T\{q_V\} = \sum_{k=1}^{K}\sum_{l=1}^{L} B_{kl}(\xi,\eta)q_{kl}(t)\\
w_0 &= \{B_{MN}\}^T\{q_W\} = \sum_{m=1}^{M}\sum_{n=1}^{N} B_{mn}(\xi,\eta)q_{mn}(t)\\
\phi_x &= \{B_{PQ}\}^T\{q_X\} = \sum_{p=1}^{P}\sum_{q=1}^{Q} B_{pq}(\xi,\eta)\,q_{pq}(t)\\
\phi_y &= \{B_{RS}\}^T\{q_Y\} = \sum_{r=1}^{R}\sum_{s=1}^{S} B_{rs}(\xi,\eta)q_{rs}(t)
\end{aligned} \tag{19}$$

This can be reduced to a more compact form

$$\begin{Bmatrix} u_0 \\ v_0 \\ w_0 \\ \phi_x \\ \phi_y \end{Bmatrix} = \left\{\{B_{IJ}\}^T, \{B_{KL}\}^T, \{B_{MN}\}^T, \{B_{PQ}\}^T, \{B_{RS}\}^T\right\}^T \begin{Bmatrix} q_U \\ q_V \\ q_W \\ q_X \\ q_Y \end{Bmatrix} = [B]^T\{q\} \tag{20}$$

The displacement vector $\{q\}$ is

$$\{q\} = \{\{q_U\}^T, \{q_V\}^T, \{q_W\}^T, \{q_X\}^T, \{q_Y\}^T\}^T \tag{21}$$

The Ritz basis vectors $\{B\}$ are given by

$$[B] = \left\{\{B_{IJ}\}^T, \{B_{KL}\}^T, \{B_{MN}\}^T, \{B_{PQ}\}^T, \{B_{RS}\}^T\right\}^T \tag{22}$$

*2. Legendre Polynomials*

Basis vectors $B_i(x)$ are chosen as Legendre polynomials given by Eq. (*23*) and shown in **Figure 1**.

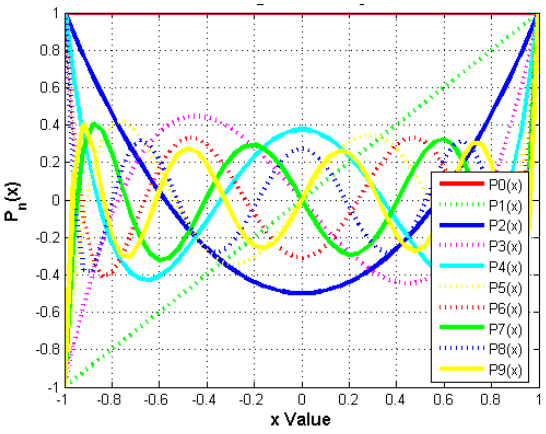


***Figure 8. First 10 Legendre Polynomials.***

$$B_{ij}(x,y) = B_i(x)B_j(y)$$

where

$$B_i(x) = P_{i-1}(x)$$

and

$$P_o(x) = 1$$
$$P_1(x) = x$$
$$P_{n+1}(x) = \frac{2n+1}{n+1}xP_n(x) - \frac{n}{n+1}P_{n-1}(x), n = 1, \ldots \quad (23)$$

*3. Strain Energy and Stiffness Matrix*

Substituting Eqs.(*6*) and (*7*) into Eq. (*15*) and integrating with respect to z for symmetric laminates, we obtain

$$U = \frac{1}{2}\iint_A \left[A_{11}{\varepsilon_x^0}^2 + 2A_{12}\varepsilon_x^0\varepsilon_y^0 + A_{22}{\varepsilon_y}^2 + 2\left(A_{16}\varepsilon_x^0 + A_{26}\varepsilon_y^0\right)\varepsilon_{xy}^0 + A_{66}{\varepsilon_{xy}^0}^2\right]dxdy$$
$$+ \frac{1}{2}\iint_A \left[D_{11}{\kappa_x^0}^2 + 2D_{12}\kappa_x^0\kappa_y^0 + D_{22}{\kappa_y^0}^2 + 4\left(D_{16}\kappa_x^0 + D_{26}\kappa_y^0\right)\kappa_{xy}^0 + 4D_{66}{\kappa_y^0}^2\right]dxdy \quad (24)$$

Plate stiffnesses (*A*,*B*,*D*) above vary with (x,y) position and are given by

$$\{A_{ij}, B_{ij}, D_{ij}\}(x,y) = \int_{-h/2}^{h/2}\bar{Q}_{ij}\{1, z, z^2\}\,dz = \sum_{k=1}^{N}\bar{Q}_{ij}(x,y)\{(h_k - h_{k-1}), \frac{1}{2}\left(h_k^2 - h_{k-1}^2\right), \frac{1}{3}\left(h_k^3 - h_{k-1}^3\right) \quad (25)$$

Strains are transformed to the (ξ-η) domain using the Jacobian relations

$$\begin{Bmatrix}\frac{\partial f}{\partial \xi}\\ \frac{\partial f}{\partial \eta}\end{Bmatrix} = \begin{bmatrix}\frac{\partial x}{\partial \xi} & \frac{\partial y}{\partial \xi}\\ \frac{\partial x}{\partial \eta} & \frac{\partial y}{\partial \eta}\end{bmatrix}\begin{Bmatrix}\frac{\partial f}{\partial x}\\ \frac{\partial f}{\partial y}\end{Bmatrix} = [J]\begin{Bmatrix}\frac{\partial f}{\partial x}\\ \frac{\partial f}{\partial y}\end{Bmatrix}$$
$$or \begin{Bmatrix}\frac{\partial f}{\partial x}\\ \frac{\partial f}{\partial y}\end{Bmatrix} = [J]^{-1}\begin{Bmatrix}\frac{\partial f}{\partial \xi}\\ \frac{\partial f}{\partial \eta}\end{Bmatrix}$$
$$where\ [\bar{J}] = [J]^{-1} = \frac{1}{|J|}\begin{bmatrix}J_{22} & -J_{12}\\ -J_{21} & J_{11}\end{bmatrix} = \begin{bmatrix}\bar{J}_{11} & \bar{J}_{12}\\ \bar{J}_{21} & \bar{J}_{21}\end{bmatrix} \quad (26)$$

The strain tensor is rewritten as

$$\{\varepsilon\} = \begin{Bmatrix}\varepsilon_x\\ \varepsilon_y\\ \varepsilon_{xy}\\ \varepsilon_{yz}\\ \varepsilon_{zx}\end{Bmatrix} = \begin{bmatrix}\bar{J}_{11} & \bar{J}_{12} & 0 & 0 & 0 & 0 & z\bar{J}_{11} & z\bar{J}_{12} & 0 & 0 & 0 & 0\\ 0 & 0 & \bar{J}_{21} & \bar{J}_{22} & 0 & 0 & 0 & 0 & z\bar{J}_{21} & z\bar{J}_{22} & 0 & 0\\ \bar{J}_{21} & \bar{J}_{22} & \bar{J}_{11} & \bar{J}_{12} & 0 & 0 & z\bar{J}_{21} & z\bar{J}_{22} & z\bar{J}_{11} & z\bar{J}_{12} & 0 & 0\\ 0 & 0 & 0 & 0 & \bar{J}_{21} & \bar{J}_{22} & 0 & 0 & 0 & 0 & 1 & 0\\ 0 & 0 & 0 & 0 & \bar{J}_{11} & \bar{J}_{12} & 0 & 0 & 0 & 0 & 0 & 1\end{bmatrix}\{\bar{\varepsilon}\} = [T_e]\{\bar{\varepsilon}\}$$

$$\{\bar{\varepsilon}\} = \begin{bmatrix}\frac{\partial u_o}{\partial \xi} & \frac{\partial u_o}{\partial \eta} & \frac{\partial v_o}{\partial \xi} & \frac{\partial v_o}{\partial \eta} & \frac{\partial w_o}{\partial \xi} & \frac{\partial w_o}{\partial \eta} & \frac{\partial \phi_x}{\partial \xi} & \frac{\partial \phi_x}{\partial \eta} & \frac{\partial \phi_y}{\partial \xi} & \frac{\partial \phi_y}{\partial \xi\eta} & \phi_x & \phi_y\end{bmatrix}^T \quad (27)$$

The strain energy can be written in matrix form as

$$U = \frac{1}{2}\iint_A [\{q\}^T[C]^T[T_e]^T[D][T_e][C]\{q\}\,|J|d\xi d\eta$$

$$U = \frac{1}{2}\{q\}^T[K_c]\{q\}$$

where

$$[K_c] = \iint_A [C]^T[T_e]^T[D][T_e][C]\,|J|d\xi d\eta \tag{28}$$

$$[K_c] \cong \sum_{i=1}^{M_g}\sum_{j=1}^{N_g} g_i\, g_j K_{mn}(\xi_i, \eta_j)$$

where

$$K_{mn} = [[C]^T[T_e]^T[D][T_e][C]|J|]_{(\xi_i,\eta_j)}$$

$$g_i, g_j = Gauss\ weights \tag{29}$$

and

$$[C] = \begin{bmatrix} [B_{IJ,\xi\eta}] & 0 & 0 & 0 & 0 \\ 0 & [B_{KL,\xi\eta}] & 0 & 0 & 0 \\ 0 & 0 & [B_{MN,\xi\eta}] & 0 & 0 \\ 0 & 0 & 0 & [B_{PQ,\xi\eta}] & 0 \\ 0 & 0 & 0 & 0 & [B_{RS,\xi\eta}] \\ 0 & 0 & 0 & \{B_{PQ}\}^T & 0 \\ 0 & 0 & 0 & 0 & \{B_{RS}\}^T \end{bmatrix} \tag{30}$$

*4. Kinetic Energy and Mass Matrix*

The velocity vector $\bar{v}$ described in Eq. (*18*) is given by

$$\{\bar{v}\} = \left\{\frac{\partial \bar{d}}{\partial t}\right\} = \begin{Bmatrix} \frac{\partial u_o}{\partial t} + z\frac{\partial \phi_x}{\partial t} \\ \frac{\partial v_o}{\partial t} + z\frac{\partial \phi_y}{\partial t} \\ \frac{\partial w_o}{\partial t} \end{Bmatrix} = \begin{bmatrix} 1 & 0 & 0 & z & 0 \\ 0 & 1 & 0 & 0 & z \\ 0 & 0 & 1 & 0 & 0 \end{bmatrix} \begin{Bmatrix} \frac{\partial u_o}{\partial t} \\ \frac{\partial v_o}{\partial t} \\ \frac{\partial w_o}{\partial t} \\ \frac{\partial \phi_x}{\partial t} \\ \frac{\partial \phi_y}{\partial t} \end{Bmatrix} = [Z][H]\{\dot{q}\}$$

Where $\{\bar{d}\}$ is the displacement vector

$$\{\bar{d}\} = \begin{Bmatrix} u \\ v \\ w \end{Bmatrix}, \qquad [\mathrm{Z}] = \begin{bmatrix} 1 & 0 & 0 & z & 0 \\ 0 & 1 & 0 & 0 & z \\ 0 & 0 & 1 & 0 & 0 \end{bmatrix}$$

$$[H] = \begin{bmatrix} \{B_{IJ}\}^T & 0 & 0 & 0 & 0 \\ 0 & \{B_{KL}\}^T & 0 & 0 & 0 \\ 0 & 0 & \{B_{MN}\}^T & 0 & 0 \\ 0 & 0 & 0 & \{B_{PQ}\}^T & 0 \\ 0 & 0 & 0 & 0 & \{B_{RS}\}^T \end{bmatrix} \tag{31}$$

The kinetic energy can be rewritten as

$$T = \frac{1}{2}\iiint_V p\{\dot{q}\}^T[Z]^T[H]^T[Z][H]\{\dot{q}\}dV$$

In matrix form

$$T = \frac{1}{2}\{\dot{q}\}^T[M_c]\{\dot{q}\}$$

The mass matrix $[M_c]$ is

$$[M_c] \cong \sum_{i=1}^{M_g}\sum_{j=1}^{N_g} g_i\, g_j M_{mn}$$

$$M_{mn} = \int_{-h/2}^{h/2} [\rho[Z]^T[H]^T[Z][H]dz]\,|J|d\xi d\eta \tag{32}$$

*5. Potential Energy of External Loads Due to In-plane Deflections*

Equation (*16*) is used to write the potential energy expression for external loads due to in-plane deflections

$$V_i = \oint_\Gamma [N_x \quad N_y \quad N_{xy}][u_o \quad v_o \quad (u_o + v_o)]^T\, d\Gamma \tag{33}$$

We can rewrite in matrix form as

$$V_i = \{F_c\}^T\{q\}$$

$$\{F_c\} = \oint_\Gamma \{N\}[d_i]\, d\Gamma$$

where $[d_i]$ = in-plane displacement vector

$$[d_i] = \begin{bmatrix}\{B_{IJ}\}^T & \{B_{KL}\}^T & 0 & 0 & 0\end{bmatrix}$$

Introducing numerical integration

$$\{F_c\} = \sum_{i=1}^{4}\sum_{j=1}^{M_g} g_j\, f_j(\xi_\Gamma, \eta_\Gamma)$$

$$f_j(\xi_\Gamma, \eta_\Gamma) = \oint_{\Gamma_i} \left[\{N\}[d_i]\right]_{(\xi_\Gamma,\eta_\Gamma)}\, d\Gamma \tag{34}$$

*6. Potential Energy of External Loads Due to Bending Deflections*

The potential energy of in-plane loads associated with bending deflections can be written as

$$V_b = \lambda \iint_A \left[N_x\varepsilon_x^b + N_y\varepsilon_y^b + N_{xy}\varepsilon_{xy}^b\right] dxdy$$

$$= \frac{1}{2}\lambda \iint_A N_x w_{,x}^2 + N_y w_{,y}^2 + N_{xy}w_{,x}w_{,y}]dxdy$$

$$= \frac{1}{2}\lambda \iint_A \{q\}^T[C]^T[T_b]^T\{N\}^T[T_b][C]\{q\}\,|J|d\xi d\eta \tag{35}$$

where $\lambda$ is the buckling load factor and $\varepsilon_x^b,\ \varepsilon_y^b, \varepsilon_{xy}^b$ are bending strains induced by the in-plane stress resultants $N_x, N_y, N_{xy}$.

Using Eqs. (*19*),(*20*),(*21*) and introducing numerical integration we can write

$$V_b = \frac{1}{2}\lambda\{q\}^T[G_c]\{q\}$$

where geometric stiffness matrix $[G_c]$ is

$$[G_c] \cong \sum_{i=1}^{M_g}\sum_{j=1}^{N_g} g_i\, g_j G_{mn}$$

and

$$G_{mn} = [C]^T[T_b]^T\{N\}^T[T_b][C]|J|_{(\xi_i,\eta_j)} \tag{36}$$

and

$$[T_b] = \begin{bmatrix} 0 & 0 & 0 & 0 & \bar{J}_{11} & \bar{J}_{12} & 0 & 0 & 0 & 0 & 0 & 0 \\ 0 & 0 & 0 & 0 & \bar{J}_{21} & \bar{J}_{22} & 0 & 0 & 0 & 0 & 0 & 0 \\ 0 & 0 & 0 & 0 & \bar{J}_{11}+\bar{J}_{21} & \bar{J}_{12}+\bar{J}_{22} & 0 & 0 & 0 & 0 & 0 & 0 \\ 0 & 0 & 0 & 0 & 0 & 0 & 0 & 0 & 0 & 0 & 1 & 0 \\ 0 & 0 & 0 & 0 & 0 & 0 & 0 & 0 & 0 & 0 & 0 & 1 \end{bmatrix} \tag{37}$$

*7. Potential Energy of External Transverse Loads*

The work $W$ given by Eq. (*17*) due to a uniform transverse load $p_o$ and point loads $P_l$ can be expressed as

$$W = \iint_A p_o\{q_W\}\,dxdy + \sum_l P_l\,\{q_W\}$$

$$W = \{P_c\} = \{P_0\} + \{P_L\}$$

$$\{P_o\} = \iint_A p_o[d_t]^T\{q\}|J|d\xi d\eta$$

$$\{P_L\} = \sum_l P_l\,[d_t]^T\{q\}|_{(\xi_l,\eta_l)}$$

$$[d_t] = [0 \quad 0 \quad \{B_{MN}\}^T \quad 0 \quad 0]$$

Using numerical integration

$$\{P_o\} \cong \sum_{i=1}^{M_g}\sum_{j=1}^{N_g} g_i\, g_j p_o[d_t] \tag{38}$$

*8. Boundary Conditions: Null Space Approach*

Boundary conditions include combinations of simple, clamped or free displacement conditions along plate edges. To simplify their specification for a generalized quadrilateral geometry, they are applied in the (ξ-η) computational domain given by Eq.(*39*).

$$\begin{aligned} u &= 0 \\ w &= 0 \\ w &= 0 \\ \phi_x &= 0 \\ \phi_y &= 0 \end{aligned} \tag{39}$$

The basis functions do not satisfy these conditions and must be enforced in a more general way. Eq.(*39*) can be written in matrix form for fully clamped conditions as

$$[A]\{q\} = 0$$

or

$$[A]\{q\} = \begin{Bmatrix} u|_{\xi=-1} \\ v|_{\xi=-1} \\ w|_{\xi=-1} \\ \phi_x|_{\xi=-1} \\ \phi_y|_{\xi=-1} \\ \cdots \end{Bmatrix}\{q\} = 0 \tag{40}$$

Eq. (*40*) indicates the coeffients $\{q\}$ are not linearly independent. A set of linearly independent coordinates $\{\bar{q}\}$ are defined such that

$$\{\bar{q}\} = [T]\{q\} \tag{41}$$

Here $[T]$ is a unknown transformation matrix. Substituting Eq. (*41*) into Eq. (*40*) gives

$$[A][T]\{\bar{q}\} = \{0\} \tag{42}$$

Since $\{q\}$ is a set of independent coordinates, it follows that

$$[A][T] = [0] \tag{43}$$

Thus $[T]$ is the null space of matrix $[A]$, or

$$[T] = null(A) \tag{44}$$

The energy expressions can now be expressed in terms of the fully generalized, linearly independent coordinates $\{\bar{q}\}$. The strain energy is written as

$$U = \frac{1}{2}\{\bar{q}\}^T[T]^T[K_c][T]\{\bar{q}\} = \frac{1}{2}\{\bar{q}\}^T\left[K_{\bar{q}}\right]\{\bar{q}\}$$

where

$$\left[K_{\bar{q}}\right] = [T]^T[K_c][T] \tag{45}$$

The kinetic energy is written as

$$T = \frac{1}{2}\{\dot{\bar{q}}\}[T]^T[M_c][T]\{\dot{\bar{q}}\} = \frac{1}{2}\{\dot{\bar{q}}\}\left[M_{\bar{q}}\right]\{\dot{\bar{q}}\}$$

where

$$\left[M_{\bar{q}}\right] = [T]^T[M_c][T] \tag{46}$$

Similarly, the potential energy terms can be written as

$$V_i = \{F_c\}^T[T]\{\bar{q}\} = \left\{F_{\bar{q}}\right\}^T\{\bar{q}\} \tag{47}$$

$$V_b = \frac{1}{2}\lambda\{\bar{q}\}^T[T]^T[G_c]\{\bar{q}\} = \frac{1}{2}\lambda\{\bar{q}\}^T\left[G_{\bar{q}}\right]\{\bar{q}\} \tag{48}$$

$$W = \{P_c\}[T]\{q\} = \left\{P_{\bar{q}}\right\}^T\{\bar{q}\} \tag{49}$$

*9. Analysis Problems*

The free vibration eigenvalue problem is formulated from Eq. (*14*) and taking the stationary value

$$\frac{\partial \Pi}{\partial(B_{IJ}, B_{KL}, B_{MN}, B_{PQ}, B_{RS})} = \frac{\partial(T-U)}{\partial(B_{IJ}, B_{KL}, B_{MN}, B_{PQ}, B_{RS})} = 0 \tag{50}$$

This process gives a set of linear simultaneous equations in terms of the unknown coefficients$B_{IJ}, B_{KL}, B_{MN}, B_{PQ}, B_{RS}$. The natural frequencies and mode shapes for the plate are obtained by solving

$$[K - \lambda M]\{q\} = 0 \tag{51}$$

Similarly, the buckling eigenvalue problem is formulated from Eq. (*14*) and taking the stationary value

$$\frac{\partial \Pi}{\partial(B_{IJ}, B_{KL}, B_{MN}, B_{PQ}, B_{RS})} = \frac{\partial(U - V)}{\partial(B_{IJ}, B_{KL}, B_{MN}, B_{PQ}, B_{RS})} = 0 \tag{52}$$

Buckling load factors and mode shapes for the plate are obtained by solving

$$[K - \lambda G]\{q\} = 0 \tag{53}$$

The static analysis problem is formulated from Eq. (*14*) and taking the stationary value

$$\frac{\partial \Pi}{\partial(B_{IJ}, B_{KL}, B_{MN}, B_{PQ}, B_{RS})} = \frac{\partial(U + W)}{\partial(B_{IJ}, B_{KL}, B_{MN}, B_{PQ}, B_{RS})} = 0 \tag{54}$$

The displacement vector is obtained by solving

$$[K]\{q\} = \{F\} \tag{55}$$

## V. Numerical Results

Numerical solutions were implemented using the MATLAB software (Ref. 25). Results were generated for vibration, buckling and static analyses. A summary of the problems investigated is provided in **Table 1**

***Table 1.Summary of Analyses***

| Case | Analysis | Panel Geometry | Loads | BCs | Laminate | Study Parameter |
|---|---|---|---|---|---|---|
| 1 | Vibration | a=b=10 | - | CFFF | QI | $N_p$ |
| 2 | Vibration | ”” | - | CFFF | $VAT^1$ | $M_g$ |
| 3 | Vibration | ”” | - | SSSS, CCCC, CFFF | $VAT^1$ | $\lambda_{Ritz}/\lambda_{FEM}$ |
| 4 | Buckling | ”” | $N_x$=-100 lb/in | SSSS, CCCC, CFFF | QI, AP, $VAT^1$,$VAT^2$,$VAT^3$ | $\lambda_{Ritz}/\lambda_{FEM}$ |
| 5 | Static | ”” | $p_0$=-0.025psi | CFFF | $VAT^1$ | Deflection, strain |
| 6 | Static | ”” | $N_{xy}$=100 lb/in | CFFF | $VAT^1$ | Deflection, strain |
| 7 | Vibration | Skew a=b=10 | - | SSSS, CCCC, CFFF | $VAT^1$ | Panel Skew |
| 8 | Vibration | Quadrilateral | - | SSSS, CCCC, CFFF | QI, AP, $VAT^1$,$VAT^2$,$VAT^3$ | Geometry |
| 9 | Buckling | ”” | $N_x$=-100; $N_y$=-10 | SSSS, CCCC, CFFF | QI, AP, $VAT^1$,$VAT^2$,$VAT^3$ | Geometry |
| 10 | Static | ”” | $p_0$=-0.025psi | SSSS | QI, AP, $VAT^1$,$VAT^2$,$VAT^3$ | Deflection, strain |

Laminate definitions used for this study are given in **Table 2** and material properties are given in **Table 3**. The VAT laminates were selected from Ref. 8 and 19.

***Table 2.Laminate descriptions***

| Laminate | Stacking Sequence | $N_{plys}$ |
|---|---|---|
| QI | $[0/+45/-45/90]_S$ | 8 |
| AP | $[+45/-45/+45/-45]_S$ | 8 |
| $VAT^1$ | $[<-45\|45>,<45\|-45>]_{2S}$ | 8 |
| $VAT^2$ | $[<0\|45>,<0\|-45>]_{2S}$ | 8 |
| $VAT^3$ | $[90<0\|45>,90<0\|-45>]_{2S}$ | 8 |

***Table 3. Lamina Mechanical Properties***

| $E_1$(Msi) | $E_2$(Msi) | $G_{12}$(Msi) | $\nu_{12}$ | $\rho$(lb/in$^3$) | $t_{ply}$(in) |
|---|---|---|---|---|---|
| 22.15 | 1.38 | 0.86 | 0.321 | 0.058 | .0053 |

The distribution of effective engineering laminate stiffnesses as a function of panel position are presented in **Figure 9** through **Figure 11**. This serves to illustrate the degree of property tailoring offered by variable fiber path laminates. The $VAT^1$ laminate has two regions near the panel edges where the stiffness is maximized. The $VAT^2$ laminate is designed to achieve maximum $E_x$ stiffness in the middle of the panel, whereas the $VAT^3$ laminate is designed to achieve a maximum $E_y$ stiffness in the middle of the panel.

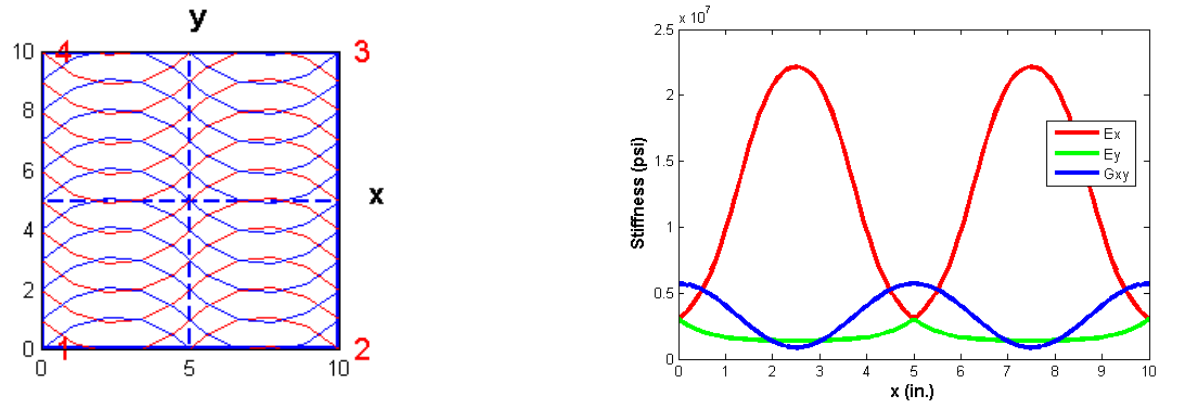


***Figure 9. Fiber Paths and Laminate Engineering Constants for VAT[1] Laminate.***

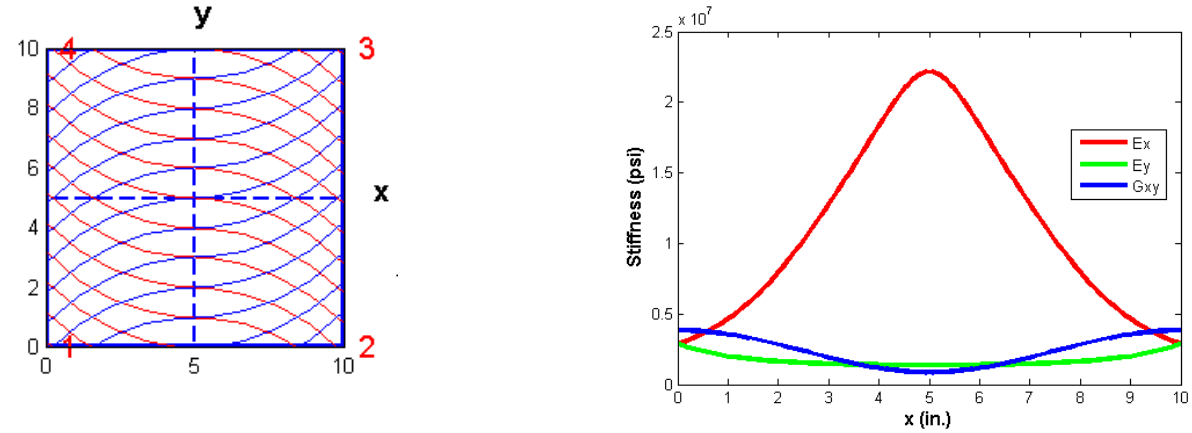


***Figure 10. Fiber Paths and Laminate Engineering Constants for VAT[2] Laminate.***

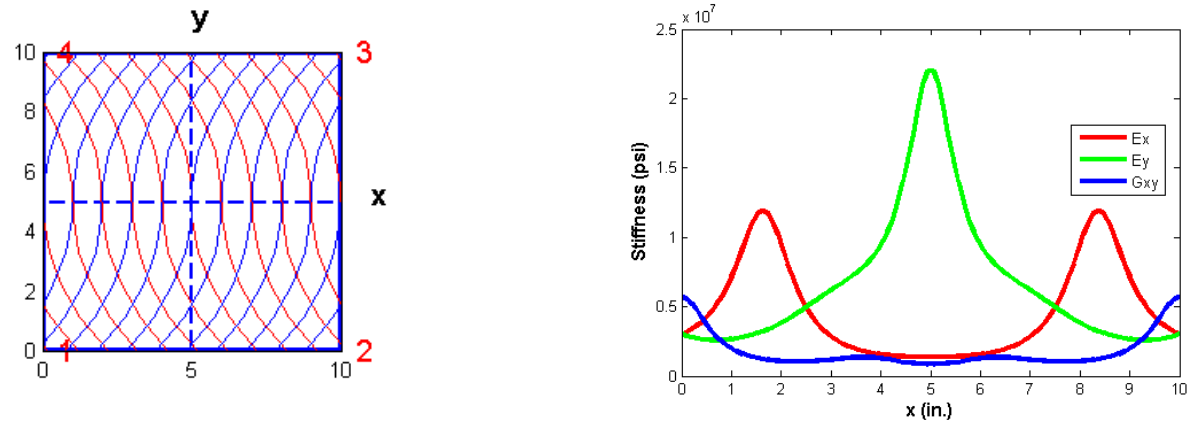


***Figure 11. Fiber Paths and Laminate Engineering Constants for VAT[3] Laminate.***

## A. Numerical Solution

The analysis problems were solved using Gaussian quadrature numerical integration to evaluate the integral energy expressions. The integrals are evaluated in the (ξ-η) computational domain at gauss points. Boundary conditions are evaluated by creating a uniform grid of points in the physical domain and transforming them to the (ξ-η) domain. Results are recovered in the physical x-y domain to evaluate eigenvalues, mode shapes, deflections and strains.

## B. Convergence

Convergence of the vibration solution was investigated by examining natural frequencies for the first 15 modes of a cantilevered QI laminated plate as shown in **Figure 12**. The first 5 eigenvalues converged at a polynomial order of $N_p = 5$ and all fifteen frequencies were converged by order $N_p = 9$. Convergence was also studied on the integration order to determine the minimum number of Gauss points required to capture behavior of a cantilevered VAT[1] laminate. **Figure 13** shows the results are generally insensitive to integration order beyond $M_g = 10$. A value of $M_g = 20$ was used for all subsequent studies.

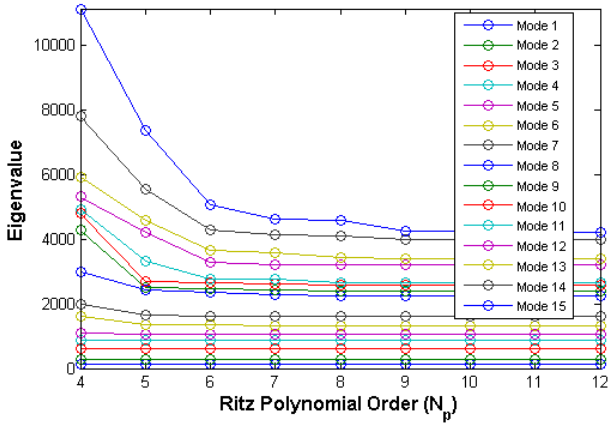


**Figure 12. Eigenvalue convergence as function of Np.**

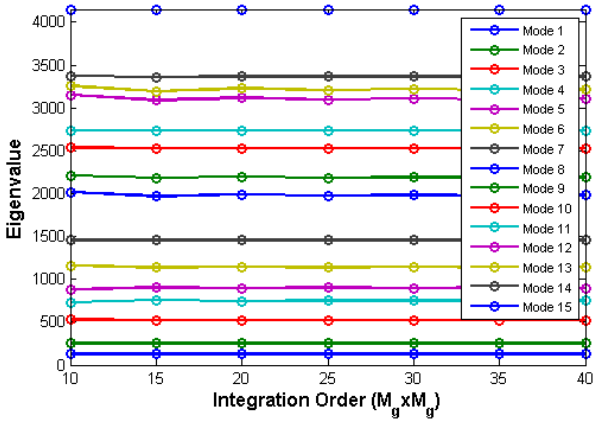


**Figure 13. Eigenvalue convergence for Mg.**

## C. Model Verification

The Ritz analysis model was verified using Nastran finite element analyses. Free vibration results are given in **Table 4** and **Figure 14** for a square VAT[1] laminate with three boundary condition cases of SSSS, CCCC and CFFF.

***Table 4. VAT[1] Free Vibration Eigenvalue Ratios.***

| Mode | Ratio: $\lambda_{Ritz}/\lambda_{FEM}$ | | |
|---|---|---|---|
| | SSSS | CCCC | CFFF |
| 1 | 1.005 | 1.004 | 0.996 |
| 2 | 1.018 | 1.021 | 1.003 |
| 3 | 1.024 | 1.027 | 1.015 |
| 4 | 1.009 | 1.003 | 0.995 |
| 5 | 1.017 | 1.014 | 1.009 |
| 6 | 1.026 | 1.028 | 1.020 |
| 7 | 1.024 | 1.026 | 1.015 |
| 8 | 1.005 | 0.998 | 1.030 |
| 9 | 1.028 | 1.032 | 1.028 |
| 10 | 1.016 | 1.028 | 1.009 |
| 11 | 1.028 | 1.011 | 1.013 |
| 12 | 1.029 | 1.038 | 1.039 |
| 13 | 1.035 | 1.029 | 1.035 |
| 14 | 1.035 | 1.050 | 1.020 |
| 15 | 1.029 | 1.044 | 1.035 |

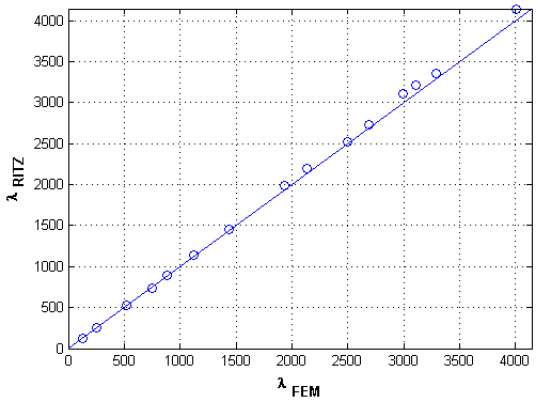


***Figure 14. Vibration Eigenvalues for CFFF VAT[1] Laminate.***

The Ritz buckling solution was verified by analysis of square plate laminates as described in Case 4. Buckling factor results are given in **Table 5** for the $N_x$ load cases and in for the $N_y$ cases. The Ritz $N_x$ solutions agrees within 3% of the FEM results with exception of the fully clamped cases and the simply supported angle ply laminate. The $N_y$ cases generally produced the same trends as Nx loading but with larger errors.

***Table 5. Ritz and FEM $N_x$ Buckling Factor Comparison.***

| Laminate | BC | Buckling Factor | | Ratio | % Error |
|---|---|---|---|---|---|
| | | Ritz | FEM | | |
| VAT1 | SSSS | 0.470 | 0.460 | 1.021 | 2.13 |
| VAT1 | CCCC | 0.697 | 0.758 | 0.920 | -7.97 |
| VAT1 | CFFF | 0.141 | 0.142 | 0.995 | -0.51 |
| VAT2 | SSSS | 0.507 | 0.520 | 0.974 | -2.61 |
| VAT2 | CCCC | 0.714 | 0.840 | 0.850 | -14.99 |
| VAT2 | CFFF | 0.143 | 0.143 | 1.000 | 0.03 |
| VAT3 | SSSS | 0.417 | 0.413 | 1.008 | 0.78 |
| VAT3 | CCCC | 0.562 | 0.954 | 0.589 | -41.11 |
| VAT3 | CFFF | 0.069 | 0.068 | 1.001 | 0.09 |
| QI | SSSS | 0.469 | 0.464 | 1.011 | 1.08 |
| QI | CCCC | 0.777 | 0.976 | 0.796 | -20.37 |
| QI | CFFF | 0.154 | 0.154 | 1.000 | -0.05 |
| AP | SSSS | 0.530 | 0.493 | 1.075 | 7.49 |
| AP | CCCC | 0.745 | 0.977 | 0.762 | -23.81 |
| AP | CFFF | 0.091 | 0.091 | 0.999 | -0.12 |

***Table 6. Ritz and Fem $N_y$ Buckling Factor Comparison.***

| Laminate | BC | Buckling Factor | | Ratio | % Error |
|---|---|---|---|---|---|
| | | Ritz | FEM | | |
| VAT1 | SSSS | 1.516 | 1.419 | 1.069 | 6.85 |
| VAT1 | CCCC | 0.800 | 0.879 | 0.909 | -9.05 |
| VAT1 | CFFF | 0.213 | 0.195 | 1.092 | 9.23 |
| VAT2 | SSSS | 1.486 | 1.548 | 0.960 | -3.98 |
| VAT2 | CCCC | 1.826 | 3.105 | 0.588 | -41.18 |
| VAT2 | CFFF | 0.205 | 0.191 | 1.070 | 6.97 |
| VAT3 | SSSS | 1.577 | 1.263 | 1.248 | 24.79 |
| VAT3 | CCCC | 2.732 | 2.829 | 0.966 | -3.43 |
| VAT3 | CFFF | 0.441 | 0.427 | 1.032 | 3.19 |
| QI | SSSS | 1.588 | 1.511 | 1.051 | 5.11 |
| QI | CCCC | 2.260 | 2.762 | 0.818 | -18.16 |
| QI | CFFF | 0.584 | 0.730 | 0.800 | -19.96 |
| AP | SSSS | 1.836 | 1.637 | 1.121 | 12.11 |
| AP | CCCC | 2.635 | 3.293 | 0.800 | -19.98 |
| AP | CFFF | 0.331 | 0.310 | 1.069 | 6.90 |

The Ritz static solution was verified by analysis of a plate bending problem (Case 5) and an in-plane bending problem (Case 6). The results are presented graphically in **Figure 15** and **Figure 16**. The Ritz deflection and strain profiles track closely with the FEM for the plate bending case. The max deflection is within 0.5% and the max bending strain is within 12%. It is expected that a more refined FEM mesh would improve this agreement.

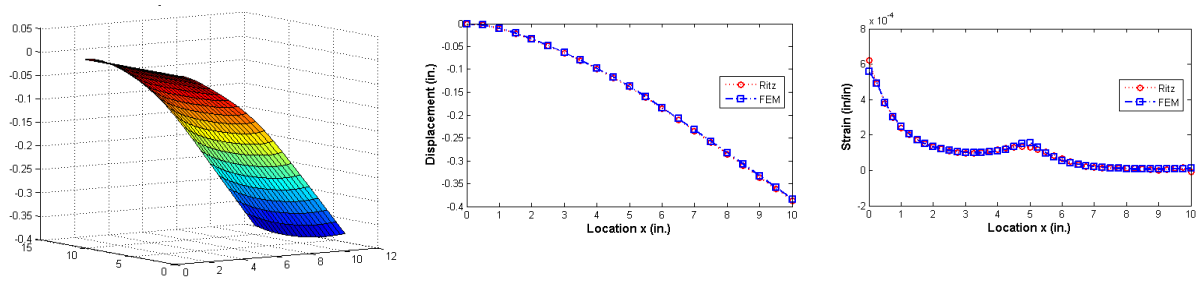


***Figure 15. Case 5 Deflected Shape and Profiles of Deflection and Top Fiber Strain $\varepsilon_x$ at Midspan Section y=0.***

The in-plane bending deflection results from Case 6 (**Figure 16**) lie within 3% of the FEM. The in-plane shear strain $\varepsilon_{xy}$ profile is consistent with the FEM but does not exhibit the same peak strain values.

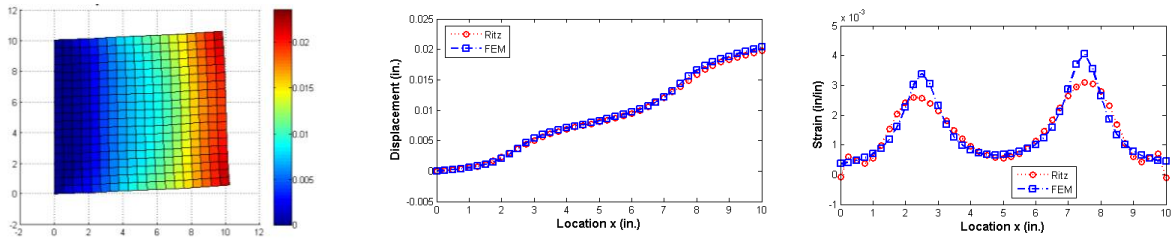


***Figure 16. Midspan Deflections and Shear Strain $\varepsilon_{xy}$ for Case 6.***

## D. Skew and Quadrilateral Panel Results

The behavior of skew and quadrilateral panels was studied for Cases 7 through 10. **Table 7** shows Ritz and FEM free vibration results for a skewed VAT laminate with boundary conditions of SSSS, CCCC and CFFF and a range of plate skew angles $\phi_{skew} = 0\ to\ 60$ degrees. The agreement here is very good. Typical results are shown for a cantilevered plate in **Figure 17**.

***Table 7. Vibration Eigenvalue Ratios for Skewed Laminate.***

| $\phi_{skew}$ | BC | Ratio: $\lambda_{Ritz}/\lambda_{FEM}$ Mode | | | | |
|---|---|---|---|---|---|---|
| | | 1 | 2 | 3 | 4 | 5 |
| 15 | SSSS | 1.005 | 1.018 | 1.024 | 1.009 | 1.017 |
| 30 | SSSS | 1.006 | 1.017 | 1.022 | 1.009 | 1.017 |
| 45 | SSSS | 1.008 | 1.015 | 1.013 | 1.011 | 1.016 |
| 60 | SSSS | 1.013 | 1.013 | 1.009 | 1.012 | 1.009 |
| | | | | | | |
| 15 | CCCC | 1.004 | 1.021 | 1.027 | 1.003 | 1.014 |
| 30 | CCCC | 1.004 | 1.020 | 1.025 | 1.003 | 1.016 |
| 45 | CCCC | 1.006 | 1.017 | 1.019 | 1.006 | 1.016 |
| 60 | CCCC | 1.008 | 1.013 | 1.012 | 1.010 | 1.016 |
| | | | | | | |
| 15 | CFFF | 0.996 | 1.003 | 1.015 | 0.995 | 1.009 |
| 30 | CFFF | 0.997 | 1.003 | 1.014 | 0.996 | 1.009 |
| 45 | CFFF | 1.000 | 1.002 | 1.013 | 1.002 | 1.008 |
| 60 | CFFF | 1.002 | 1.003 | 1.010 | 1.007 | 1.009 |

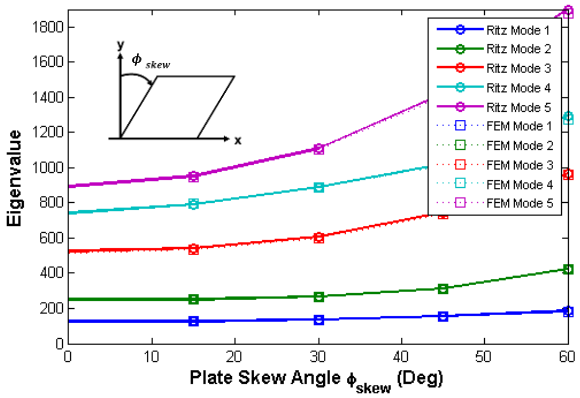


***Figure 17. Eigenvalue for Skewed CFFF VAT[1] Laminate***

The quadrilateral plate geometry is shown in **Figure 18**. Free vibration results are given in **Table 8** for the first vibration mode. The Ritz solution shows good agreement with FEM results with errors of less than 10% for all laminates and boundary conditions.

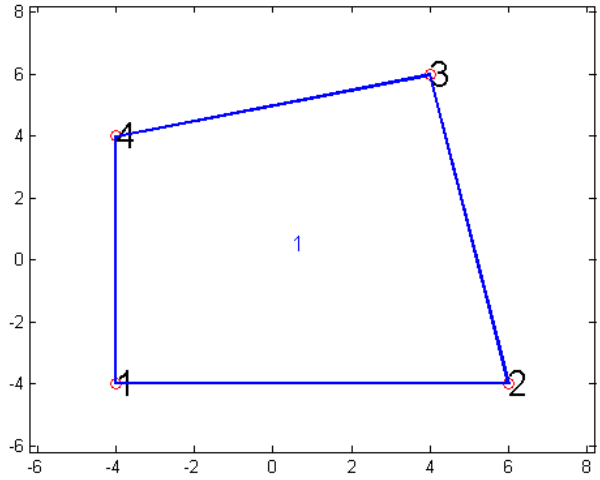


**Figure 18. Quadrilateral Plate Geometry.**

***Table 8. Free Vibration Results for Quadrilateral Panel.***

| Laminate | BC | First Mode Eigenvalue | | |
|---|---|---|---|---|
| | | Ritz | FEM | %Error |
| VAT1 | SSSS | 707 | 714 | -0.96 |
| VAT1 | CCCC | 1201 | 1178 | 1.97 |
| VAT1 | CFFF | 144 | 141 | 1.51 |
| | | | | |
| VAT2 | SSSS | 760 | 763 | -0.45 |
| VAT2 | CCCC | 1209 | 1185 | -9.05 |
| VAT2 | CFFF | 134 | 129 | 6.85 |
| | | | | |
| VAT3 | SSSS | 688 | 680 | 1.08 |
| VAT3 | CCCC | 1364 | 1386 | 2.10 |
| VAT3 | CFFF | 83 | 80 | 3.97 |
| | | | | |
| QI | SSSS | 799 | 805 | -0.70 |
| QI | CCCC | 1320 | 1301 | 1.45 |
| QI | CFFF | 96 | 96 | 0.14 |
| | | | | |
| AP | SSSS | 725 | 713 | 1.60 |
| AP | CCCC | 1355 | 1340 | 1.09 |
| AP | CFFF | 156 | 152 | 2.75 |

Buckling factor results for the quadrilateral plate are given in **Table 9** and **Table 10**. The Ritz and FEM generally results agree within 10% for the Nx loading. Similar to the square plate results, the $N_y$ cases also produced the same trends as Nx loading but have larger disagreement with the FEM.

***Table 9. $N_x$ Buckling Factors for Quadrilateral Panels.***

| Laminate | BC | Buckling Factor | | % Error |
|---|---|---|---|---|
| | | Ritz | FEM | |
| VAT1 | SSSS | 0.513 | 0.490 | 4.60 |
| VAT1 | CCCC | 0.788 | 0.798 | -1.21 |
| VAT1 | CFFF | 0.148 | 0.144 | 2.54 |
| VAT2 | SSSS | 0.549 | 0.545 | 0.76 |
| VAT2 | CCCC | 0.800 | 0.879 | -9.05 |
| VAT2 | CFFF | 0.151 | 0.142 | 6.85 |
| VAT3 | SSSS | 0.445 | 0.422 | 5.55 |
| VAT3 | CCCC | 0.632 | 0.945 | -33.19 |
| VAT3 | CFFF | 0.075 | 0.070 | 6.86 |
| QI | SSSS | 0.524 | 0.484 | 8.43 |
| QI | CCCC | 0.863 | 1.021 | -15.48 |
| QI | CFFF | 0.163 | 0.155 | 5.33 |
| AP | SSSS | 0.568 | 0.513 | 10.55 |
| AP | CCCC | 0.812 | 1.038 | -21.78 |
| AP | CFFF | 0.095 | 0.095 | 0.98 |

***Table 10. $N_y$ Buckling Factors for Quadrilateral Panels.***

| Laminate | BC | Buckling Factor | | % Error |
|---|---|---|---|---|
| | | Ritz | FEM | |
| VAT1 | SSSS | 1.516 | 1.419 | 6.85 |
| VAT1 | CCCC | 0.800 | 0.879 | -9.05 |
| VAT1 | CFFF | 0.213 | 0.195 | 9.23 |
| VAT2 | SSSS | 1.486 | 1.548 | -3.98 |
| VAT2 | CCCC | 1.826 | 3.105 | -41.18 |
| VAT2 | CFFF | 0.205 | 0.191 | 6.97 |
| VAT3 | SSSS | 1.577 | 1.263 | 24.79 |
| VAT3 | CCCC | 2.732 | 2.829 | -3.43 |
| VAT3 | CFFF | 0.441 | 0.427 | 3.19 |
| QI | SSSS | 1.588 | 1.511 | 5.11 |
| QI | CCCC | 2.260 | 2.762 | -18.16 |
| QI | CFFF | 0.584 | 0.730 | -19.96 |
| AP | SSSS | 1.836 | 1.637 | 12.11 |
| AP | CCCC | 2.635 | 3.293 | -19.98 |
| AP | CFFF | 0.331 | 0.310 | 6.90 |

Response of quadrilateral VAT laminates due to constant pressure was also investigated. Typical results are presented in **Figure 19** for the simply supported VAT[1] laminate. Deflection and strain profiles are shown in **Table 11** and **Table 12** and have good agreement with the FEM. The $\varepsilon_x$ fiber strain profile reflects the laminate stiffness distribution.

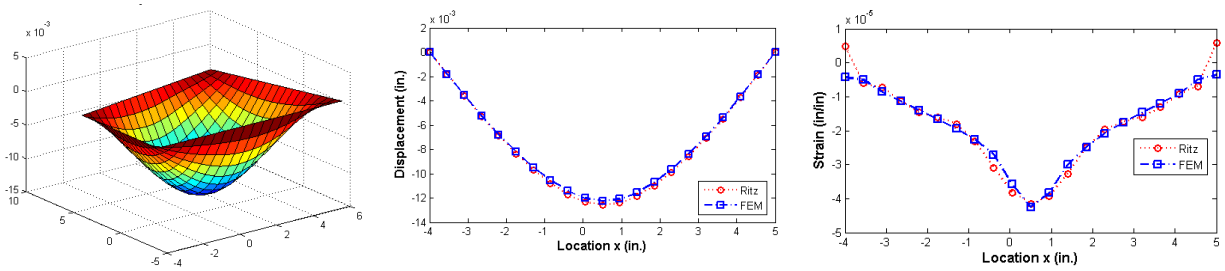


***Figure 19. Results Due to Pressure for Quadrilateral VAT Laminate: (a) Deflection, (b) Top $\varepsilon_x$ Strain, (c) Top $\varepsilon_{xy}$ Strain.***

***Table 11. Deflection of Quadrilateral VAT Laminates Due to Pressure***

| Laminate | BC | Max Deflection | | %Error |
|---|---|---|---|---|
| | | Ritz | FEM | |
| VAT1 | SSSS | -0.013 | -0.012 | 2.73 |
| VAT1 | CCCC | -0.004 | -0.004 | -3.68 |
| VAT1 | CFFF | -0.289 | -0.297 | -2.54 |
| VAT2 | SSSS | -0.010 | -0.010 | 1.60 |
| VAT2 | CCCC | -0.004 | -0.004 | -3.92 |
| VAT2 | CFFF | -0.316 | -0.340 | -7.22 |
| VAT3 | SSSS | -0.014 | -0.014 | -1.61 |
| VAT3 | CCCC | -0.004 | -0.003 | 4.12 |
| VAT3 | CFFF | -0.833 | -0.907 | -8.13 |

***Table 12. Max Fiber Strain of Quadrilateral VAT Laminates Due to Pressure.***

| Laminate | BC | Max Strain | | %Error |
|---|---|---|---|---|
| | | Ritz | FEM | |
| VAT1 | SSSS | -4.16E-05 | -4.26E-05 | -2.31 |
| VAT1 | CCCC | -1.99E-05 | -2.18E-05 | -8.71 |
| VAT1 | CFFF | 5.63E-04 | 4.79E-04 | 17.48 |
| VAT2 | SSSS | -2.51E-05 | -2.42E-05 | 4.02 |
| VAT2 | CCCC | -1.46E-05 | -1.47E-05 | -0.71 |
| VAT2 | CFFF | 5.70E-04 | 5.15E-04 | 10.87 |
| VAT3 | SSSS | -6.75E-05 | -6.50E-05 | 3.94 |
| VAT3 | CCCC | -2.01E-05 | -1.65E-05 | 22.01 |
| VAT3 | CFFF | 6.22E-04 | 5.75E-04 | 8.09 |

## E. Concluding Remarks

A high order Ritz solution procedure was developed to perform static, vibration and buckling analyses of variable stiffness laminates with generalized boundary conditions. In general, the Ritz solution demonstrated good agreement with Nastran FEM results for common panel geometries and VAT laminates. The significant errors associated with buckling factors for fully clamped boundaries indicates the possibility of a formulation error in the geometric stiffness matrix or inconsistent application of the boundary conditions for clamped Ritz and FEM cases. Future work should explore the use of this methodology with design optimization. More work is needed to analyze combined load conditions, perform fiber path optimization and implement thickness sizing with manufacturing constraints.

## References


[1]Bohlmann, J., and M. H. Love. "Aeroelastic Tailoring and Integrated Wing Design".1989.

[2]Blom, A. W., Lopes, C. S., Kromwijk, P. J., Gurdal, Z. and Camanho, P. P.. A theoretical model to study the influence of tow-drop areas on the stiffness and strength of variable-stiffness laminates. J. Composite Mater. 43(5), pp. 403-425. 2009.

[3]Hyer, M., and R. Charette. "The use of Curvilinear Fiber Format in Composite Structure Design." American Institute of Aeronautics and Astronautics, 1989. Structures, Structural Dynamics, and Materials and Co-Located Conferences.

[4]Hyer, M. W., and H. H. Lee. "The use of Curvilinear Fiber Format to Improve Buckling Resistance of Composite Plates with Central Circular Holes." Composite Structures 18.3 (1991): 239-61.

[5]Gurdal, Z., and Olmedo, R., "In-Plane Response of Laminates with Spatially Varying Fiber Orientations - Variable Stiffness Concept." AIAA Journal 31.4 (1993).

[6]Tatting, B. F., and Z. Gurdal. Design and Manufacture of Elastically Tailored Tow Placed Plates. NASA/CR—2002–211919 Vol. , 2002.

[7]Gurdal, Z., Tatting, B., and Wu, K. "Tow-Placement Technology and Fabrication Issues for Laminated Composite Structures." In: Proceedings of the 46th AIAA/ASME/ASCE/AHS/ASC Strcutures, Structural Dynbamics and Material (SDM) Conference, Austin, TX, April 18-21, 2005, Paper Number AIAA 2005-2017.

[8]Gürdal, Z., Tatting, B. F., and Wu., C. K., Variable stiffness composite panels: Effects of stiffness variation on the in-plane and buckling response. Composites Part A: Applied Science and Manufacturing 39(5), pp. 911-922. 2008.

[9]Nagendra, S., et al. "Optimization of Tow Fiber Paths for Composite Design." American Institute of Aeronautics and Astronautics, 1995. Structures, Structural Dynamics, and Materials and Co-Located Conferences Web.

[10]Tosh, Matthew William. "An Experimental and Numerical Investigation of Fibre Steering in Composite Structures." ProQuest, UMI Dissertations Publishing, 2000.

[11]Parnas, Levend, Oral and Ceyhan. "Optimum Design of Composite Structures with Curved Fiber Courses." Composites Science and Technology 63.7 (2003): 1071-82.

[12]Schueler, K., J. R. Miller, and R. Hale. "Approximate Geometric Methods in Application to the Modeling of Fiber Placed Composite Structures." Journal of Computing and Information Science in Engineering 4 (2004): 251-6. Print.

[13]Blom, Adriana W., et al. "Design of Variable-Stiffness Conical Shells for Maximum Fundamental Eigenfrequency." Computers and Structures 86.9 (2008): 870-8.

[14]Blom, Adriana W., et al. "Fiber Path Definitions for Elastically Tailored Conical Shells." Composites Part B 40.1 (2009): 77-84.

[15]Wu, Z., Weaver, P. M., Raju, G. and Kim, B. C. Buckling analysis and optimisation of variable angle tow composite plates. Thin-Walled Structures 60pp. 163. 2012.

[16]Alhajahmad, Ahmad, Mostafa M. Abdalla, and Zafer Gurdal. "Optimal Design of Tow-Placed Fuselage Panels for Maximum Strength with Buckling Considerations." Journal of Aircraft 47.3 (2010): 775-82.

[17]Honda, Shinya, Yoshihiro Narita, and Katsuhiko Sasaki. "Discrete Optimization for Vibration Design of Composite Plates by using Lamination Parameters." Advanced Composite Materials 18.4 (2009): 297-.

[18]H. Akhavan and P. Ribeiro. Natural modes of vibration of variable stiffness composite laminates with curvilinear fibers. Composite Structures 93(11), pp. 3040. 2011.

[19]Houmat, A., Nonlinear free vibration of laminated composite rectangular plates with curvilinear fibers. Composite Structures 106pp. 211-224. 2013.

[20]Houmat, A., Nonlinear free vibration analysis of variable stiffness symmetric skew laminates. *European Journal of Mechanics - A/Solids 50*pp. 70-75. 2015.

[21]Haddadpour, H., and Zamani, Z. Curvilinear fiber optimization tools for aeroelastic design of composite wings. J. Fluids Struct. 33pp. 180. 2012.

[22]Stodieck, O., Cooper, J. E., Weaver. J. E. and Kealy, P. Improved aeroelastic tailoring using tow-steered composites. Composite Structures 106pp. 703. 2013.

[23]Lukaszewicz, D. H., Ward, C. Potter, K.D. "The Engineering Aspects of Automated Prepreg Layup: History, Present and Future." Composites Part B: Engineering 43.3 (2012): 997-1009. Web.

[24]Tenney, D. R., et al. "NASA Composite Materials Development: Lessons Learned and Future Challenges". NATO Research and Technology Agency AVT 164 - Support of composite systems. 2009.

[25]MATLAB 2014.0, The MathWorks, Inc., Natick, Massachusetts, United States